Measurement of the Deeply Virtual Compton Scattering Cross Section from the Proton at 10.6 GeV using the CLAS12 Detector

by

Sangbaek Lee

B.S., Seoul National University (2016)

Submitted to the Department of Physics
in partial fulfillment of the requirements for the degree of

Doctor of Philosophy in Physics

at the

MASSACHUSETTS INSTITUTE OF TECHNOLOGY

September 2022

Author .....
Department of Physics
August 22, 2022

Certified by .....
Richard G. Milner
Professor of Physics
Thesis Supervisor

Accepted by .....
Deepto Chakrabarty
Associate Department Head of Physics

Measurement of the Deeply Virtual Compton Scattering Cross Section from the Proton at 10.6 GeV using the CLAS12 Detector

by

Sangbaek Lee

Submitted to the Department of Physics
on August 22, 2022,
in partial fulfillment of the requirements
for the degree of Doctor of Philosophy in Physics

Abstract

Deeply Virtual Compton Scattering (DVCS) is an exclusive process that produces a real photon when a lepton scatters from a quark inside a nucleon or a nucleus. Measurement of the DVCS cross section enables the study of the Generalized Parton Distributions (GPD), which plays a central role in understanding the QCD dynamics inside a hadron. Thus, the quark and gluon origin of the nucleon spin and mass can be probed and three-dimensional images of the target nucleon or nucleus can be realized. This thesis presents a cross section analysis of DVCS from the proton in the presence of its background, Bethe-Heitler (BH) process.

The CEBAF Large Acceptance Spectrometer for operation at 12 GeV beam energy (CLAS12) collaboration has taken electron-proton scattering data in fall 2018 using a liquid hydrogen target and the 10.6 GeV polarized electron beam from the Continuous Electron Beam Accelerator Facility (CEBAF). The CLAS12 detector is a nearly hermetic fixed-target detector, located in Hall B, Jefferson Lab at Newport News, Virginia.

The experimentally determined BH-DVCS cross section is in good agreement with a phenomenological-model based theoretical prediction. The kinematic dependence of the cross section is reported over a wide range. The short-term plan to utilize the results presented here for a thorough tomography study and the long-term plan for GPD studies at future facilities such as the Electron-Ion Collider (EIC) are discussed.

Thesis Supervisor: Richard G. Milner
Title: Professor of Physics

Acknowledgments

I would like to thank my Ph.D. advisor Prof. Richard G. Milner, first and foremost, for his guidance and support. It has been my pleasure to learn from his expertise as a great physicist and leader. I am grateful to my other committee members Prof. Iain W. Stewart and Prof. Robert L. Jaffe. I would like to acknowledge ILJU Foundation, JLab/JSA Graduate Fellowship and APS DNP Travel Fund for providing support for my Ph.D. study and dissemination.

This project would have never been possible without the collaborative effort. I am extremely thankful to Bobby Johnston for his outstanding works on the CLAS12 cluster computing and his dissertation analysis, DVπ^0P cross section measurement. I would like to thank MIT CMS members Benedikt Maier, Max Goncharov and Christoph Paus for their assistance with HTCondor and Axel Schmidt for his advice on SLURM computing. I am grateful to University of Connecticut group members Andrey Kim, Brandon Clary, David Riser, Paul Stoler, and Kyungseon Joo for illustrating CLAS12 data and code structure. Thanks should also go to Igor Korover for discussing how to efficiently analyze the data, design the database schema, and perform the smearing processes and normalization. I would like to acknowledge the entire CLAS Collaboration and the Jefferson Lab members including Latifa Elouadrhiri, Volker Burkert, Francois-Xavier Girod, Harut Avakian, Valery Kubarovsky, Maurizio Ungaro, Nathan Baltzell, Maxime Defurne, Daria Sokhan, Hyon-Suk Jo, Guillaume Christiaens, Josh Tan, Stefan Diehl, Raffaella de Vita, Dan Carman, Cole Smith, Stepan Stepanyan, Eugene Pasyuk, Mac Mestayer, Veronique Ziegler, Derek Glazier, Gagik Gavalian, Silvia Niccolai, Marco Contalbrigo, Marco Battaglieri, Nick Markov, Christopher Dilks, Timothy Hayward and Florian Hauenstein. I would like to mention Kyle Shiells, Yuxun Guo, Brandon Kriesten and Xiangdong Ji for the phenomenology discussion. I would like to recognize Igor Akushevich and Alexander Ilyichev for providing their codes for radiative correction and John Arrington for the electromagnetic form factor.

I would like to thank everyone who has supported me. I am deeply indebted to the

present and past group members Richard Milner, Doug Hasell, Igor Korover, Xiaqing Li, Patrick Moran, Bobby Johnston, Ross Corliss, Jan Bernauer, Ivica Friščić, Steve Steadman, Charles Epstein and Yimin Wang. I am also grateful to MIT physics department, LNS and ISO staff members Cathy Modica, Sydney Miller, Rosaleah Brown, Karma Yangzom, Lauren Saragosa, Karen Dow, Jack McGlashing, Elsye Luc, Alisa Cabral, Anna Maria Convertino and Janka Moss for taking care of a plethora of administrative matters. I was lucky to share my snug office, the penthouse with Yunjie Yang, Constantin Weisser, Tom Boettcher and Nick Buzinsky. I also want to extend my thanks to physics graduate students Field Rogers, Joe Johnston, Efrain Segarra, Alex Diaz, Lauren Yates, Yi Jia, Zhaozhong Shi, Afroditi Papadopoulou, Cedric Wilson, Ali Fahimniya and Çağın Yunus for taking this journey together. Special thanks to Dongha Kim, Choongman Lee, Min Gu Kang, Jong Yeon Lee, Sung Woo Jeong, Haeyeon Lee, Soomi Kim, Minjae Park, Hyungseok Song, Hyunseok Lee, Jaehwan Kim, Do Hun Kim, Youngkyu Sung, Seunghyeon Kim, Seong Ho Yeon, Jungki Song, Jae Hyung Cho, Yoonho Kim, Dongchan Lee, Sunjin Moon, Seungchan Ryu, Ho San Ko, Deok Yong Kim and many others for keeping me positive even during the pandemic. Last but not least, I want to thank my family—my cousins Sandra, André, Petra, Oliver, Ella, Johann, my uncle Ji-sang, my brother Sangwon and my parents Youngmi Kim and Nak Dong Lee. Words cannot express my gratitude to my parents, who have always been with me with their unconditional love.

Contents

List of Figures

List of Tables

Chapter 1

Introduction

This work focuses on the cross section measurements of electron-proton Deeply Virtual Compton Scattering (DVCS) with a liquid hydrogen target and the CLAS12 detector. A proton is the lightest stable QCD bound state consisting of quarks and gluons. The three-dimensional imaging of the proton via the Generalized Parton Distribution (GPD) formalism has been proposed to understand the spatial distributions of the proton's constituents. The DVCS is the cleanest such process that has access to the Generalized Parton Distributions. In this chapter, we discuss the theoretical background and history regarding the measurement.

1.1 Overview of Proton Structure

The proton is a physical object consisting of quarks and gluons and as the lightest baryon, is the only free, stable hadron whose decay has never been observed. The current knowledge describes the proton as a composite particle, with some macroscopic properties such as the mass m_p 938.272081± 0.000006 MeV/c^2, the charge radius $r_{ch,p}$=0.8409±0.0004 fm, spin s=1/2, and the magnetic moment $\mu_p = 2.7928473446\pm$ 0.00000000082 μ_N, where μ_N is the nucleon magneton [1]. Inside the hydrogen atom, the proton size is only $\sim 10^{-5}$ of the entire atom size ∼1 Å [2]. This is because the atom is an electromagnetic bound state and the proton is a strong interaction bound state.

The most successful theoretical framework to explain the strong interaction is generally within Quantum Field Theory (QFT), and more specifically Quantum Chromodynamics (QCD) [3]. Mathematically, the QFT lagrangian density is constructed from the fermionic field and the gauge bosonic field. The strong interaction is well modeled by the quarks that are the fermionic fields with spin-1/2, and the spin-1 gluons that are the $SU(3)$ gauge bosons. The $SU(3)$ color charge on the quarks and gluons within the Yang-Mills theory [4] is the basis for QCD. Together with other discovered gauge bosons for the electroweak interaction [5–7] and the Higgs mechanism [8], the Standard Model (SM) explains all experimental results in the laboratory in nuclear and particle physics. Investigating the dynamics inside bound objects like the proton is one of the major ways to understand QCD.

In studying subatomic structure, experimental observation plays an essential role. The historical events that brought breakthroughs include the atomic nucleus discovery [9, 10], the proton discovery [11], the neutron discovery [12], the confirmation that the proton itself is not a point-like particle [13], the theoretical development of quark model [14, 15] and color charge [16, 17] based on hadron spectroscopy, the scaling behavior [18] through the SLAC-MIT experiment, the detection of gluons at PETRA [19], and confirmation of the asymptotic freedom [20, 21] at HERA [22, 23]. We will revisit the details of some of these important experiments in the remainder of this chapter.

Scattering experiments have been a widely used tool to probe the structure of subatomic targets [24]. Generally, quantum mechanics or the QFT predicts the dependence of the target structure on the scattering amplitude. Therefore, it is possible to reconstruct the structure from the scattering amplitude, or from the experimentally accessible physical quantities, cross sections and decay rates. Historically, the application of scattering experiments to the sub-atomic structure study originated with the Geiger-Marsden experiment that discovered the existence of the atomic nucleus inside the gold atom [9, 10].

The electromagnetic structure of the proton as a whole can be studied via the electron-proton elastic scattering cross section [13]. The differential cross section $\frac{d\sigma}{d\Omega}$

when the fixed-target proton is replaced with a spin 1/2, point-like particle is given as

$$\frac{d\sigma}{d\Omega} = (\frac{d\sigma}{d\Omega})_{Mott.} \frac{E_{e'}}{E_{beam}} (1 + 2\tau \tan^2 \frac{\theta}{2}) \tag{1.1}$$

$$(\frac{d\sigma}{d\Omega})_{Mott.} = \frac{\alpha^2}{4E_{beam}^2 \sin^4(\theta/2)} \cos^2 \frac{\theta}{2} \tag{1.2}$$

$$\frac{E_{e'}}{E_{beam}} = \frac{1}{1 + E_{beam}/m_p(1 - \cos\theta)} \tag{1.3}$$

in the presence of the proton recoil. Here, the Mott cross section $(\frac{d\sigma}{d\Omega})_{Mott.}$ is the special case when the recoil can be neglected, and expressed with the fine-structure constant $\alpha \sim \frac{1}{137}$ [2], the electron beam energy E_{beam}, the scattered electron energy $E_{e'}$ and polar angle in lab frame θ. The space-like momentum transfer $Q^2 = -q^2$ where q is the virtual photon four-vector $p_{e'} - p_{beam}$, with p_{beam}, $p_{e'}$, the 4-momentum of the beam electron and the scattered electron e'. The parameter $\tau \equiv \frac{Q^2}{4m_p^2}$ quantifies the modification from the recoil.

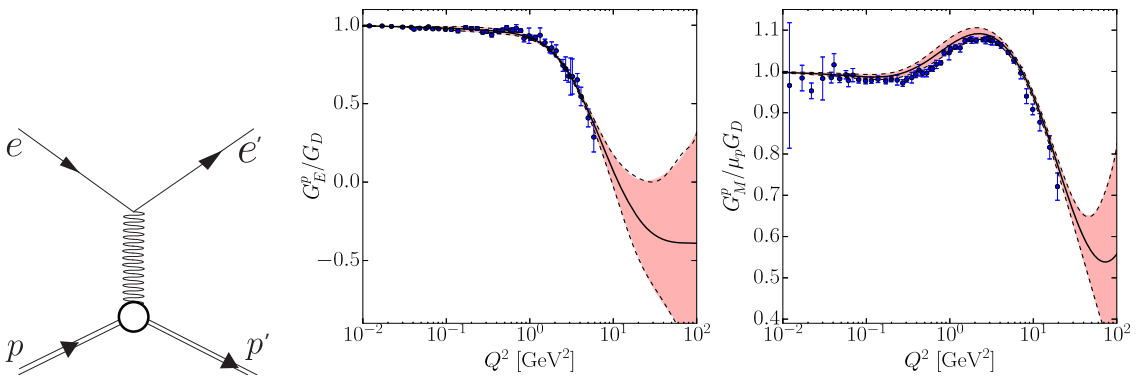

Figure 1-1: The tree-level Feynman diagram for elastic scattering (left) and the elastic FFs extracted from the cross-section measurements (middle, right). The FF plots with global fits were taken from [25], which used the data of previous experiments.

Because the proton is a composite particle of finite size, the momentum and spatial distributions of the constituent particles must modify the cross-section. Quantum Electrodynamics (QED) dominates the interaction between the electron and the proton and forces the interaction vertex to have the following form with the Pauli Form

Factor (FF) F_1 and the Dirac FF F_2 [3].

$$\Gamma^{\mu} = F_1\gamma^{\mu} + \frac{i}{2m_p}F_2 q_{\nu}\sigma^{\mu\nu} \tag{1.4}$$

$$\sigma^{\mu\nu} = \frac{i}{2}[\gamma^{\mu}, \gamma^{\nu}], \tag{1.5}$$

where $[a, b] = ab - ba$ is the commutator.

The experimentally preferred form of the FFs are the so-called *Sachs* FF, the electric FF G_E and the magnetic FF G_M [26] defined as

$$G_E(Q^2) = F_1(Q^2) - \tau F_2(Q^2) \tag{1.6}$$

$$G_M(Q^2) = F_1(Q^2) + F_2(Q^2). \tag{1.7}$$

The differential cross section $\frac{d\sigma}{d\Omega}$ is then given as

$$\frac{d\sigma}{d\Omega} = (\frac{d\sigma}{d\Omega})_{Mott.}\frac{E_{e'}}{E_{beam}}\left[\frac{G_E + \tau G_M}{1+\tau} + 2\tau G_M^2 \tan^2(\theta/2)\right]. \tag{1.8}$$

Eqn. 1.8 is known as the *Rosenbluth* formula [27]. The Rosenbluth separation is a well established technique to determine the elastic FFs by fitting the Rosenbluth formula to eqn. 1.1 at different Q^2 and θ. Note that one can achieve 1.1 by replacing G_E and G_M with 1 at eqn. 1.8. The electromagnetic FFs extracted using cross section measurements are in good agreement with the dipole FF $G_D(Q^2)$ at low Q^2 [28].

$$G_E(Q^2) \sim \frac{G_M(Q^2)}{\mu_p} \sim G_D(Q^2) = (1 + \frac{Q^2}{0.71\ (\mathrm{GeV/c})^2})^{-2}. \tag{1.9}$$

At sufficiently high $Q^2 > 1$ $(\mathrm{GeV/c})^2$, not only the measured G_E and G_M deviate signifcantly from G_D (Fig. 1-1), but also more importantly, the measured G_E/G_M ratio values from the traditional Rosenbluth separation show a large discrepancy with the data from the relatively recent polarization measurements [29]. The discrepancy has stimulated great interested in the contribution of Two-Photon Exchange (TPE) [30–32] that could explain the discrepancy. The Bethe-Heitler (BH) cross sections in this thesis were calculated with the global fit of G_E and G_M from the supplementary

material of [25] that considered the TPE corrections. The momentum transfer in elastic scattering Q^2 is equivalent to the absolute value of the Mandelstam variable $|t|$ at the virtual Compton scattering. The kinematic reach of t is limited to $|t| < 1.7$ GeV^2 in this thesis, which does not result in a significant uncertatinty by using $G_E,\ G_M$ for this analysis.

The proton as a bound state of point-like particles can be studied via inelastic scattering. The modification of the cross section is parameterized by the structure function F_1 and F_2 [33, 34]. Bjorken scaling predicts F_1 and F_2 are function of only $x_B \equiv \frac{Q^2}{2p_{p'}\cdot q}$[1], the momentum fraction of the struck quark in the Breit frame. Likewise on the lepton side of the Feynman diagram, the four momenta p_p and $p_{p'}$ denote the initial and final state proton four momenta. With Lorentz invariant parameter $\nu = \frac{p_{p'}\cdot q}{m_p}$, the differential cross section $\frac{d\sigma}{d\Omega dE_{e'}}$ is given as

$$\frac{d\sigma}{d\Omega dE_{e'}} = \frac{4\alpha^2 E_{e'}^2}{Q^4}\cos^2\frac{\theta}{2}\left[\frac{F_2}{\nu}\cos^2\frac{\theta}{2} + \frac{2F_1}{m_p}\sin^2\frac{\theta}{2}\right] \tag{1.10}$$

at sufficiently large $Q^2 > 1$ (GeV/c)^2 and $W > 2$ GeV (DIS region), where the invariant mass $W \equiv (p_{p'} + q)^2$. Another important consideration for scaling is the Lorentz invariant variable $y \equiv \frac{p_{p'}\cdot q}{p_{p'}\cdot p_p}$, known as the *inelasticity*. For fixed-target experiments, it is useful to express the variables with experimentally accessible quantities as follows:

$$x_B = \frac{Q^2}{2m_p\nu} \tag{1.11}$$

$$Q^2 = 4E_{beam}E_{e'}\sin^2(\theta/2) \tag{1.12}$$

$$\nu = E_{beam} - E_{e'} \tag{1.13}$$

$$y = \frac{\nu}{E_{beam}} \tag{1.14}$$

$$p_p = (M, 0, 0, 0) \tag{1.15}$$

$$p_{beam} = (E_{beam}, 0, 0, E_{beam}). \tag{1.16}$$

The mass of the electron was neglected in eqns. 1.12 and 1.16. From the observed

[1]The DIS convention is to denote the Bjorken x as x, but we will reserve x for another usage in the DVCS.

behavior that F_2 shows a flat distribution in Q^2, it was confirmed that the Bjorken scaling $F_2(x_B)$ is effective [18, 35], and further that the proton consists of point-like particles [36]; this motivated the parton model [37]. The suppression of the longitudinal contribution to the DIS cross section σ_L implies the validity of the Callan-Gross relation $F_2(x_B) = 2x_B F_1(x_B)$ in the DIS regime [38]. This further supports the interpretation that the partons have spin 1/2 as the quark model states [14, 15]. The DIS data taken at HERA [22, 23] show the rise of F_2 at low x_B with increasing Q^2, consistent with asymptotic freedom, namely that the QCD coupling constant α_S becomes sufficiently small at high energy scales [20, 21]. This motivates the scale factorization of the hard contribution that can be calculated by using perturbative QCD (pQCD), and the soft part that can be determined by experiment. Employing the factorization theorem [39], one can evolve the structure function with the QCD evolution equation (DGLAP [40–42]) to other Q^2 regions.

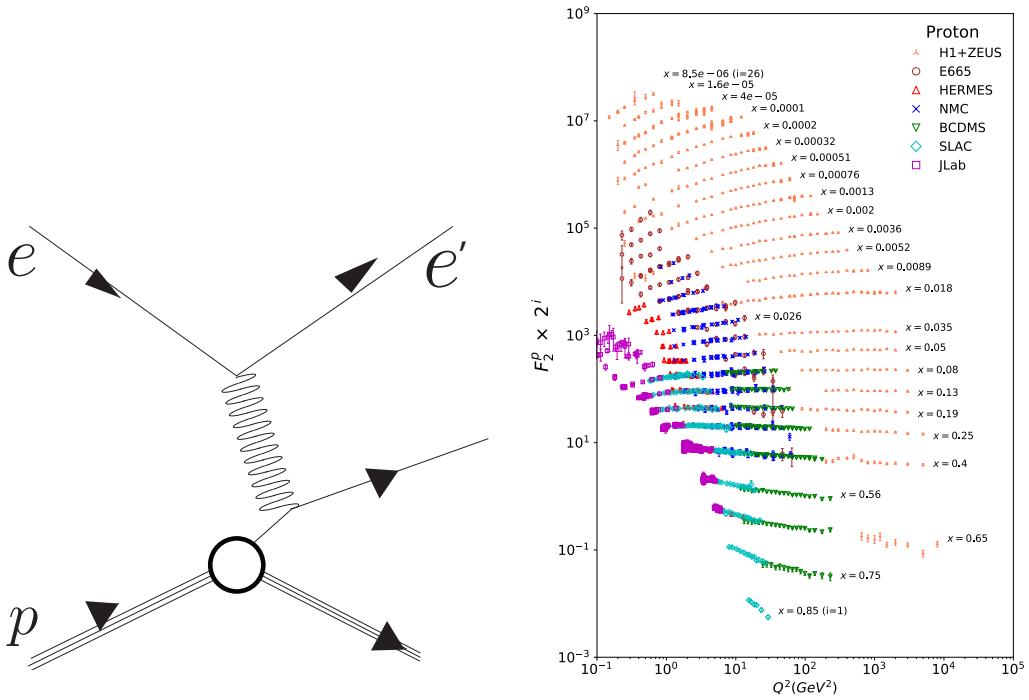

Figure 1-2: The tree-level, schematic Feynman diagram of DIS (left) and the structure function F_2 extracted from previous experiments (middle, right). The F_2 plot was taken from [1], which used the data of the previous experiments.

The parton model connects the structure function F_2 to the Parton Distribution

Function (PDF) $q_i(x_B)$, the probability density to find the parton in the interval (x_B, $x_B + dx_B$)

$$F_2(x_B) = x_B \sum_i e_i^2 q_i(x_B), \tag{1.17}$$

where e_i is the electric charge of each quarks i ($e_i = 2/3$ for *up* quarks, and -1/3 for *down* quarks). From the definition of x_B, the PDF can be interpreted as the distribution of proton longitudinal momentum. Therefore, the integral and moments in x_B of the PDFs describe the contribution to the proton structure from each quark flavor. In particular, the spin quantum number constrains the spin contribution from the substructure,

$$\frac{1}{2} = \frac{1}{2}\sum_i \Delta q_i + \Delta g + L_q + L_g, \tag{1.18}$$

where $\frac{1}{2}\sum_i \Delta q_i = \frac{1}{2}(q_i^{\uparrow} - q_i^{\downarrow})$ is the quark spin contribution, Δg is the gluon contribution, and L_q, L_g are the quark and gluon Orbital Angular Momentum (OAM) contributions, respectively. The spin-dependent structure function [43] defined as $g_1(x_B) = \frac{1}{2}e_i^2 \Delta q_i(x_B)$ for the spin dependent DIS experiments is the spin-dependent equivalent of the unpolarized momentum PDFs and plays an essential role in the spin sum rules such as the Bjorken sum rule [44, 45] and the Ellis-Jaffe sum rule [46]. The Bjorken sum rule relates the proton and neutron spin structure functions via isospin invariance as follows:

$$\Gamma_1^p - \Gamma_2^n = \int_0^1 dx\ [g_1^p(x_B) - g_2^n(x_B)] = \frac{1}{6}\frac{g_A}{g_V} \tag{1.19}$$

with the transverse spin-dependent structure function g_2 [47], and the vector and axial weak coupling constants g_V and g_A. With the Conserved Vector Current (CVC) and Partially Conserved Axial Current (PCAC) hypothesis, we follow the convention $g_V = 1$, and take the measured g_A from neutron beta decay [1]. The Ellis-Jaffe sum rule was derived with tighter assumptions of light flavor symmetry ($SU(3)_f$), and an

unpolarized strange sea for the separate nucleons,

$$\Gamma_1^{p,\ n} = \pm\frac{1}{12}(F+D) + \frac{5}{36}(3F-D), \tag{1.20}$$

where D and F are $SU(3)_f$ couplings. The EMC experiment [48] reported that the Ellis-Jaffe sum rule was violated. This implies that the proton spin cannot be reproduced only by the quarks inside the proton, which was termed the so-called *proton spin crisis* [49, 50].

The spin content of the nucleon can be decomposed in the following way [33, 51, 52].

$$\frac{1}{2} = \Delta L_q + \frac{1}{2}\Sigma + \Delta L_g + \Gamma\ , \tag{1.21}$$

where Σ and Γ are the contributions of the quarks and gluons, and L_q and L_g are the Orbital Angular Momentum (OAM) contributions of the quarks and gluons. The measurements from various experimental programs have consistently found that $\Sigma \sim 0.3$ [53, 54]. The STAR [55, 56] and PHENIX [57, 58] data imply that the gluon contribution Γ is significant [59].

1.2 Generalized Parton Distribution and Deeply Virtual Compton Scattering

The concept of Generalized Parton Distributions (GPD) [60] was developed using a mathematical approach to determine correlated information on momentum and spatial phase space [61–63] in the 1990s.

The optical theorem [3] identifies the imaginary part of the forward scattering with a sum of all possible intermediate state contributions, i.e., branch cut diagrams [64]. The specific example can be found in the DIS-Forward Compton Scattering case (Fig. 1-3). The cross section for DIS is connected to the imaginary part of the forward limit amplitude of the DIS. The reaction associated with the forward limit is called

the double DVCS process, where two photons are all virtual.

It is conventional to use the light-cone coordinate system to formally treat the QCD scale factorization [65] regarding the FF, PDF, and GPD. Before we discuss the mathematical details, we borrow the diagrammatic representation of [66] (Fig. 1-4). The matrix elements related to proton-photon (or virtual photon) interactions are related to each other. The four-momenta x and y are defined in the light-cone coordinate system, and one can choose replace $0, y \rightarrow -z/2, z/2$ without loss of generality [67]. Now, the PDFs are formally expressed using Fourier transformations as follows:

$$q(x) = \frac{p_p^+}{2} \int \frac{dz^-}{2\pi} e^{ixp_p^+ z^-} < p_p|\bar{\psi}_q(-\frac{1}{2}z)\gamma^+\psi_q(\frac{1}{2}z)|p_p > |_{z^+=0,\mathbf{z}=0} \tag{1.22}$$

$$\Delta q(x) = \frac{p_p^+}{2} \int \frac{dz^-}{2\pi} e^{ixp_p^+ z^-} < p_p|\bar{\psi}_q(-\frac{1}{2}z)\gamma^+\gamma^5\psi_q(\frac{1}{2}z)|p_p > |_{z^+=0,\mathbf{z}=0} \ . \tag{1.23}$$

To reduce the ambiguity, we fix the choice of the light-cone basis, $n^\pm = (n^0 \pm n^3)/\sqrt{2}$. In general there is also a Wilson line (path ordered exponential of gauge fields), which runs between the two fermion fields. It is suppressed here.

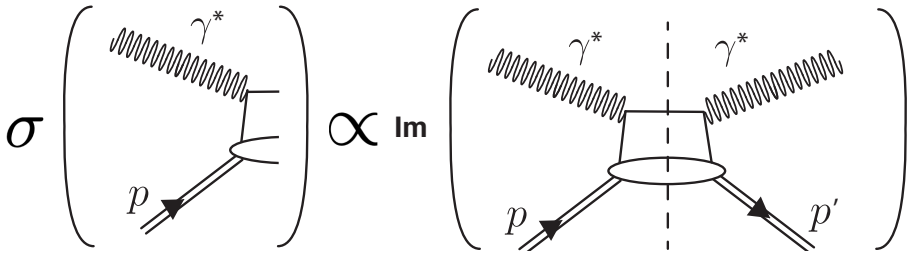

Figure 1-3: The representation of the optical theorem of the DIS and the Forward Compton Scattering in Feynman diagrams. The DIS cross section (left) is connected to the imaginary part of the forward Compton scattering, which is the forward limit amplitude.

The matrix element for the Fermi and Dirac FF can be formally expressed as well in momentum space. The Fourier transform is not required here because the

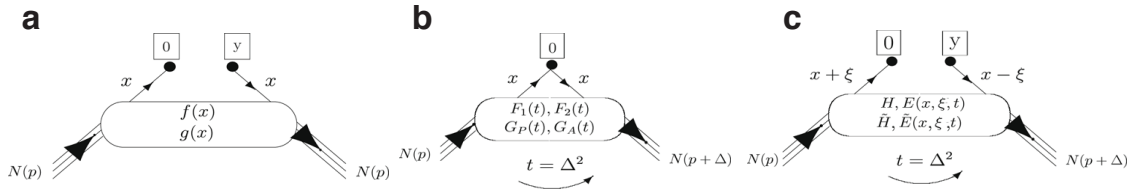

Figure 1-4: Illustration of the matrix elements (a) non-local forward (b) local nonforward, and (c) nonlocal nonforward cases. The (a), (b), and (c) are related to the DIS, Elastic Scattering, and the DVCS respectively. The original image was from [66].

operators are local.

$$< p_p|\bar{\psi}_q(0)\gamma^+\psi_q(0)|p_p >= F_1^q(|t|)\bar{N}(p_{p'})\gamma^+N(p_p) + F_2^q(|t|)\bar{N}(p_{p'})i\sigma^{+\nu}\frac{\Delta_\nu}{2m_N}N(p_p) \tag{1.24}$$

$$< p_p|\bar{\psi}_q(0)\gamma^+\gamma^5\psi_q(0)|p_p >= G_A^q(|t|)\bar{N}(p_{p'})\gamma^+\gamma^5N(p_p) + G_P^q(|t|)\bar{N}(p_{p'})\gamma^5\frac{\Delta_+}{2m_N}N(p_p). \tag{1.25}$$

The relations hold for both nucleons whose wave function is N and the mass is m_N. The superscript q of the FF are the light quark flavor (u, d, s) to denote each quark's contribution. As mentioned in Section 1.1, now t replaces Q^2. The new terms, G_A and G_P, are the axial and the induced pseudoscalar form factors, respectively.

Finally, the non-local, off-forward matrix element were defined as follows [61–63].

$$\begin{aligned} P_p^+\int\frac{dz^-}{2\pi}e^{ixP_p^+z^-} < p_{p'}|\bar{\psi}_q(-\frac{1}{2}z)\gamma^+\psi_q(\frac{1}{2}z)|p_p > |_{z^+=0,\mathbf{z}=0} = \\ H^q(x,\xi,|t|)\bar{N}(p_{p'})\gamma^+N(p_p) + E^q(x,\xi,|t|)\bar{N}(p_{p'})i\sigma^{+\nu}\frac{\Delta_\nu}{2m_N}N(p_p) \end{aligned} \tag{1.26}$$

$$\begin{aligned} P_p^+\int\frac{dz^-}{2\pi}e^{ixP_p^+z^-} < p_{p'}|\bar{\psi}_q(-\frac{1}{2}z)\gamma^+\gamma^5\psi_q(\frac{1}{2}z)|p_p > |_{z^+=0,\mathbf{z}=0} = \\ \tilde{H}^q(x,\xi,|t|)\bar{N}(p_{p'})\gamma^+\gamma^5N(p_p) + \tilde{E}^q(x,\xi,|t|)\bar{N}(p_{p'})\gamma^5\frac{\Delta_+}{2m_N}N(p_p), \end{aligned} \tag{1.27}$$

where $P_p = p_p + p_{p'}$, $\Delta = p_{p'} - p_p$ and $H, E, \tilde{H}, \tilde{E}$ are the generalized parton distributions. Again, there is a Wilson line between the quark fields, which is not shown. The generalized Bjorken variable ξ is a Lorentz invariant term defined as $\xi \equiv -\frac{q^2}{q\cdot P} \sim \frac{x_B}{2-x_B}$, where $P \equiv p_p + p_{p'}$. Another variable x originates as a dummy variable to simplify

the light-cone correlation functions [62]. The physical interpretation is that $x+\xi$ and $x-\xi$ are the longitudinal parton momentum fractions with respect to P [68] and integrated over in the scattering amplitude (Fig. 1-6). The GPDs H and E are the quark helicity averaged and thus unpolarized GPDs. The other two terms $\tilde{H}$ and $\tilde{E}$ are quark helicity dependent and called polarized GPDs. At the nucleon level however, E and $\tilde{E}$ are associated with the nucleon spin flip, and H and $\tilde{H}$ are the nucleon spin conserving terms [69].

One can interpret the GPD as the generalization of FFs and PDFs (eqn. 1.28–1.33). The effective operators determining the GPD are non-forward and non-local whereas those determining the FF are non-forward but local and determining the PDFs are non-local but forward [69]. The concept of a GPD is connected to the transverse spatial distributions in the impact parameter space [70] as well (eqn. 1.34). In short, the GPD is central to one main branch of tomography from the full phase space density distributions (Fig. 1-5). Related to the quark spin contributions, the GPD is expected to play a role in reconciling the theoretical and experimental quark contributions in the proton spin crisis. The equations that represent the characteristics of the GPDs are as follows:

$$\int_{-1}^{-1} dx H(x,\ \xi,\ |t|) = F_1(|t|) \tag{1.28}$$

$$\int_{-1}^{-1} dx E(x,\ \xi,\ |t|) = F_2(|t|) \tag{1.29}$$

$$\int_{-1}^{-1} dx \tilde{H}(x,\ \xi,\ |t|) = G_A(|t|) \tag{1.30}$$

$$\int_{-1}^{-1} dx \tilde{E}(x,\ \xi,\ |t|) = G_P(|t|) \tag{1.31}$$

$$H_q(x,\ 0,\ 0) = q(x) \tag{1.32}$$

$$\tilde{H}_q(x,\ 0,\ 0) = \Delta q(x) \tag{1.33}$$

$$q(x, \mathbf{b}_\perp) = \int \frac{d^2\mathbf{\Delta}}{(2\pi)^2} H_q(x, -\Delta_\perp^2) e^{-i\mathbf{b}_\perp \cdot \mathbf{\Delta}_\perp} \tag{1.34}$$

$$J_q = \frac{1}{2} \int_{-1}^{+1} dx\ x[H^q(x,\ \xi,\ |t|=0) + E^q(x,\ \xi,\ |t|=0)]. \tag{1.35}$$

The eqn. 1.35 is often referred to as the Ji sum rule. The GPDs can be probed by QCD processes like DVCS [62, 71]. The principle of a QCD scattering experiment is that the scale factorization allows separation of the information on the structure function. The cross section is considered to be factorizable when it can be expressed as a product of hard, collinear, and soft contributions [65]. There is the special kinematics region that the factorization is valid. In the Bjorken limit, namely $Q^2 \gg m_p^2$ and $|t| \ll Q^2$, the factorization for the DVCS was proved rigorously [63, 71–74]. The experimental results discussed in Section 1.3 has been supporting the idea that the factorization can be applied for the Q^2 around a few $(\mathrm{GeV/c})^2$ level.

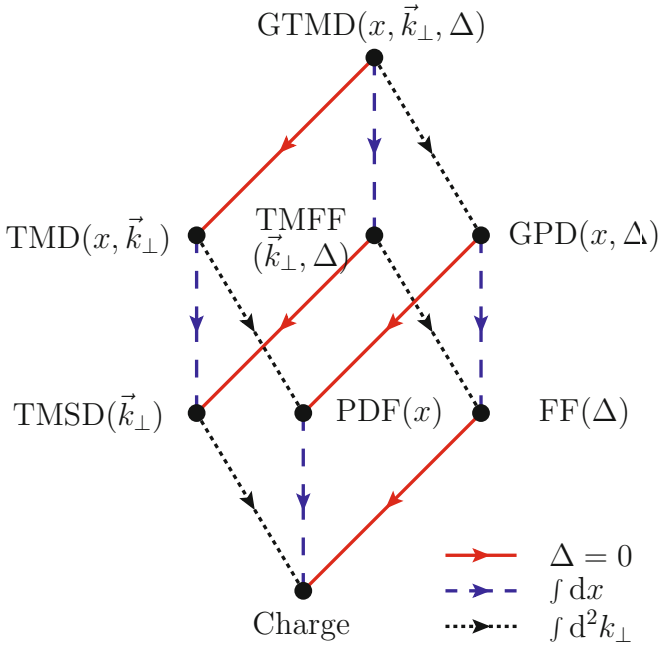

Figure 1-5: The entire tomography program that includes the GPD, FF, and PDFs. The figure was imported from the original publication [75].

DVCS is deeply inelastic electroproduction of a real photon in the lepton scattering process from the struck quark inside the hadron. In this thesis, we use the electron as the lepton and the proton as the hadron. The DVCS as a reaction of $ep \to e'p'\gamma$ shares identical initial and final states with the BH process (Fig. 1-7). Therefore, the total scattering amplitude is the coherent summation of BH and DVCS [76, 77]. The

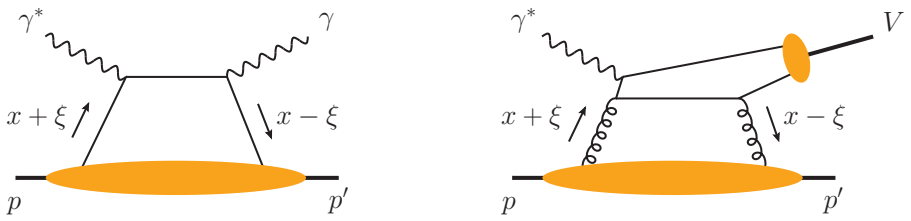

Figure 1-6: The graphical descriptions for physical meaning of x and ξ for the DVCS (left) and the DVMP (right). This figure was imported from the original publication [68]

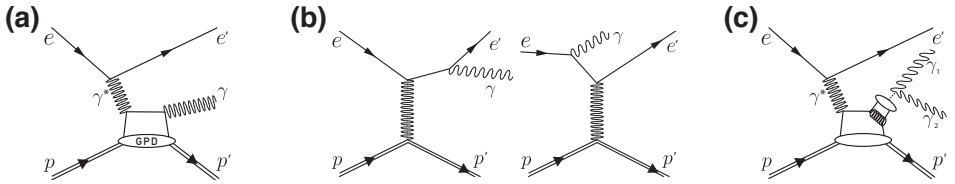

Figure 1-7: The Feynman diagrams of the (a) DVCS process, (b) BH processes and (c) DVπ^0P process.

differential cross section is expressed as follows[2].

$$\frac{d^5\sigma}{dx_B dQ^2 d|t| d\phi d\varphi} = \Gamma \times |\mathcal{T}_{\rm BH} + \mathcal{T}_{\rm DVCS}|^2 = \Gamma \times (|\mathcal{T}_{\rm DVCS}|^2 + |\mathcal{T}_{\rm BH}|^2 + \mathcal{I}) \tag{1.36}$$

$$\Gamma = \frac{\alpha^3}{16\pi^2 (s-M^2)^2 x_B \sqrt{1+\epsilon^2}} \tag{1.37}$$

$$s - M^2 = \frac{Q^2}{x_B y} \sim 2ME_{beam}, \tag{1.38}$$

where Γ is the virtual photon flux, $\epsilon \equiv 2x_B \frac{m_p}{Q}$. The variable ϕ is the angle between the lepton scattering plane and the hadronic scattering plane in the Trento convention (Fig. 1-8). The last variable φ is related to the target polarization, and integrated out to 2π for this experiment. The scattering amplitudes of BH $\mathcal{T}_{\rm BH}$ and DVCS $\mathcal{T}_{\rm DVCS}$ are propotional to FF and Compton Form Factors (CFF) respectively. The interference term $\mathcal{I}$ is trivially defined as $\mathcal{T}^*_{\rm BH}\mathcal{T}_{\rm DVCS} + (h.c.)$. Each contribution can be expressed

[2]One can perform the change of variables to achieve the $dx_B dQ^2$-based differential cross section from $d\Omega dE_{e'}$ using the relations eqns. 1.11–1.13. For details, see the problem 8.3 of [34], for example.

as a Fourier series in ϕ,

$$|\mathcal{T}_{\rm BH}|^2 = \frac{1}{x_B^2 y^2 (1+\epsilon^2)^2 t \mathcal{P}_1(\phi)\mathcal{P}_2(\phi)} \sum_{n=0}^{2} (c_n^{\rm BH}\cos(n\phi) + s_n^{\rm BH}\sin(n\phi)) \tag{1.39}$$

$$|\mathcal{T}_{\rm DVCS}|^2 = \frac{1}{y^2 Q^2} \sum_{n=0}^{2} (c_n^{\rm DVCS}\cos(n\phi) + s_n^{\rm DVCS}\sin(n\phi)) \tag{1.40}$$

$$\mathcal{I} = \frac{1}{x_B y^3 t \mathcal{P}_1(\phi)\mathcal{P}_2(\phi)} \sum_{n=0}^{3} (c_n^{\mathcal{I}}\cos(n\phi) + s_n^{\mathcal{I}}\sin(n\phi)), \tag{1.41}$$

where $s_0 = 0$ and the expansion order limits are determined by the approximate twist level, equivalent to the spin dimension of the operator [78]. The BMK approximation takes the twist-3 approximation [76].

The lepton propagators $\mathcal{P}_1$ and $\mathcal{P}_2$ have the following dependence on the particle kinematics,

$$\mathcal{P}_1(\phi) = (p_{beam} - p_\gamma)^2 \tag{1.42}$$

$$\mathcal{P}_2(\phi) = (p_{beam} - \Delta)^2, \tag{1.43}$$

where p_γ is the 4-momentum of the outgoing photon γ.

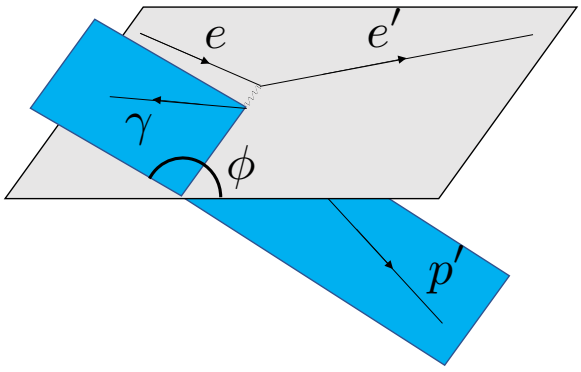

Figure 1-8: A schematic drawing of the particle kinematics of DVCS and BH scattering in the lab frame. The planes in grey and blue colors are the lepton scattering plane and the hadronic scattering plane, respectively.

The CFF is defined as the convolutional integral of the GPD terms. Convention-

ally, the CFF terms are divided into the real and imaginary parts [69]:

$$H_{Re}(\xi,t) \equiv \mathcal{P}\int_0^1 dx[H(x,\xi,t) - H(-x,\xi,t)]C^+(x,\xi) \tag{1.44}$$

$$\tilde{H}_{Re}(\xi,t) \equiv \mathcal{P}\int_0^1 dx[H(x,\xi,t) + H(-x,\xi,t)]C^-(x,\xi) \tag{1.45}$$

$$H_{Im}(\xi,t) \equiv H(\xi,\xi,t) - H(-\xi,\xi,t) \tag{1.46}$$

$$\tilde{H}_{Im}(\xi,t) \equiv H(\xi,\xi,t) + H(-\xi,\xi,t) \tag{1.47}$$

$$C^{\pm} = \frac{1}{x-\xi} \pm \frac{1}{x+\xi}. \tag{1.48}$$

The eqns. 1.44–1.47 hold for E terms as well. These GPD terms $H, E, \tilde{H}, \tilde{E}$ are twist-two quark GPDs that are governing the DVCS observables. One can further study the subleading order contributions of the transversity GPDs [79], gluon transversity GPDs, and twist-three GPDs [76]. The transversity was defined within the context of the transverse spin structure functions [47, 80, 81]. The quark transversity GPDs are more senstive to the Deeply Virtual Meson Production (DVMP) observables, and beyond the scope of this thesis. The contributions of twist-three and gluon transversity GPDs are discussed in many references [76, 77, 82].

A global fit to determine CFFs was an immediate research priority after the GPD was invented. The CFF models should satisfy the polynomial relation for GPDs:

$$\int_{-1}^1 dx x^n H(x,\xi,t) = a_0 + a_2\xi^2 + ... + a_{2\lceil n/2\rceil}\xi^{2\lceil n/2\rceil}, \tag{1.49}$$

where $2\lceil n/2\rceil$ is a mapping to n for even n and $n+1$ for odd n.

An early GPD parametrization was based on the Double Distribution (DD) ansatz [83, 84]; here the GPD is parametrized by decorrelating Δ and p_p. For given t,

$$\mathrm{GPD}^q(x,\xi) = \int_{-1}^1 d\beta \int_{-1+|\beta|}^{1-|\beta|} d\alpha \delta(x-\beta-\xi\alpha)h(\beta,\alpha)q(\beta) \tag{1.50}$$

$$h(\beta,\alpha) = \frac{\Gamma(2b+2)}{2^{2b+1}\Gamma^2(2b+1)} \frac{[(1-|\beta|)^2-\alpha^2]^b}{(1-|\beta|)^{2b+1}}, \tag{1.51}$$

with a free parameter b, and the Γ in eqn. 1.51 is the Euler gamma function defined as

$\Gamma(z) = \int_0^{\int} t^{z-1}e^{-t}dt$. Although the DD elegantly satisfies the polynomiality condition (eqn. 1.49), this idea neglected the last order $a_{n+1}\xi^{n+1}$ when n is odd. The problem was resolved by introducing the D-term $D(x/\xi, t)$ [85] as follows.

$$D(x/\xi, t) = (1 - (x/\xi)^2) \sum_{k=0}^{\infty} d_{2k+1}(t) C_{2k+1}^{3/2}(x/\xi), \tag{1.52}$$

where $C_{2k+1}^{3/2}$ is the Gegenbauer polynomial. Extracting the D-term components in GPDs, and connecting to the pressure and shear distributions inside the proton is a state-of-the-art research topic [86–88]. The models based on the DD ansatz include the VGG model [89] and the GK model [90]. Another representation is to decompose the GPDs in a partial-wave expansion [91]. The dual parametrization method was the earliest partial-wave expansion approach. It has been called "dual" in that the GPDs were representated as the infinite series of t-channel exchanges [92]. Later, the partial-wave idea was further generalized with the Mellin-Barnes integral representation [93, 94]. The details of the three types of GPD paramterization can be found in the review papers [69, 95, 96]. These three models are mathematically related and the dual parametrization method is equivalent to the Mellin-Barnes integral representation [97].

A phenomenological problem has been known that the DD ansatz is not ideal for fitting data sets with different ξ [96, 98]. The Mellin-Barnes representation provides the useful global GPD fitting procedure [95]. The KM15 model arises from the global fitting of the data sets from the ZEUS [99, 100], H1 [101, 102], HERMES [103–105], CLAS [106–109], and Hall A [110, 111] experiments and demonstrates that the CFF model is quite consistent with the world data. It is released publicly [112].

1.3 Status of Experiments

The common approaches in the experimental study of the DVCS process can be roughly categorized into four areas. I. The BH coefficients of polarized target experiments and the DVCS and Interference term coefficients (eqns. 1.39–1.41) have

the lepton helicity and the nucleon spin dependences [76]. II. The polarized beam of the same lepton and the polarized target have access to the differences of cross sections that each helicity state generates. The former is often called the Beam Spin Asymmetry (BSA), and the latter is called the Target Spin Asymmetry (TSA). III. Measurement of absolute cross section measurement allows for direct comparison with the theoretical predictions. IV. Lastly, performing the experiment with the same environment, but with the corresponding antiparticle lepton beam, changes the sign of eqn. 1.41, which is called the Beam Charge Asymmetry (BCA). For example, the experiments at HERA performed measurements of the BSA with lepton beams of both signs.

Here we summarize the major experiments have been performed in the facilities for lepton-hadron scattering and collision since the GPD was established in the 1990s. The facilities include the HERA collider and the HERMES fixed-target experiment at DESY, the COMPASS experiment at CERN, and the halls A and B at CEBAF, Jefferson Lab. At HERA, experiments used the polarized electron and positron beams and released several results including the BCA at H1 [101], t-dependence of the cross section at H1 [113] and Q^2, W, and t-dependence at ZEUS [99]. The HERMES experiment released the BSA [114], BCA [115], and TSA with target polarized longitudinally [104] and transversely [105]. The COMPASS experiment used the polarized muon beam to acesss the t-dependence [116]. The Jefferson Lab measurements include the TSA [117], BSA [108], and cross section [107] measurements from CLAS and the cross section from Hall A [110, 111]. The earlier Hall A result [110] supported the scale separation for the GPDs at intermediate Q^2 by performing the scaling test in a model independent way. The Hall A collaboration recently published measurements of the neutron DVCS cross section [118]. Reference [119] sorted the performed experiment and accessible GPD variables from the measured observables.

The proposed experiments at Jefferson Lab include the positron beam experiments to measure the BCA at CLAS [120] and Hall C [121, 122], and the polarized target experiments to measure the TSA at CLAS [123–125].

Each method has different sensitivity to the GPD terms. The sensitivities are sub-

ject to the experiment's resolution and acceptances. We leave the reader to consider several efforts to sort the sensitivity to each of the DVCS observables [119, 126–128]. As discussed in Section 1.2, the polarized target is useful to investigate the nucleon spin flip or the quark helicity dependent terms. The conventional notation to denote the relevant asymmetry is A; A_C for the beam-charge asymmetry, A_{XY}, where X and Y are beam helicity and target spin. These are written as U, L, and T to represent unpolarized, longitudinal, and transverse respectively. The collected data are about A_C, A_{UL}, A_{UT}, A_{LL}, A_{LT}, and A_{LU}. The COMPASS measured the charge-spin sum asymmetry with the unpolarized target $A_{CS,U}$ and the transversely polarized target $A_{CS,T}$. There are two ways of defining cross sections with the polarized beam: the unpolarized cross section $d\sigma_{unp.}$ and the polarized cross section $d\sigma_{pol.}$.

$$d\sigma_{unp.} = \frac{1}{2}(d\sigma^{\rightarrow} + d\sigma^{\leftarrow}) \tag{1.53}$$

$$d\sigma_{pol.} = \frac{1}{2}(d\sigma^{\rightarrow} - d\sigma^{\leftarrow}) \tag{1.54}$$

This thesis aims at the determination of the precise BH-DVCS differential cross section as a primary goal, focusing on $d\sigma_{unp.}$. The interference term gives access to the linear combinations of twist two GPD terms $\tilde{H}, H, E$: $F_1 H + \xi(F_1 + F_2)\tilde{H} + \frac{|t|}{4m_p^2} F_2 E$ and $-\xi(F_1 + F_2)\left\{\xi(H + E) + \tilde{H}\right\}$. The Fourier coefficients for the cosine terms take the real parts and the sine terms take the imaginary parts of the CFFs at the interference term [76]. The pure DVCS term is proportional to the bilinear form of CFFs and is expected to be relatively flat over ϕ. At the fixed-target kinematics, the scales of two terms are both generally sizeable (Fig. 1-9 from [77]). The differences in their phase dependence allow the generalized Rosenbluth separation, which will be discussed in Chapter 5.

We will then discuss connecting to the global fitting in Chapter 5. The latest release of the cross section measurement at Hall A spectrometer [129] implies that the experimental data agree reasonably well with the KM15 model [95]. Extracting the twist-three contribution from the experimental data is an important task for the nucleon structure study [77, 130], but this thesis concentrates on the twist-two

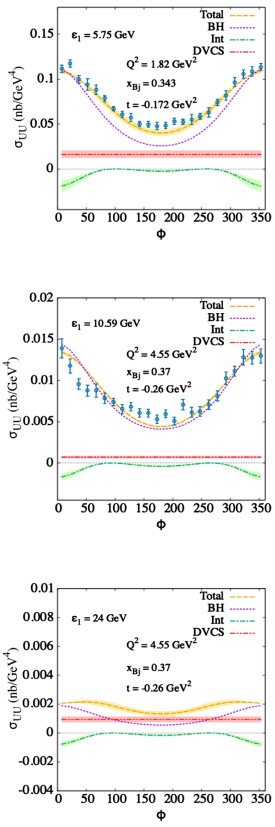

Figure 1-9: The theoretical predictions on the interference and pure DVCS contributions to the unpolarized cross sections at Jefferson Lab experiments. The original image was from [77]. The top and middle plots were drawn with the Hall A data with beam energies of 5.75 GeV [111] and 11.5 GeV [129] respectively. The bottom plot is the projected results at E_{beam}=24 GeV. The figure of merit at y axes σ_{UU} are the total cross section $d\sigma_{unp.}$.

contribution [131].

In the few decades since the GPD was first proposed, measurement of the GPDs has become a principal approach to proton tomography. At the moment when this thesis is being written, the future facility where the DVCS and GPD research takes place most comprehensively is undisputedly the Electron-Ion Collider (EIC) [68, 132]. The kinematic coverage of this work and the past CLAS measurement [107] is overlayed on that of EIC and other past experiments in Fig. 1-10. The plot demonstrates that this work will provide the CFF fitting in large acceptance with the multidimensional binning, and a prediction to be tested at the EIC by future experiments.

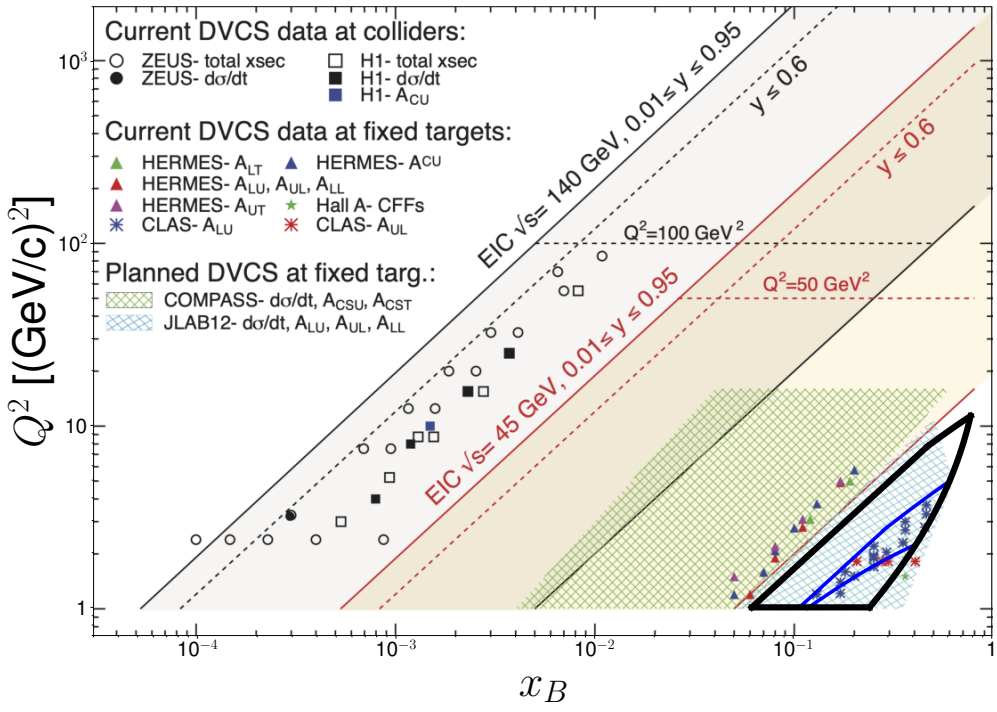

Figure 1-10: The kinematic reach in the Q^2-x_B plane of various experiments performed until 2012. The original image was from [68]. The overlaid black and blue curves indicate the coverage of this work and the CLAS result [107].

Chapter 2

Experiment

In this chapter, we describe the details of the experimental apparatus. Understanding the performance of the experimental apparatus during data taking is an essential aspect of the analysis. As we stated in Chapter 1, the experiment was performed in the Run Group A (RG-A) period in fall 2018 at Hall B Jefferson Lab, with the liquid hydrogen target. The protons in the target interact with the continuous wave electron beam of energy 10.6 GeV and requested beam currents delivered from the CEBAF. The CEBAF Large Acceptance Spectrometer for operation at 12 GeV beam energy (CLAS12) detector inside the Hall-B of the accelerator hall is a hermetic system that effectively detects the particles in the final state from the deep exclusive processes. The triggered events are recorded and saved in specified data formats that are consecutively processed by the analysis chain.

2.1 CLAS12 DVCS Experiment

The CLAS12 DVCS Experiment in RG-A is an officially approved project (E12-06-119) by the Physics Review Committee (PAC) of the Jefferson Lab [133] that aims to measure the CFF with the extracted BSA and the cross section at RG-A beamtime. This work focuses on the cross section measurement only. In fall 2018, two sets of experiments have been performed with opposite toroidal magnetic field directions keeping the other detector settings the same. The toroidal magnet bends the scattered

trigger electron inward or outward along the beam direction. In convention, the torus polarity associated with the inwardly bending electrons is called the negative, -1, -100%, or inbending polarity. The opposite is called the positive, +1, +100%, or outbending polarity. Both experiments took data with the beam energy of 10.6 GeV, and the beam current of about 50 nA. The effects due to the variation in the beam current during the run periods will be taken into account at the end of the analysis.

The CLAS collaboration performed other CLAS12 experiments with different targets like liquid deuterium, and various beam energies. The description in this thesis will be focused on the RG-A fall 2018.

2.2 Accelerators

The Continuous Electron Beam Accelerator Facility (CEBAF), after its energy upgrade to 12 GeV, is able to deliver Continuous Wave (CW) electron beam that is bunched at 499 MHz to Hall-B. The electron beam is accelerated when it passes through the Linear Accelerator (LINAC) part of the CEBAF (Fig. 2-1. 5 pass beam was delivered to Hall-B with an energy of 10.6 GeV.

For any fixed-target experiment using coincidence particle detection, higher duty cycle of the beam reduces the false coincidence rate. Thanks to the CW electron beam from the CEBAF, the duty factor is almost 100% which allows measurement of the DVCS cross section that requires the coincidence detection of electron, proton, and photon.

The Radio Frequency (RF) signal with a period of 2.004 ns identifies the time of the scattered electron at the vertex. This time is generally called the vertex time, and the electron vertex time is defined as the start time of the event. The beam was delivered in every other RF bucket, and so bunched at a period of 4.008 ns.

Lastly, the electron beam was polarized, the polarization degree of which was determined by the Møller polarimeter upstream of the CLAS12 detector. The measured electron beam polarization was 86.9% during the RG-A data taking in fall 2018.

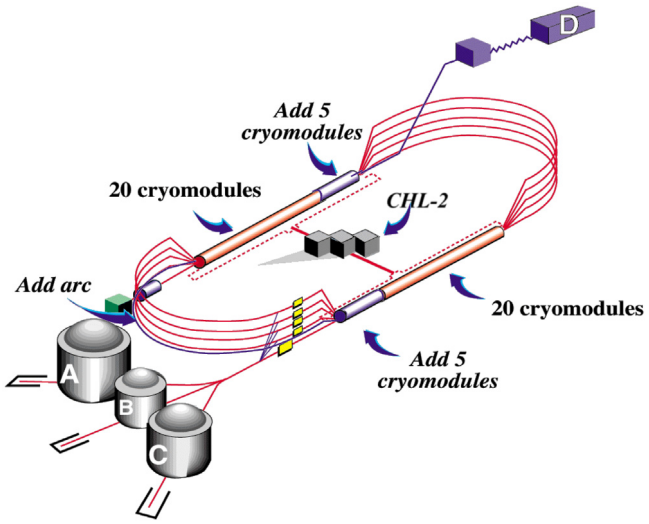

Figure 2-1: A schematic drawing of the CEBAF accelerator. The original image was imported from [134].

2.3 Detectors and Reconstruction Principle

The CLAS12 detector is designed for fixed-target experiments with the CEBAF electron beam in Hall-B [134]. The RG-A target system is constructed from a target cell containing liquid hydrogen and an associated cryogenic system. The pure LH_2 section is located from -5.5 cm to -0.5 cm in z axis of the CLAS12 coordinate system, where the beam is directed from -z to +z [135].

The CLAS12 detector consists of the Forward Detector (FD), the Central Detector (CD), and the Forward Tagger (FT). The FD consists of the High Threshold Cherenkov Counter (HTCC) [136], the Low Threshold Cherenkov Counter (LTCC) [137], the Ring Imaging Cherenkov detector (RICH) [138], the Forward Time-of-Flight (FTOF) [139], the Drift Chamber (DC) [140], and the Electromagnetic Calorimeter (ECAL) [141]. The ECAL has three layers of sampling calorimeters named as the Pre-shower Calorimeter (PCAL), the EC-inner, and the EC-outer. The EC-inner and EC-outer are two layers of the legacy Electromagnetic Calorimeter (EC) of the previous CLAS experiment [142]. Likewise, the FTOF has three layers—FTOF 1a, FTOF 1b, and FTOF 2. The LTCC and the RICH were not used in this measurement. By forward, it means that the FD covers from 5° to 35° polar angle, except for the

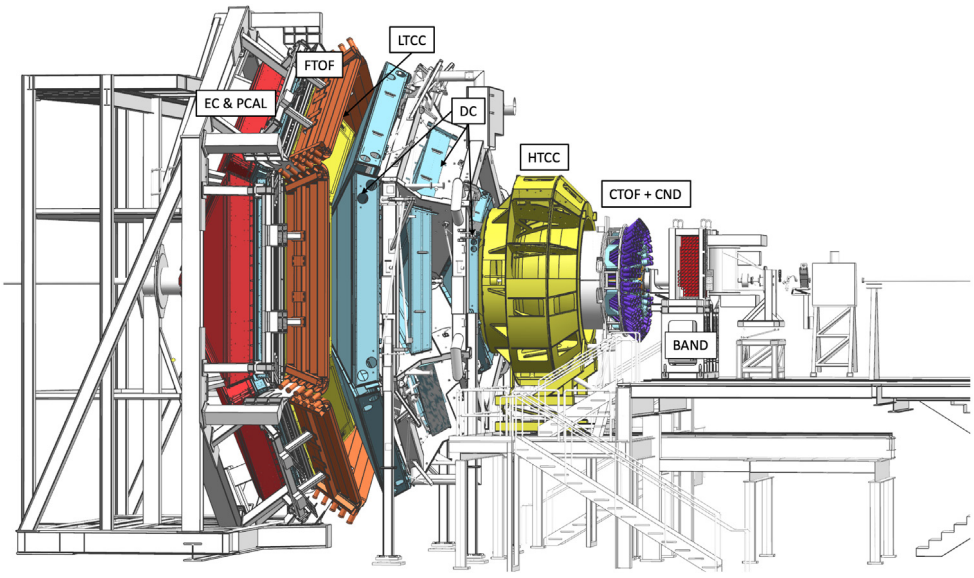

Figure 2-2: A schematic drawing of CLAS12 detector. The original image was imported from [134].

FTOF 2 that covers 35–45°. Each detector in FD is divided into 6 sectors in azimuth that each covers 60° with a counterclockwise numbering convention that the sector 1 corresponds to [-30°, 30°].

Outside the FD, a wider range of polar angles is covered by the CD. The CD has the Central Vertex Tracker to reconstruct hadrons. The CVT is formed by the Barrel Micromega Tracker (BMT) [143], and the Silicon Vertex Tracker (SVT) [144] during the runs. The main part is the SVT, while the BMT is used to improve the track reconstruction. The Central Neutron Detector (CND) [145] was installed but not used in this measurement. Meanwhile, the Backward Angle Neutron Detector (BAND) [146] and the Forward Micromegas Tracker (FMT) [143] were not installed. Inside the FD, there is the FT [147] that covers 2.5–4.5°, which is an independent set of three detectors: the tracker (FT-Trk), the homogeneous calorimeter (FT-Cal), and the hodoscope (FT-Hodo).

To determine the momentum of charged particles, each solenoid and torus magnet surrounds the FD and the CD [148]. The peak magnetic fields in the solonoid and the torus are 5 T and 3.58 T, respectively, with the line-integrated magnetic field ($\int Bdl$) 7.0 T·m and 0.54–2.78 T·m, where the limits correspond to 40° and 5° polar

angle coordinate, respectively. Both are super-conducting magnets that are cooled by means of cryostats.

The ECAL is roughly 9 m distant from the target in the beamline direction and is the farthest detector from the target. The Faraday Cup at the beam dump measures the beam charge to an uncertainty of 0.48% [135, 149]. The Data Acquisition (DAQ) [150] dead-time can be corrected by using a gate at the FC that closes when the DAQ procedure is complete [135]. The total charge regardless of the gate is called the ungated charge, and the charge collected during the gate on is the gated charge. The ratio of the gated charge to the ungated charge is recorded as the DAQ live-time. The complete listing of detector components can be found in Table. 2.1. The CLAS12 detector components relevant to the particle 4-momentum vector reconstruction are grouped by their characteristics in Table. 2.2. The essential properties like threshold and resolutions and the prominent material components are also listed.

An electron candidate e' is defined as an associated signal of these FD signals: (1) a track in DC, (2) photoelectrons in HTCC, (3) hits in FTOF, (4) energy deposited over 60 MeV, and (5) the Sampling Fraction (SF) of Minimum Ionizing Particle's (MIPs). Here, the event start time is determined from the track information, and corrected by the RF signal and the vertex location. The momentum of a charged particle such as e' and the proton p' is reconstructed using the equation of motion in a magnetic field. The polar angle difference during the trajectory $\Delta\theta$ is related to the momentum p and the charge q of the particle, and the line-integrated magnetic field along the trajectory curve, $\int Bdl$ as

$$\frac{q}{p} = \frac{\Delta\theta}{c \int Bdl}. \tag{2.1}$$

During one event, p' is identified when there is a positively charged track in the DC or the CVT, associated with FTOF or CTOF hits for the timing. The flight time $\Delta t_{p'}$ of p' is determined as the difference of TOF hits and event start time. Along with the path length $l_{p'}$ and the momentum $p_{p'}$ determined from the trajectory, the

Table 2.1: The layout of CLAS12 detector subsystems and their usage in this experiment.

	Name	Primary Usage (this work)
FD	HTCC	e' trigger, PID
	LTCC	not used
	RICH	not used
	FTOF	e' trigger, p' PID
	DC	e' trigger, e' and p' momentum determination
	ECAL	e' trigger, PID, γ energy determination
CD	CTOF	p' PID
	CVT	p' momentum determination
	CND	not used
	FMT	not installed
	BAND	not installed
FT	FT-Cal	γ energy determination
	FT-Hodo	γ PID
	FT-Trk	γ angle determination
Magnets	Solenoid	surrounds CD
	Torus	surrounds FD
Beamline	Target	5 cm long LH_2 target
	FC	luminosity determination

following relationship holds [151]:

$$\beta_{p'} \equiv \frac{v_{p'}}{c} = \frac{l_{p'}}{c\Delta t_{p'}} = \frac{p'}{p'^2 + M_p^2}. \tag{2.2}$$

We take the common relativity notation for $\beta = \frac{v}{c}$ where v is the velocity of the particle and c is the speed of light. Here, $\chi \equiv \Delta t/\sigma_{TOF}$ with $\Delta t \equiv \Delta t_{p',\text{expected}}(p') - \Delta t_{p',\text{measured}}$ is assigned to the particle as the signed distance function from the theoretical value. The photon γ can be reconstructed in the ECAL in FD, and the FT-Calorimeter in the FT. A photon will not produce charged tracks in the DC and the FT-Hodo associated with the existing calorimeter hits. More efficiently, the neutral hits are defined as the remaining calorimeter hits after all charged particles are assigned. The energy deposition in ECAL is converted to the actual photon energy using the SF. The homogeneous calorimeter FT-Cal takes the energy deposition as the photon energy.

Table 2.2: The properties of the relevant subdetectors for the DVCS analysis. The properties relate mostly to the effective measurement uncertainties listed in each NIM article [135, 136, 140, 141, 143, 144, 147, 152].

Name	Coverage (°)	Nominal Property	Material
HTCC	5–35	0.015< p <4.9 GeV/c	CO_2
FTOF 1B	5–35	60–110 ps (t)	plastic scintillator
FTOF 1A	5–35	90–180 ps (t)	
FTOF 2	35–45	170–180 ps (t)	
CTOF	35–125	80 ps (t)	
ECAL	5–35	$10\%/\sqrt{E}$ (E) 1.2 mrad (θ, ϕ)	Pb (absorber) plastic scintillator
FT-Cal	2.5–4.5	$2\%/\sqrt{E} \oplus 1\%$ (E) 1.5% (θ) 2° (ϕ)	$PbWO_4$ crystal
DC	5–40	1% (p) 1 mrad (θ) 1 mrad/$\sin\theta$ (ϕ)	aluminium wire 90% Ar 10% CO_2
CVT	35–125	5% (p_t) 10–20 mrad (θ) 5 mrad (ϕ)	SVT: Si BMT: 90%Ar+10%C_4H_10
FC	-	0.48% ($\mathcal{L}$)	Pb

2.4 Particle Identification

The individual Particle Identification (PID) is a requirement of the exclusive coincidence measurement and our event selection. In this section, the details of the PID with the related plots are presented. The first level PID is done with the Event Builder (EB) service with COATJAVA library [151] that is associated with the particle reconstruction principles described in Section 2.3. The detector volume was also considered in the EB service to exclude the fiducial region effectively. The cuts excluding the borders of the detector will be referred to as the fiducial cuts throughout the thesis.

The PID cuts were further enforced at the post-processing offline stage of analysis to ensure high reconstruction quality. Most of them were developed within the collaboration's common effort to analyze the RG-A data. The RG-A PID cuts were proven to be effective in various analysis channels [153–155]. Hence, we present the survival rates of two non RG-A fiducial cuts only: the proton fiducial cut at CD and

the photon fiducial cut at FT.

We present the plots of the PID variables in this section. The data sets used for plotting have already exclusivity cut applied. The passed cut is the 'DVCS Wagon' to select events with electron e', proton p', photon γ candidates with a loose DVCS exclusivity condition. The details of the DVCS wagon will be described in Section 2.5 and Chapter 3. This results in the PID cuts listed in this section to appear to be redundant. However, the PID techniques have been developed with the inclusive data sets and individual particles without the exclusivity condition. The well-defined PID cuts are the necessary conditions for defining exclusivity sets. The additional PID cuts defined after the exclusivity selection will be introduced in Section 5.2 with tables describing the effect of the PID cuts on the exclusive $e'p'\gamma$ and $e'p'\gamma\gamma$ data sets.

2.4.1 Electron Identification

The identification of an electron originates with fact that the electron is a negatively charged particle of mass of 510.9989461±0.0000031 keV/c^2 [1]. The unique characteristics of the high energy scattered electron defines the electron candidates as follows:

- The electron should follow a trajectory inside the drift chamber with a negatively charged particle's curvature. i.e., the electron should bend inwardly in the inbending data set and outwardly in the outbending data set.
- The electron mass is light enough to allow the electron to pass the timing detectors at the speed of light.
- The electron should leave the energy deposition of MIP at the calorimeter. This means (1) the PCAL energy deposition ($E_{dep.\ \mathrm{PCAL}}$) should be larger than some limits (60 MeV), and (2) the SF $\equiv \frac{p}{E_{dep.}}$ is roughly constant. The denominator of the SF is the total energy deposited in the ECAL system, i.e., $E_{dep.\ \mathrm{PCAL}} + E_{dep.\ \mathrm{EC\text{-}inner}} + E_{dep.\ \mathrm{EC\text{-}outer}}$, where the subscripts denote the corresponding ECAL layers.
- The electron should be differentiated from the π^-'s by the hard threshold of the number of photoelectrons ($n_{phe.}$) in HTCC at 2. This cut can effectively

perform e/π separation from e-threshold 15 MeV/c to π-threshold 4.9 GeV/c.

The conditions above are fulfilled by the EB service that is applied to the raw data [151]. For an effective discussion, we start from the EB selected electrons. For the tighter electron selection, a further requirement should be added at the post-processing stage.

- The electron SF is further limited to the narrower region. This cut is defined as 3.5σ curves of SF-$p_{e'}$ that were fitted separately for each sector, for the experimental data (Fig. 2-3) and for the simulation (Fig. 2-4).
- The calorimeter energy deposition threshold should be higher than the EB condition to reduce the π^- contamination. The cut was determined to be 70 MeV (Fig. 2-9).
- The electron hits must exclude the DC and ECAL detector fringes. The DC fiducial cuts are defined for all three layers of the DC separately for both polarities. The effect of the fiducial cut on the outmost layer is presented in Figs. 2-5–2-6. The PCAL fiducial cuts are defined as $l_V,\ l_W$ >9 cm (Fig. 2-8) where $l_{U,V,W}$ are the readout distances defined over the three alternating stereo readout planes U, V, W (Fig. 2-7).
- The reconstructed vertex location must be in the vicinity of the target location. The nominal z position of the scattered electron $vz_{e'}$ is located within the target that ranges from -5.5 cm to -0.5 cm in the CLAS12 coordinate system. Accordingly, the v_z cut is defined as (-13, 12) cm range for the inbending and (-18, 10) cm range for the outbending (Fig. 2-10).
- The anti-pion cut must be reinforced by the ECAL energy deposition for the electron with energy above 4.9 GeV. The effective cut is $E_{dep.\ \text{EC-inner}}/p_{e'} + E_{dep.\ \text{PCAL}}/p_{e'} > 0.2$ (Fig. 2-11), and applied for $p_{e'}$ >4.5 GeV.

The electron selection was further refined by removing some regions in (l_U, l_V, l_W) in PCAL that are not efficient in the experimental data set. This procedure is

related to the effort to match the experimental data to the simulation data, and will be introduced in Section 5.2.

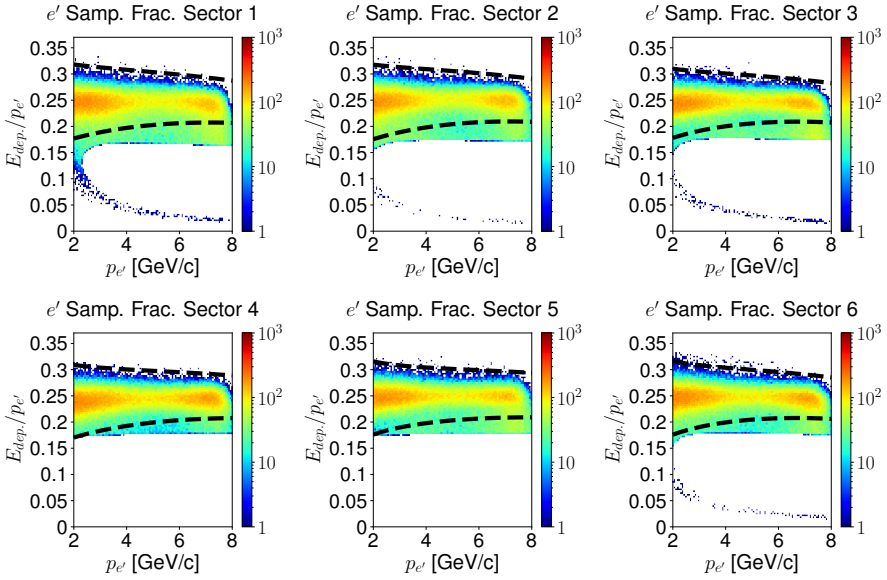

Figure 2-3: The 2D histograms of SF and $p_{e'}$ before the RG-A PID cuts. The black dotted curves indicate the 3.5σ ranges of 2D distributions for each sector defined with the electron candidates in the inclusive data set. Note that the cuts exclude the tails in the low SF region.

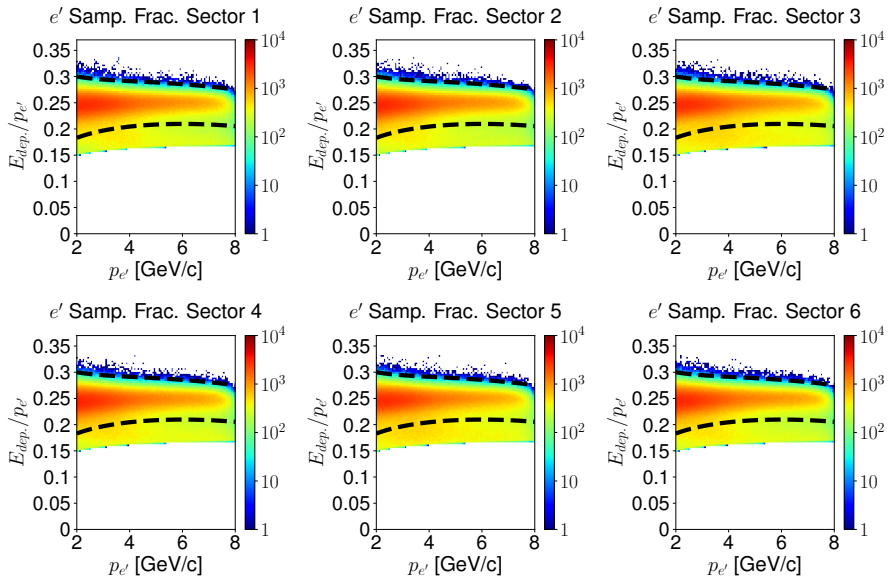

Figure 2-4: The 2D histograms of SF and $p_{e'}$ of the electron candidate before the RG-A PID cuts on the MC simulation data set. The black dotted curves indicate the 3.5σ ranges of 2D distributions for each sector defined with the electron candidates in the inclusive electron simulation. Note that there is no tail issue, unlike the experimental data (Fig. 2-3)

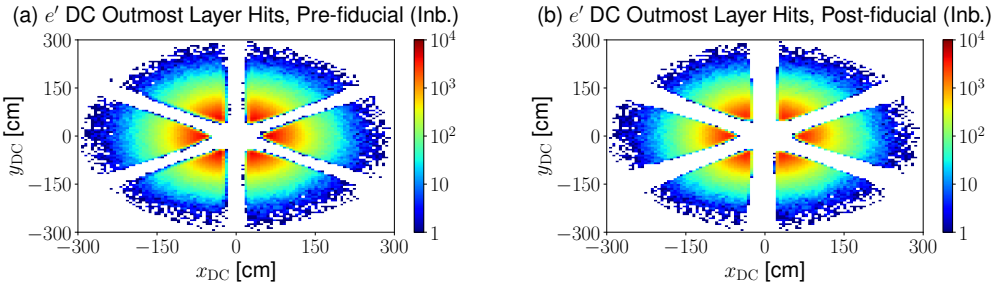

Figure 2-5: The 2D histograms of e' hit positions y_{DC} and x_{DC} of the electron candidate (a) before the RG-A PID cuts, and (b) after the cuts for the inbending data set.

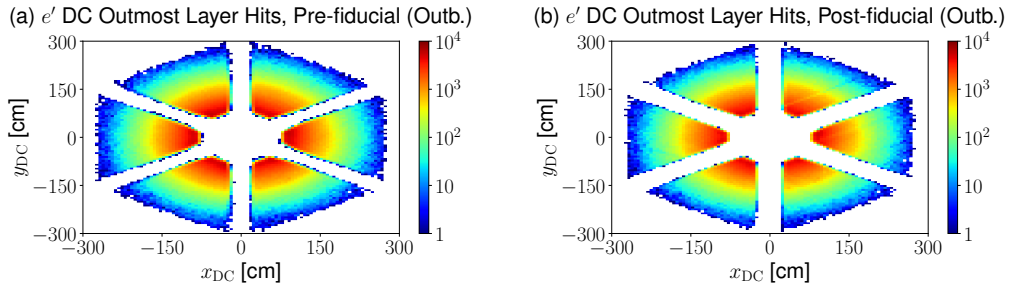

Figure 2-6: The 2D histograms of e' hit positions y_{DC} and x_{DC} of the electron candidate (a) before the RG-A PID cuts and (b) after the cuts for the outbending data set.

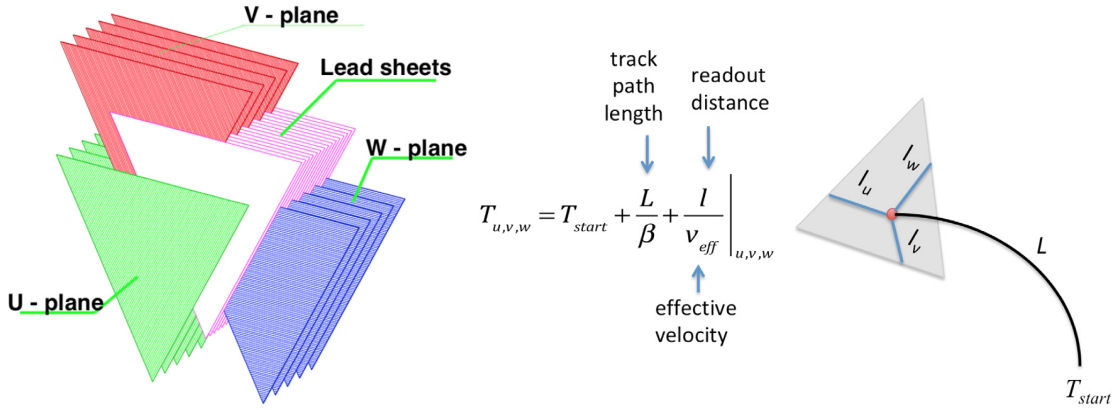

Figure 2-7: The definition of the readout planes U, V, W, and corresponding readout distances $l_{U,V,W}$. The original figures were imported from the ECAL NIM article [141].

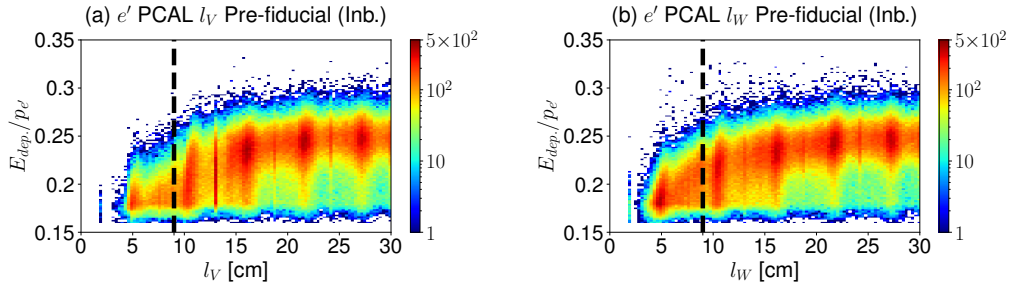

Figure 2-8: The 2d histograms of SF and (a) l_V, (b) l_W before the RG-A PID cuts. The black dotted lines indicates the fiducial cuts $l_V, l_W = 9$ cm.

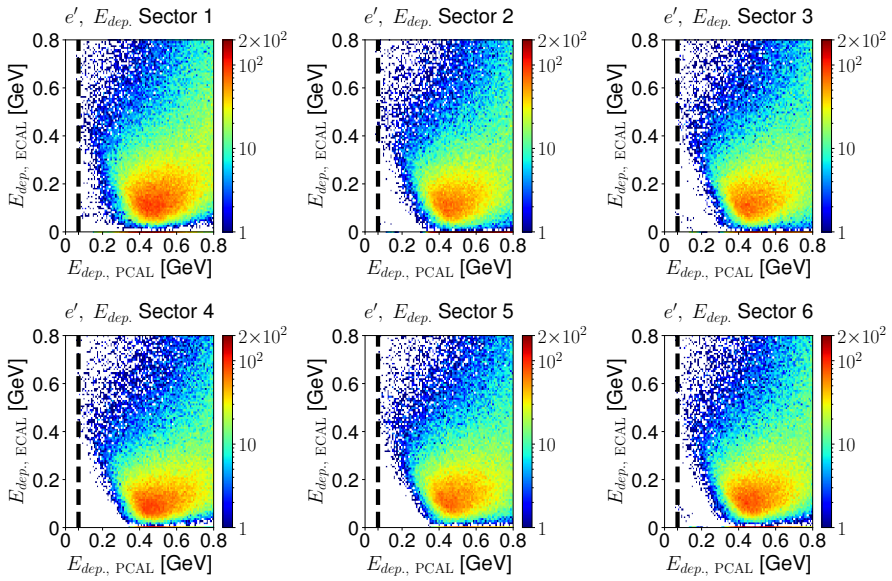

Figure 2-9: The 2d histograms of energy depositions $E_{dep.\ \mathrm{PCAL}}$ and $E_{dep.\ \mathrm{ECAL}} = E_{dep.\ \text{EC-inner}} + E_{dep.\ \text{EC-outer}}$ before the RG-A PID cuts. The black dotted lines indicate the 70 MeV threshold to exclude the π^-, which looks redundant after the exclusivity cuts.

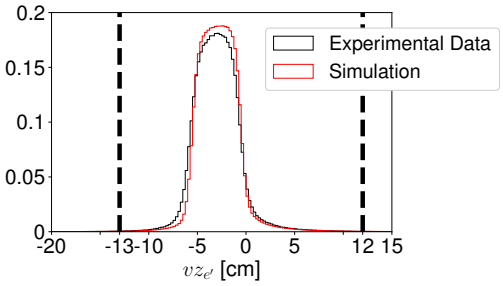

Figure 2-10: The histogram of vertex z position of the electron candidate, $vz_{e'}$ before the RG-A PID cuts for the inbending data set. The horizontal axis is the number of photoelectrons ($n_{phe.}$) with bin width 1. The vertical axis is the normalized density of the experimental data (black) and the simulation (red).

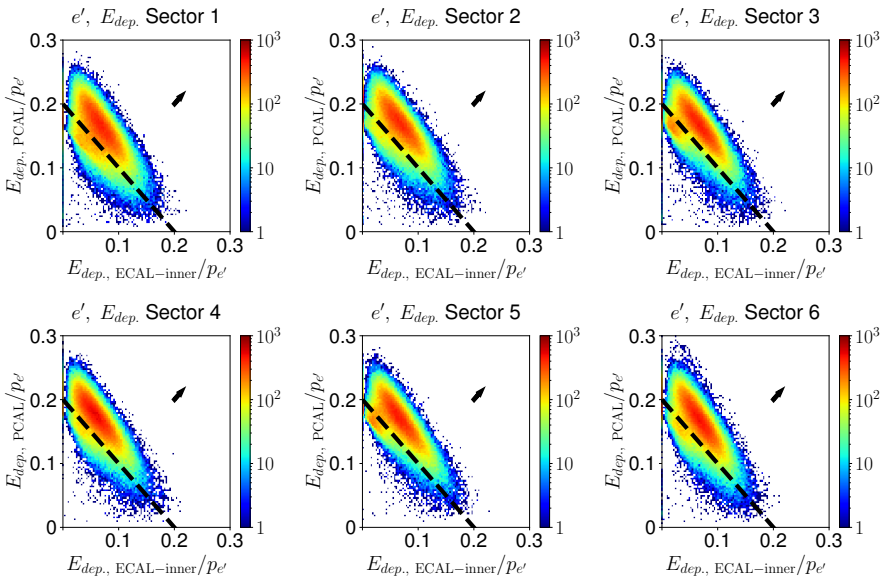

Figure 2-11: The 2D histograms of the fractional SF's $E_{dep.\ \mathrm{PCAL}}/p_{e'}$ vs. $E_{dep.\ \text{EC-inner}}/p_{e'}$ before the RG-A PID cuts. The black arrows in each plot represent the selected region resulting from this cut.

2.4.2 Proton Identification

The proton candidate can be defined from the proton characteristics—a positively charged particle with mass of 938.3 MeV/c^2. As described in Section 2.3, $\chi \equiv \frac{\Delta t_{p',\ measured} - \Delta t_{p',\ expected}(p)}{\sigma_{TOF}}$ is the well-defined signed distance from the theoretical particle identification curve. The proton is the heaviest among the hadrons π, K, p, which are the most abundant in the RG-A environment. The timing differences originate from the mass differences of K ($m_K \sim 500$ MeV) and p ($m_p \sim 938$ MeV) and can effectively identify the proton in the DVCS proton kinematics. Ideally, the positive χ ensures the correct choice of protons because the expected flight times of kaons and pions are always shorter than the proton[1].

The instrumentation articles report that the CTOF can separate p/K up to 0.93 GeV/c at to 3σ level [152], and the FTOF can achieve this performance up to 4.8 GeV/c [139]. As this work analyzes the data with protons up to 1.6 GeV/c momentum level, we do not require a χ cut on the forward detectors. As for the CTOF, we also use the χ cut from the EB service without the additional refinement. The χ cut is adaptively refined by the EB service.

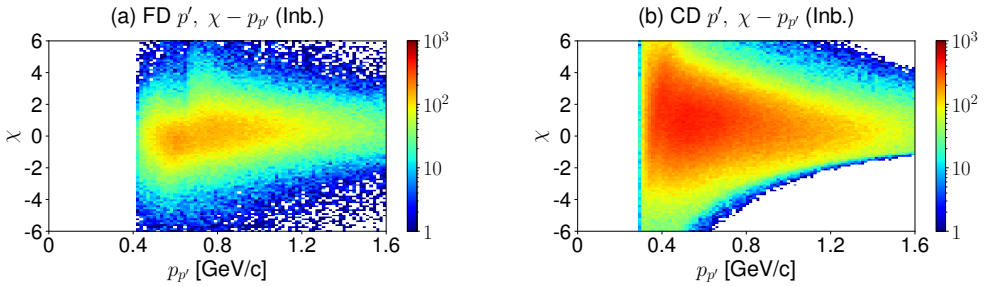

Figure 2-12: The 2D histograms of χ and $p_{p'}$ of the proton candidates for the inbending data set (a: FD, b: CD). Note that the adaptive cuts were already applied by the EB service.

The proton fiducial cuts can be defined in the trackers—DC and CVT. The DC fiducial cuts were developed by the common analysis effort for all three layers and for all polarities, likewise with the electrons (Figs. 2-13–2-14).

[1]The $\pi^{+,-}$ with the negative χ can be regarded as pure for the same reasons.

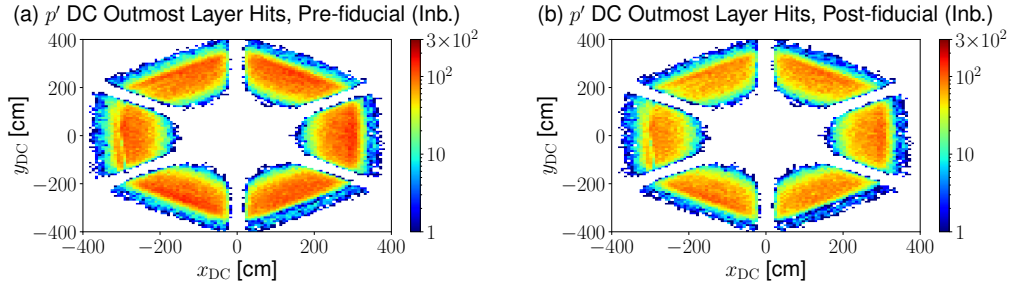

Figure 2-13: The 2D histograms of p' hit positions y_{DC} and x_{DC} of the proton candidate (a) before the RG-A PID cuts and (b) after the cuts for the inbending data set.

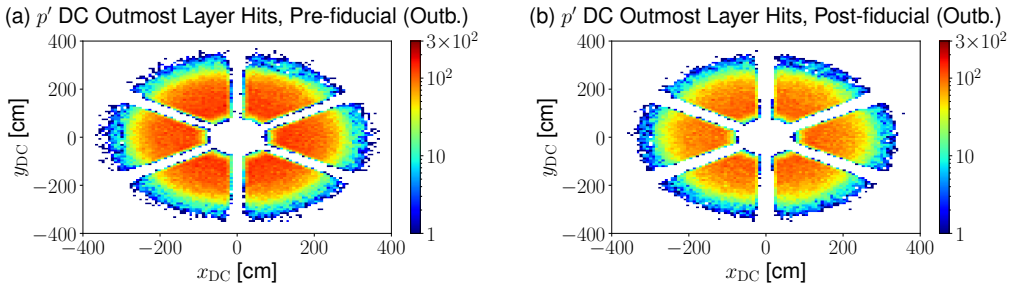

Figure 2-14: The 2D histograms of p' hit positions y_{DC} and x_{DC} of the proton candidate (a) before the RG-A PID cuts and (b) after the cuts for the outbending data set.

The proton selection was enhanced by the fiducial cuts on CVT, the 3σ cuts on χ and 3σ cuts on the vz differences from electron ($vz_{e'} - vz_{p'}$). These are related to improving the determination of the normalization and succeeds the momentum post-processing procedure in Chapter 4. Thus, these selection cuts will be described in Section 5.2.

2.4.3 Photon Identification

The photon is a neutral particle that travels at the speed of light. The most important signature of a photon is that it lacks the associated tracks in the tracker as it has a neutral charge. The nominal photon β is 1 by definition, but we take a conservative limit of $0.9< \beta <1.1$. The lower limit was set up to rule out the neutrons from reactions such as $ep \rightarrow en\pi^+$. The photon fiducial cuts can be defined in the

calorimeters—ECAL and FT-Cal. Likewise with the electron, the photon fiducial cuts were set by $l_{V,W}$ with a tighter lower bound of 14 cm as determined in the RG-A common analysis effort. The PCAL fiducial cut was reinforced by the hit position-based boundary estimation [156]. The effects of the photon fiducial cuts are presented in Figs. 2-15.

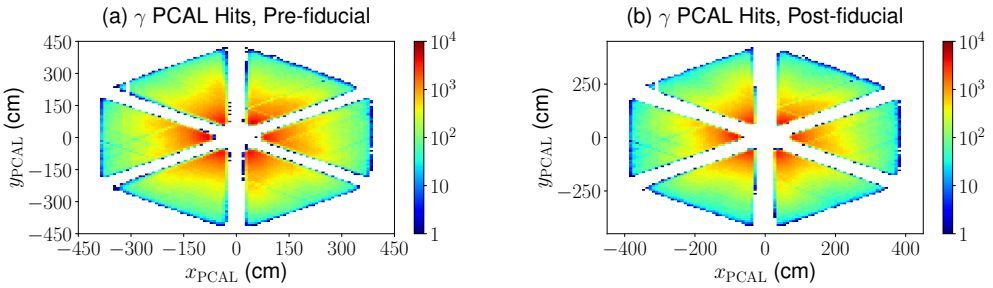

Figure 2-15: The 2D histograms of p' hit positions y_{PCAL} and x_{PCAL} of the photon candidate (a) before the RG-A PID cuts and (b) after the cuts for the concatenated data set of inbending and outbending polarities.

As with the electrons, the photons associated with the inefficient regions in PCAL were excluded. The inefficient regions in FT-Cal were also eliminated. These procedures will be introduced in Section 5.2.

2.5 Data Processing

During RG-A data taking, the event was triggered in parallel by three physics trigger systems: (1) the electron trigger, (2) photoproduction trigger and (3) opposite sector trigger. This analysis focuses on the (inclusive) electron trigger that is designed to record events with FD electron candidates with minimum n_phe, $E_{dep.}$, $E_{dep.\ \mathrm{PCAL}}$ conditions and the geometrical matching between detector subsystems. The electron trigger search was adjusted and performed in parallel for each sector. The electron trigger system is highly efficient with 99.5% trigger efficiency and 95% DAQ livetime for trigger electrons of momentum above 2 GeV/c. The desired event rate for the RG-A experiment is about 20 kHz, which was estimated using the simulation. This can be easily achieved by the CLAS12 trigger logic with the effective performance

level up to 200 kHz [157]. The events triggered by the electron trigger has trigger bits "1" (True) in any of bits 0 to 6, where the bits 1–6 stan for each sector and 0 is their OR. The trigger bits can be accessed offline.

Processing all saved inclusive events is not efficient in many aspects. There are a lot more inclusive events than the exclusive channels of interest, namely DVCS and DVπ^0P. The RG-A has a few skimming modes, trains and wagons, to be commonly used for some specific channels. A train is a coarse skimming, such as the inclusive skim, which requires an electron-proton pair in one event. A wagon is a relatively finer skimming, such as the DVCS wagon, which requires one electron-proton-photon set with some level of DVCS exclusivity. The series of skimming processes is called data cooking. In this analysis, for the base data set we take the DVCS wagon that selects the DVCS candidates with loose exclusivity cuts, and require at least one $e'p'\gamma$ set in the event[158] (see Section 3.3 for the cut conditions).

The raw data is stored in the HIPO format [151] for the enitre CLAS collaboration. The HIPO format has the advantages of fast Input/Output (I/O) speed, and compatibility with the Event I/O (EVIO) format that is commonly used for the Jefferson Lab event storage [159]. For this analysis, the python program with pandas library was taken as the main analysis tool in that python is supported by modern statistical packages [160, 161] that are well maintained. This motivates operation of a custom pipeline to convert the data format to pickle, which is the python standard data format [162]. We use the CLAS12ROOT [163], a software package to read the HIPO format in C++ and store the related information in ROOT format [164]. The ROOT formated data is once again converted to pickle format, using the uproot library [165]. By doing so, the data are reduced into $M \times N$ dimensionality, where M is the number of events, and N is the number of physical quantities and other information that are related (Fig. 2-16).

Different data formats have advantages in different stages of data processing. We filter the base data with the PID cuts introduced at Section 2.4 and save in another HIPO format, because the base data contains all detector responses. The filtered HIPO files are converted into ROOT format. Finally, we execute the python script

to select DVCS and DVπ^0P events with tighter Event Selection criteria that will be described at 3.3 and save them in the pickle format.

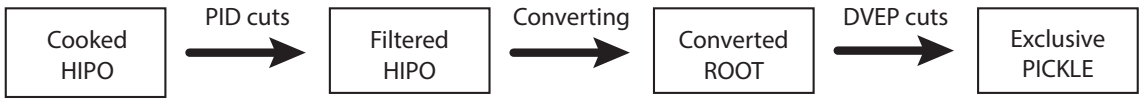

Figure 2-16: The schematic drawing depicting the data processing pipeline.

Chapter 3

Methods

The analysis methods are described in this chapter. This analysis involves detailed consideration of a number of issues: event selection, resolution smearing, momentum corrections and background estimation. A simple example can be found in the missing energy of the entire $e'p'\gamma$ data set. Ideally, the missing energy, defined as the difference of initial and final state total energies, is zero. The experimental $e'p'\gamma$ will produce a blurred distribution around zero due to the finite detector resolution even for the ideal detector. The major background occurs when π^0 events are misidentified as $e'p'\gamma$ by missing the second photon γ_2 from $\pi^0 \rightarrow \gamma_1\gamma_2$. The major background contributions will push the missing energy distribution to the positive side. Another process to modify the distribution is the emission of radiative photons. The missing energy distribution is subject to the energy of radiative photons that are stochastic and greater than or equal to zero. Finally, there is a reconstruction bias that underestimates or overestimates the particle energies. This effect generates a translation of the missing energy distribution. These convoluted effects must be corrected to minimize the systematic uncertainty in the final cross section determination. We introduce the general principle of the analysis technique and describe in detail the analysis steps in this chapter.

3.1 Deep Exclusive Meson Production as an Irreducible Source of Background

As stated in the introduction, the DVCS scattering amplitude is completely coherent with the BH scattering amplitude. We regard both BH and DVCS as a true signal of $ep \to e'p'\gamma$ in this chapter. Thanks to the large acceptance of the CLAS12 detector, all three final states $e'p'\gamma$ are detected within the exclusivity ranges. This advantage, especially in detecting the recoil proton, significantly rules out the SIDIS and resonance decays, as studied in the HERMES experiment [166].

Still, the excluisvie π^0 production is the major source of background because the exclusive event selection is not discriminating enough to distinguish the π^0 misidentified events. It is possible to remove the events with a π^0 when the π^0-decay is correctly identified with two photons. However, it is not uncommon to miss one of the two photons, which is usually inside the BH-DVCS event selection. The mass of the π^0 is 134.9768$\pm$0.005 MeV/c^2 [1], and its square is only 0.0182 (MeV/c^2)^2, which can never be distinguished by a $e'p'$ missing mass squared, $MM^2_{e'p'}$ cut. Therefore, many previous experiments considered the DVπ^0P as the most significant source of backgrounds [107, 111, 118] albeit with slightly different techniques.

Exclusive π^0 production in the DIS region is called Deeply Virtual π^0 Production (DVπ^0P), which is another major channel to access CFFs and an active research topic [167]. The Feynman diagram for the DVπ^0P reaction can be found in Fig. 1-7.

The π^0 background is prevalent not because of the narrow opening angle $\theta_{\gamma_1\gamma_2}$ below the detector resolution, but because the secondary photon escapes the detector (Fig. 3-1). The simulation in the plot refers to the DVπ^0P simulation with selection of events where one photon passes BH-DVCS event selection, and the other is missing in the reconstructed event.

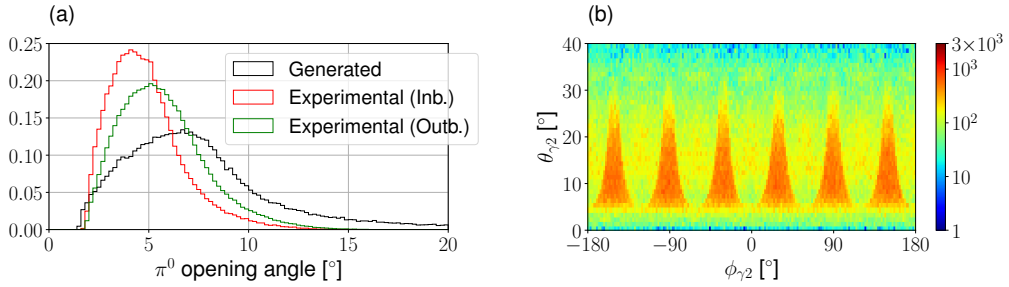

Figure 3-1: The origin of π^0 background events. The left plot contains the normalized histograms that show that the opening angle from the event generator (black) has a minimum around 0.02 rad ($\sim$1.14°) -these are well contained in the experimental data (red, green). The right 2D histogram shows the angular coordinates of the missing photons from the simulation. The plot implies that the missing photon is usually directed towards the region outside the detector fiducial volume. The plot also shows that the photon can be missed inside the detector volume due to detector inefficiency.

3.2 General Analysis Technique

The DVCS analysis involves treating the irreducible background from DVπ^0P background as stated in the introduction. Ignoring negligible backgrounds from the accidentals and other physical processes like DVηP and SIDIS, the 1-dimensional distribution of any physical variable X of a BH-DVCS candidate is expressed as follows:

$$\mathrm{P(X)}^{\mathrm{e'p'}\gamma}_{\mathrm{exp.}} = (1-c) \times \mathrm{P(X)}^{\mathrm{BH-DVCS}}_{\mathrm{exp.}} + c \times \mathrm{P(X)}^{\mathrm{DV}\pi^0\mathrm{P,mis.}}_{\mathrm{exp.}} \tag{3.1}$$

$$\mathrm{P(X)}^{\mathrm{e'p'}\gamma}_{\mathrm{sim.}} = (1-c) \times \mathrm{P(X)}^{\mathrm{BH-DVCS}}_{\mathrm{sim.}} + c \times \mathrm{P(X)}^{\mathrm{DV}\pi^0\mathrm{P,mis.}}_{\mathrm{sim.}} \tag{3.2}$$

where P(X) is the Probability Distribution Function of X with its subscript describing the source of the data set (exp.:experiment, sim.: simulation) and its superscript describing the process involved, along with the contamination ratio c. The superscript of the right hand side $e'p'\gamma$ denotes all processes that pass BH-DVCS event selections including the backgrounds. In reality, instead of the PDF, the sample distribution is known for both the experimental data, and for the MC simulated data set. Up to

statistical fluctuation, the expression

$$n_i(\mathrm{X})^{e'p'\gamma}_{\mathrm{exp.}} = (1-c) \times n_i(\mathrm{X})^{\mathrm{BH-DVCS}}_{\mathrm{exp.}} + c \times n_i(\mathrm{X})^{\mathrm{DV}\pi^0\mathrm{P}}_{\mathrm{exp.}} \tag{3.3}$$

should hold where n_i denotes the i-th bin entry in the histogram of X.

The estimation of the contamination ratio c is directly related to extraction of the signal yields, and thus to the cross section. In this work, the background ratio, or the contamination ratio $c = B/(S+B)$ is estimated by using the event count ratio of DVπ^0P to BH-DVCS either in all bins, or in a certain bin. From the eqn. 3.1,

$$c = N(e'p'\gamma)^{\mathrm{DV}\pi^0\mathrm{P}}_{\mathrm{exp.}} / N(e'p'\gamma)^{e'p'\gamma}_{\mathrm{exp.}} \tag{3.4}$$

$$= [N(e'p'2\gamma)^{\mathrm{DV}\pi^0\mathrm{P}}_{\mathrm{exp.}} \times \frac{N(e'p'\gamma)^{\mathrm{DV}\pi^0\mathrm{P}}_{\mathrm{sim.}}}{N(e'p'\gamma)^{\mathrm{DV}\pi^0\mathrm{P}}_{\mathrm{sim.}}}] / N(e'p'\gamma)^{e'p'\gamma}_{\mathrm{exp.}} \tag{3.5}$$

where $N = \sum_i n_i$ stands for the total sum of entries. This principle of estimating the contamination was used in the previous CLAS12 DVCS analyses [107, 108]. The first term inside the square bracket is the misidentified DVπ^0P events that have passed the BH-DVCS event selection. The sub- and super- script scheme is the same with the PDF case. The eqn. 3.2 requires that the ratio of $e'p'\gamma$ to $e'p'2\gamma$ acceptances is the same for both the simulation and the experimental data. i.e,

$$\frac{N(e'p'\gamma)^{\mathrm{DV}\pi^0\mathrm{P}}_{\mathrm{exp.}}}{N(e'p'\gamma)^{\mathrm{DV}\pi^0\mathrm{P}}_{\mathrm{exp.}}} = \frac{N(e'p'\gamma)^{\mathrm{DV}\pi^0\mathrm{P}}_{\mathrm{sim.}}}{N(e'p'\gamma)^{\mathrm{DV}\pi^0\mathrm{P}}_{\mathrm{sim.}}}. \tag{3.6}$$

The following is not a requirement, but the bin to bin matching of the simulated to the experimental data is desired:

$$\mathrm{P}(\mathrm{X})^{e'p'\gamma}_{\mathrm{exp.}} = \mathrm{P}(\mathrm{X})^{e'p'\gamma}_{\mathrm{sim.}} \tag{3.7}$$

$$\mathrm{P}(\mathrm{X})^{\mathrm{DV}\pi^0\mathrm{P}}_{\mathrm{exp.}} = \mathrm{P}(\mathrm{X})^{\mathrm{DV}\pi^0\mathrm{P}}_{\mathrm{sim.}} \tag{3.8}$$

$$\mathrm{P}(\mathrm{X})^{\mathrm{BH-DVCS}}_{\mathrm{exp.}} = \mathrm{P}(\mathrm{X})^{\mathrm{BH-DVCS}}_{\mathrm{sim.}}. \tag{3.9}$$

Ideally, it is best to ensure the validity of eqn. 3.9 by achieving eqns. 3.7–3.8. This issue will be discussed in Section 4.2 in detail.

3.3 Event Selection

Unlike for the simulation data, where the origin of the events could be controlled, the experimental data was inclusive, i.e., a mixture of all possible channels. Matching the inclusive simulation to the data unnecessarily involves larger systematic uncertainties from the theoretical calculations of total cross sections. This analysis narrows down the selection window of BH-DVCS events that allows irreducible DVπ^0P backgrounds. To validate this two-channel matching, the window must be defined to exclude other backgrounds.

We define the exclusive variables with the four momentum algebra:

$$ME_{e'p'\gamma} = E_{beam} + M - E_{e'} - E_{p'} - E_{\gamma} \tag{3.10}$$

$$MM^2_{e'p'\gamma} = (p_{beam} + p_{target} - p_{e'} - p_{p'} - p_{\gamma})^2 \tag{3.11}$$

$$MM^2_{e'p'} = (p_{beam} + p_{target} - p_{e'} - p_{p'})^2 \tag{3.12}$$

$$MM^2_{e'\gamma} = (p_{beam} + p_{target} - p_{e'} - p_{\gamma})^2 \tag{3.13}$$

$$MPt_{e'p'\gamma} = \sqrt{(p_{beam} + p_{target} - p_{e'} - p_{p'} - p_{\gamma})^2_x + (p_{beam} + p_{target} - p_{e'} - p_{p'} - p_{\gamma})^2_y} \tag{3.14}$$

$$\theta_{\gamma det.\gamma rec.} = \angle(\vec{p}_{\gamma}, \vec{p}_{beam} + \vec{p}_{target} - \vec{p}_{e'} - \vec{p}_{p'}) \tag{3.15}$$

$$\phi_{H\Gamma} = \angle(\vec{H}, \vec{\Gamma}), \tag{3.16}$$

where the hadronic scattering plane is defined as $\vec{H} = \frac{\vec{p}_{e'} \times \vec{p}_{p'}}{|\vec{p}_{e'}||\vec{p}_{p'}|}$, and the photon production plane is defined as $\vec{\Gamma} = \frac{\vec{p}_{e'} \times \vec{p}_{\gamma}}{|\vec{p}_{e'}||\vec{p}_{\gamma}|}$. In the absence of radiative photons, $\vec{H} \parallel \vec{\Gamma}$. The angular variables $\theta_{\gamma det.\gamma rec.}$ and $\phi_{H\Gamma}$ are often referred to as the *cone angle* and *coplanarity*, respectively. Generally, ME, MM^2 and MPt stands for the missing energy, the missing mass squared and the missing transverse momentum, respectively. It is trivial to expect the exclusivity variables for the nonradiated events reconstructed at the perfect resolution: $ME_{e'p'\gamma}, MM^2_{e'p'\gamma}, MM^2_{e'p'}, MPt_{e'p'\gamma}, \theta_{\gamma det.\gamma rec.}, \phi_{H\Gamma} = 0$ and $MM^2_{e'\gamma} = m_p^2$. Another useful variable to control the DVCS kinematics is $\theta_{e'\gamma} = \angle(\vec{p}_{e'}, \vec{p}_{\gamma})$, the angle between the e' and γ, which is used to remove the radiative photon from the electron side.

The first level BH-DVCS event selection was primarily designed by the DVCS wagon service [158] with the following conditions:

- at least one electron, one proton, one photon in the final state.
- $E_{p'} > 0.94358$ GeV
- -1 GeV $< ME_{e'p'\gamma} < 2$ GeV
- 0.25 GeV $< ME_{e'\gamma} < 2$ GeV
- $|MM^2_{e'p'\gamma}| < 0.1$ GeV^2
- $MPt^2_{e'p'\gamma} < 0.75$ (GeV/c)^2
- $\theta_{\gamma_{det.}\gamma_{rec.}} < 7.5^\circ$.

We added several conditions to the DVCS wagon. As discussed in Section 1.2, there are a couple of theoretical constraints on the kinematic regions. We require the events to be in the DIS region, $Q^2 > 1$ (GeV/c)^2 and $W > 2$ GeV. The CFF input for the event generation was provided for $-t < 1.79$ GeV^2, so we have a hard cut at $-t < 1.72$ GeV^2. This is equivalent to $p_{p'} < 1.65$ GeV/c. We set up the thresholds of e' and p' momenta to ensure the reconstruction qualities as $p_{e'} > 2$ GeV/c, $p_{p'} > 0.3$ GeV/c (CD), 0.42 GeV/c (FD, inbending data set), 0.5 GeV/c (FD, outbending data set). The DVCS photon is produced with high momentum. To ensure that the photon threshold does not limit the phase space more than $W > 2$, we take the consevative limit of $p_\gamma > 2$ GeV/c. We also constrain the trigger bits to have at least one "1" $\in \{1, 2, 3, 4, 5, 6\}$, to select the events triggered by the inclusive electron trigger. This operation can be done by the bitwise operation (trigger bit & $1<< n$), where $n \in 1, 2, 3, 4, 5, 6$. Finally, we refine the PID as we discussed the PID techniques at Section 2.4.

We define the DVπ^0P exclusivity variables very similar to the DVCS, but with the two photons $\pi^0 \to \gamma_1\gamma_2$. We keep the convention of $p_{\gamma_1} > p_{\gamma_2}$ to avoid any duplication issue.

$$IM_{\pi^0} = \sqrt{p^2_{\pi^0}} = \sqrt{(p_{\gamma_1} + p_{\gamma_2})^2} \tag{3.17}$$

$$ME_{e'p'\pi^0} = E_{beam} + M - E_{e'} - E_{p'} - E_{\gamma_1} E_{\gamma_2} \tag{3.18}$$

$$MM^2_{e'p'\pi^0} = (p_{beam} + p_{target} - p_{e'} - p_{p'} - p_{\gamma_1} - p_{\gamma_2})^2 \tag{3.19}$$

$$MM^2_{e'p'} = (p_{beam} + p_{target} - p_{e'} - p_{p'})^2 \tag{3.20}$$

$$MM^2_{e'\pi^0} = (p_{beam} + p_{target} - p_{e'} - p_{\gamma_1} - p_{\gamma_2})^2 \tag{3.21}$$

$$MPt_{e'p'\pi^0} = \sqrt{(p_{beam} + p_{target} - p_{e'} - p_{\gamma_1} - p_{\gamma_2})^2_x + (p_{beam} + p_{target} - p_{e'} - p_{\gamma_1} - p_{\gamma_2})^2_y} \tag{3.22}$$

$$\theta_{\pi^0_{det.}\pi^0_{rec.}} = \angle(\vec{p}_{\gamma_1} + \vec{p}_{\gamma_2}, \vec{p}_{beam} + \vec{p}_{target} - \vec{p}_{e'} - \vec{p}_{p'}) \tag{3.23}$$

$$\phi_{H\Pi} = \angle(\vec{H}, \vec{\Pi}), \tag{3.24}$$

where the π^0 production plane $\vec{\Pi}$ was defined as $= \frac{\vec{p}_{e'} \times \vec{p}_{\pi^0}}{|\vec{p}_{e'}||\vec{p}_{\pi^0}|}$, just like for the photon production plane. The invariant mass IM_{π^0} is a strong constraint to define the π^0 events. In the limit of perfect resolution, similarly to the DVCS case, $IM_{\pi^0} = m_{\pi^0}$, $ME_{e'p'\pi^0}, MM^2_{e'p'\pi^0}, MM^2_{e'p'}$, $MPt_{e'p'\pi^0}, \theta_{\pi^0_{det.}\pi^0_{rec.}}, \phi_{H\Pi} = 0$ and $MM^2_{e'\gamma} = m^2_p$.

Similarly, as with DVCS, the first level DVπ^0P event selection was achieved using the DVπ^0P wagon service [168] with the following conditions:

- at least one electron, one proton, two photon in the final state.
- $E_{p'} > 0.94358$ GeV
- $\theta_{e'\gamma_1}, \theta_{e'\gamma_2} > 4^\circ$
- $E_{\gamma_1}, E_{\gamma_2} > 0.15$ GeV
- $\theta_{\gamma_1\gamma_2} > 1^\circ$
- -1.5 GeV $< ME_{e'p'\pi^0} < 2$ GeV
- 0 GeV $< ME_{e'\pi^0} < 2.5$ GeV
- $|MM^2_{e'p'\pi^0}| < 0.1$ GeV^2
- $MPt^2_{e'p'\pi^0} < 1.0$ (GeV/c)^2

- 0.05 GeV$< IM_{\pi^0} <$ 1 GeV
- $\theta_{\pi^0_{det.}\pi^0_{rec.}} <$ 7.5°.

We also require $Q^2 > 1$ (GeV/c)^2 and $W > 2$ GeV to study the background in the DIS region. We demand the DVCS kinematic range, $p_p < 1.6$ GeV/c, $p_{e'} > 2$ GeV/c, $p_{p'} > 0.3$ (CD), 0.42 (FD, inbending data set), (FD, outbending data set). The trigger bits were also constrained to have one "1" $\in \{1, 2, 3, 4, 5, 6\}$, to select the events triggered by the inclusive electron trigger. The PID conditions at Section 2.4 were also applied to the π^0 event selection as well. The 3σ windows of exclusivity variables of DVπ^0P events can be determined without considering the background channel thanks to the very strong experimental trace, IM_{π^0}. The exclusivity variables were fitted for each polarity and topology, just as in the DVCS case.

The next level BH-DVCS event selection was defined by the narrower exclusivity windows for each torus polarity and detector topology. A standard approach is to select 3σ regions of individual exclusivity variables from the MC data set. The MC data set must be a mixture of DVCS and DVπ^0P to encompass a reasonable amount of π^0 background, to satisfy the condition eqn. 3.7 with a reasonable value of c. The next level DVπ^0P event conditions require a good matching of the simulation to the experimental data to ensure eqn. 3.7. Setting the next level exclusivity selections was in practice carried out in an iterative process involving smearing the simulation data resolution and correcting the experimental data at the particle kinematics. The events were selected by smearing the simulation distribution using Gaussian kernels of appropriate effective resolutions. The details of this procedure will be discussed in Section 4.2. The 3σ windows were surveyed by fitting the data set after the momentum post-processing. The final exclusivity cuts will be introduced in Section 5.2.

3.4 Configuration and Kinematics Region

The first level event selections are defined in wider windows than 3σ ranges to avoid excluding good events. This provides a broad outline of the kinematic region before

narrowing down the data selection conditions. The major topologies related to DVCS are (FD, FD), (CD, FD), (CD, FT) where each tuple denote the detector subsystem where each particle (p', γ) were reconstructed. Even though the (FD, FT) topology was totally excluded, Fig. 3-2 shows that the (FD, FT) configuration does not have sufficient statistics to be considered in this analysis.

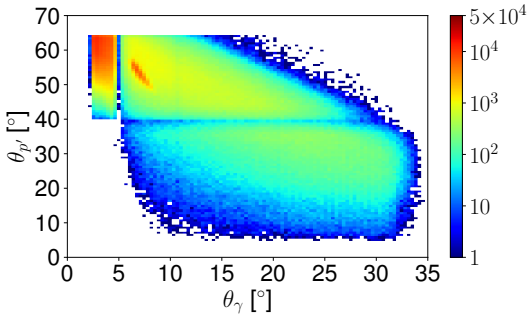

Figure 3-2: The 2D histogram of $\theta_{p'}$ and θ_γ in the concatenated data set for the inbending and the outbending configurations in first level BH-DVCS event selection. There is a correlation that $\theta_{p'}$ increases when θ_γ decreases. This has the consequence that the BH-DVCS data set is concentrated in the three major topologies (FD, FD), (CD, FD), (CD, FT) but not in (FD, FT). The colorbar scale is logarithmic to compensate for the drastic statistics differences in different topologies.

There are six configurations in total because each topology has data for two different torus polarities. The 2D distributions of events in $Q^2 - x_B$ and $-t - \phi$ for each configuration are presented in Figs. 3-3–3-4. It is conventional to define t_{min} and $t_{col.}$, which are the minimum proton momentum transfer and proton momentum transfer at the collinear limit [76, 82], respectively:

$$-t_{min} = Q^2 \frac{2(1-x_B)(1-\sqrt{1+\epsilon^2})+\epsilon^2}{4x_B(1-x_B)+\epsilon^2} \tag{3.25}$$

$$-t_{col.} = -Q^2(Q^2 - x_B s)/(x_B(Q^2 - s)), \tag{3.26}$$

with other variables defined in Chapter 1. These reference momentum transfers are subject to x_B and Q^2, and it is convenient to visualize them in the $Q^2 - x_B$ plane (Figs. 3-5–3-6).

The copious radiative photons emitted in the direction of the scattered photons

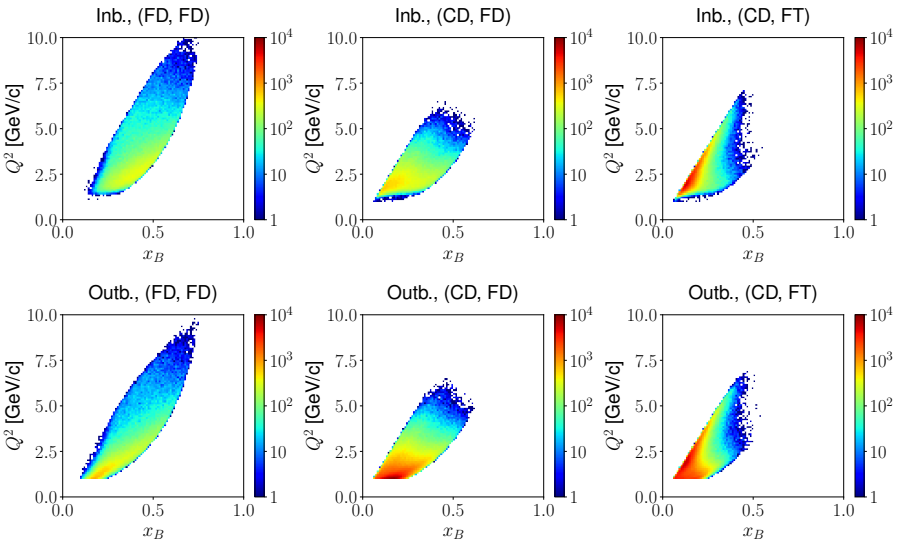

Figure 3-3: The 2D histograms of events in Q^2 and x_B for each configuration of first level BH-DVCS events. The color bar scale is logarithmic.

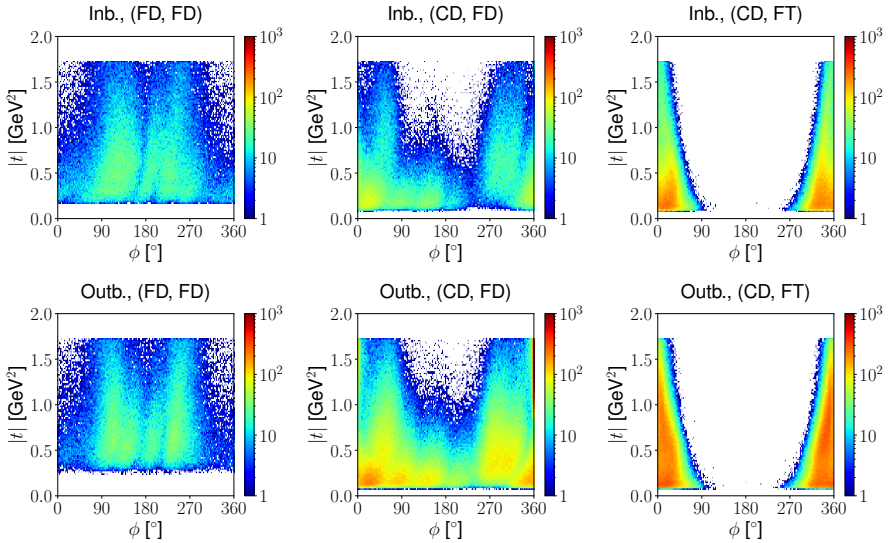

Figure 3-4: The 2D histograms of events in $-t$ and ϕ for each configuration of first level BH-DVCS events. The color bar scale is logarithmic.

can be controlled by inserting a threshold for the cone angle between the scattered electron and the photon $\theta_{e'\gamma}$. The 2D histograms of $\theta_{e'\gamma} - \theta_{e'}$ are shown in Fig. 3-8 without any regulation. The outbending data set contains especially many events with the p-peak events with low $\theta_{e'\gamma}$. This corresponds to the collinear limit, where the u-channel propagator $\mathcal{P}_1(\phi)$ in eqn. 1.42 is peaked at $\phi = 0$ or 2π. In the BMK

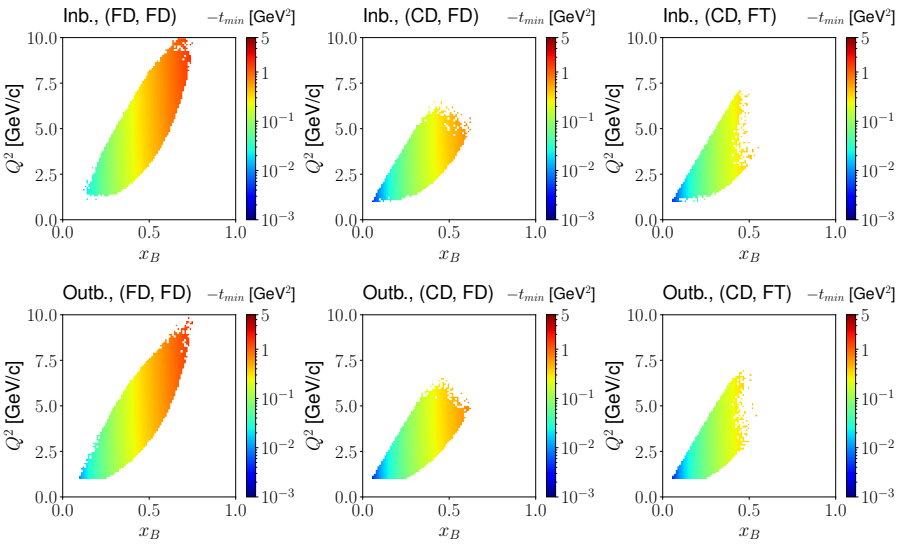

Figure 3-5: The 2D heatmap visualizing $-t_{min}$ in Q^2 and x_B plane for each configuration of first level BH-DVCS events. The color bar scale is logarithmic.

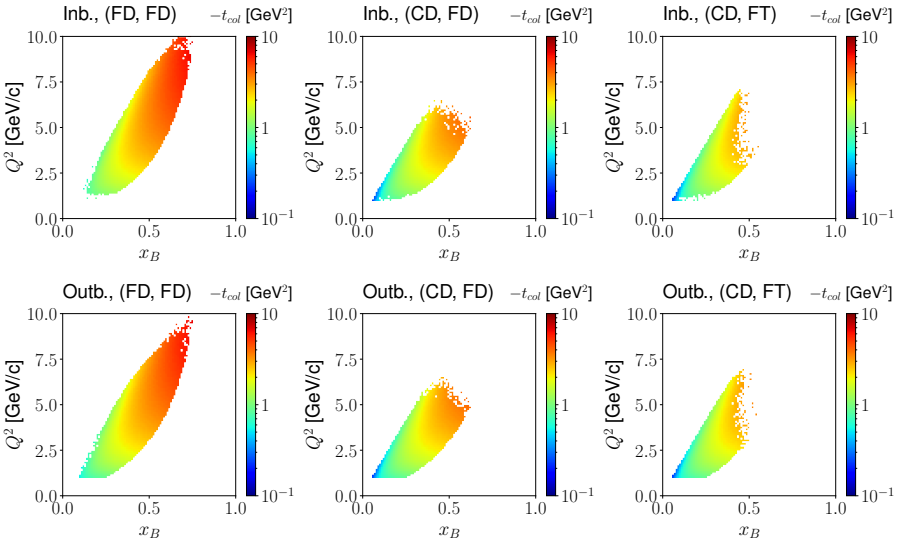

Figure 3-6: The 2D heatmap visualizing $-t_{col}$ in Q^2 and x_B plane for each configuration of first level BH-DVCS events. The color bar scale is logarithmic.

approximation [76], the azimuthal angle ϕ_{BMK} is related to ϕ as follows:

$$\phi_{\mathrm{BMK}} = \pi - \phi. \tag{3.27}$$

The u-channel propagator singularity corresponds to $\phi_{\mathrm{BMK}}{=}\pi$. While following the

BMK model conserves the sign convention in the original paper, we choose to express the cross section in the Trento convention, which is consistent with the previously published experimental results, and also with many SIDIS papers.

The current detector reconstruction performance is not guaranteed when there are electron and photon signals in the same sector of the FD ECAL [169]. After the sectors of e' and γ are required to be different in FD or reconstructed in different subsystems (i.e. γ's in FT), the 2D histograms of $\theta_{e'\gamma} - \theta_{e'}$ remove a significant amount of events at low $\theta_{e'\gamma}$ (Fig. 3-8). The dotted curves define the 3σ region around the peaks w.r.t. $\theta_{e'}$. The events with e' and γ in the same sectors, that have been removed, have ϕ around 0 and 2π, as expected (Fig. 3-9). The (CD, FT) configuration accommodates abundant low $\theta_{e'\gamma}$ events, especially in the outbending data. The 3σ window for such events was separately defined and these events were incorporated into the (CD, FT) configuration.

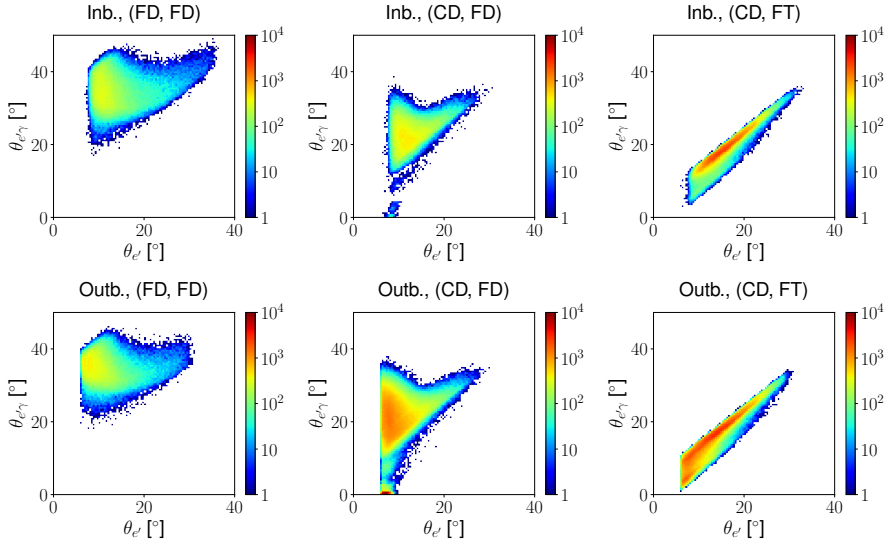

Figure 3-7: The 2D histograms of events in $\theta_{e'\gamma}$ and $\theta_{e'}$ for each configuration of first level BH-DVCS events without regulation of $\theta_{e'\gamma}$. The color bar scale is logarithmic.

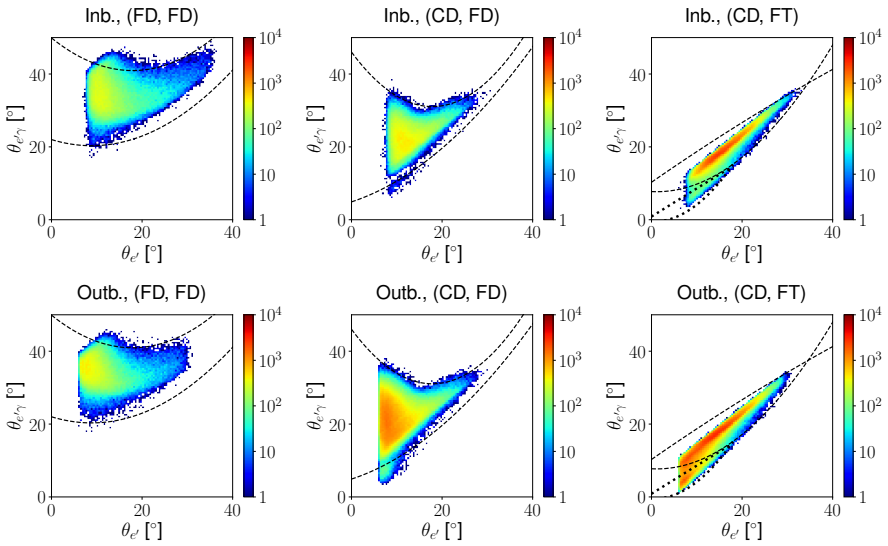

Figure 3-8: The 2D histograms of events in $\theta_{e'\gamma}$ and $\theta_{e'}$ for each configuration of first level BH-DVCS events with the condition that the sectors of e' and γ are different. The color bar scale is logarithmic.

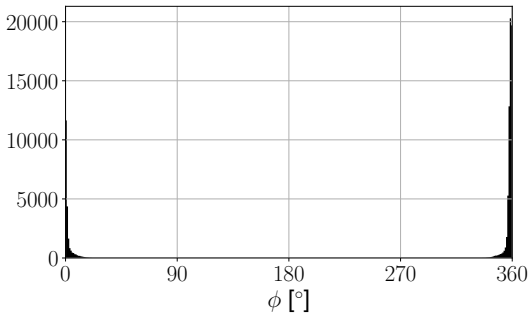

Figure 3-9: The 1D histogram of events vs. ϕ in (p, γ, polarity) = (CD, FD, +1) of first level BH-DVCS events when the electrons and the photons were reconstructed in the same sector.

3.5 Cross Section Extraction

The entire analysis chain process can be summarized as *the inverse problem*, which is the transformation of the observed event counts to the number of physical $BH - DVCS$ events. Had the number of reconstructed events been only 10% of the number of the generated events in the simulation chain, the signal yield in reality must then be ten times the observed event counts. The probability distribution that the observed event counts follows is deformed by the emission of the radiated photons, which is

taken into account by *the radiative corrections*. The extracted cross section is the differential cross section in one specific bin, not for the one fixed kinematics. To be directly compared with the BH prediction, either the data, or the fixed kinematics of the BH curve must be corrected.

3.5.1 Simulation Pipeline

The simulation technique uses the standard Monte-Carlo (MC) simulation, or MC in short. The simulation data was used to estimate the proton energy loss and improve the data quality by matching the simulation to data.

The simulation follows the standard procedure to generate events and simulate the effects arising from the detector and the reconstruction process. The event generators used in this work are the *dvcsgen* [170] for the BH-DVCS simulation and and *aao_gen* [171] for the DVπ^0P. The working principles of both generators have been proven previously [107, 167]. The *dvcsgen* was firstly developed in the early CFF paper [172] following the development of the BMK approximation [76]. The VGG CFF grid was updated for the *dvcsgen* code later [109]. The *aao_gen* program generates DVπ^0P events with the structure function tuned to agree with recent measurements [173, 174]. The generated events are rejection-sampled based on the multidimensional probability distribution, which is the normalized differential cross section.

The generated events were detector simulated using GEANT4 [175] with the GEANT4 Monte-Carlo (GEMC), the CLAS12-friendly API of the GEANT4 [176]. The code GEMC simulates the interactions and secondary particle generations using the seed of the generated particles. GEMC saves the detector responses in the same format as used for the experimental data. These responses are processed in the same way as the experimental data processing and are provided as an input to reconstruct particles using the CLAS12 event Reconstruction and Analyses (CLARA) [177]. The trigger bit is fixed to '0' for the simulated events.

The raw reconstruction efficiency in the simulation chain is much higher compared to that in the real experiment. This is because the copious background prevalent in the real experimental environment increases the DC occupancy especially in the

region 1 (the innermost layers) and significantly drops the efficiency. The reduction in efficiency is estimated using the multiplicities $n_{\pm} = N_{\pm}/N_{e'}$, where $N_{\pm}$ are the number of the positive (+) and the negative (-) particles, and $N_{e'}$ is the total number of electron events in the run. The efficiency $\eta(I)$ is defined as the ratio of multiplicity at the beam current I to the extrapolated multiplicity at $I = 0$. The study [178] shows that the efficiency decreases with increasing beam current as -0.32% and -0.37% per nA for both positively and negatively charged particles. The background detector responses from the randomly triggered experimental data were mixed with the GEMC signal detector responses to include this effect. The random trigger is not related to any physics-related trigger logic, but takes data at random frequency [157]. The mixing procedure with the random trigger events is called the *background merging*. The background merging was developed for different currents that were requested for the actual experiments. The inbending data set has the background merging configuration of 45, 50 and 55 nA, and the outbending data set has 40 nA and 50 nA. The initial outbending data with +1.00796 times higher torus current than the nominal current can be simulated with the 40 nA background merging. In this analysis, we simulate the "production" simulation with 50 nA background merging of 500M generated BH-DVCS events and 300M DVπ^0P events. To study the systematic effects arising from the reconstruction inefficiency, we simulated 100M vents for other configurations with background merging of different currents, and also without background merging.

3.5.2 Acceptance Correction

The purpose of the acceptance correction is to convert the number of observed events to the number of physical events at the vertex. If the detector efficiency is 100%, only the geometric factors define the acceptances. While it is conventional to distinguish the effect of the detector efficiency ε from the geometric factor, it is elusive in practice. The common method uses the detector simulation by GEANT4 to extract the detector

acceptance *Acc.* as follows:

$$Acc.(x_B, Q^2, -t, \phi) = \frac{N_{rec.}(x_B, Q^2, -t, \phi)}{N_{gen.}(x_B, Q^2, -t, \phi)}, \tag{3.28}$$

where $N_{rec.}$ is the event count of the reconstructed events, and $N_{gen.}$ is the number of generated events from the event generator. The caveat is that the reconstructed kinematic coordinates $(x_B, Q^2, -t, \phi)$ differ from the true values $(x_B, Q^2, -t, \phi)$. It is indeed problematic when the encoded bin number from the generated $(x_B, Q^2, -t, \phi)$ is different from the bin number from reconstructed $(x_B, Q^2, -t, \phi)$. This effect is called *bin migration*. To cope with bin migration, several high energy experiments devised the computational method known as *matrix unfolding*. In our case, the bin purity, the conditional probability to occupy the same bin number as the generated bin number, is high enough that the acceptances cane be used to determine the reconstruction efficiency at simulation. To trust the *Acc.* and to minimize the uncertainty from the bin migration, it is required to ensure that the distribution of reconstructed events both from the simulation and from the experiment are in reasonable agreement. The BH-DVCS total cross section roughly follows the BH profile. To complete this method, there must be a study to compare the efficiency using GEANT4 to the actual value in the experiment.

The experiment uses the three detector configurations for both polarities. To merge the counts from the three subsystems, we strictly divide the detector subsystems into four domains: (0) $\theta_{p'} < 40^\circ$ and $\theta_\gamma < 5^\circ$, (1) $\theta_{p'} < 40^\circ$ and $\theta_\gamma \geq 5^\circ$, (2) $\theta_{p'} \geq 40^\circ$ and $\theta_\gamma \geq 5^\circ$, (3) $\theta_{p'} \geq 40^\circ$ and $\theta_\gamma \geq 5^\circ$. The configurations (0), (1), (2), and (3) are likely to be detected in (FD, FT), (FD ,FD), (CD, FD) and (CD, FT) configurations, respectively. As mentioned in Section 3.4, there are not enough statistics in the (FD, FT) configuration to define the event selection at the reconstructed phase space. Another remark is that there is an overlap in θ range of the FD protons and CD protons due to the overlap in geometry of the CVT-CTOF and DC-FTOF2. In lieu of counting all marginal statistics in the overlapped fiducial regions, we strictly divide the CD proton and FD proton polar angle regions at 40° so that the acceptances can

be quantified per configuration.

3.6 Radiative Corrections

The Radiative Correction (RC) is an essential aspect of any QFT to match the theoretical cross section to the experimental one. The RC was initially developed to cancel the infrared (IR) divergence in physical quantities, *e.g.* cross sections. In short, any experiment cannot detect the Born cross section of tree-level processes as is, because this diagram is in interference with the next order diagrams that include the soft Bremsstrahlung and vertex corrections [3].

The soft photon emission in the direction of the incoming or outgoing electron dominates in the typical electron scattering experiment. The early calculation was carried out with the inclusive electron scattering propagator, treating the peaking approximation carefully [179]. We take the s-peak as the soft photon emission in the direction of the beam, and the p-peak in the direction of e'.

In 2018, the RC study for the exclusive BH-DVCS reaction was carried out within the peaking approximation [180]. There are many advantages to using the results of this study. Firstly, the MC code the authors used has the same technical structure as *dvcsgen* [172]. Secondly, unlike for the inclusive electron RC that inevitably changes x_B and Q^2, the RC factors and the peaking approximations were carried out at fixed x_B and Q^2, which is extremely convenient for the experimentalist. Formally,

$$Q^2 \equiv (p_{e'} - p_{beam})^2 \tag{3.29}$$

$$x_B \equiv \frac{Q^2}{2M\nu}, \tag{3.30}$$

where Q^2 is no longer identical with $-q^2$ in the presence of the radiative photon γ'. The RC code was implemented to use the existing *dvcsgen* that was designed for the CLAS12 environment [170].

The RC impacts the experiment significantly in three ways. Firstly, it transforms (corrects) the differential cross section that the sampled MC distribution follows.

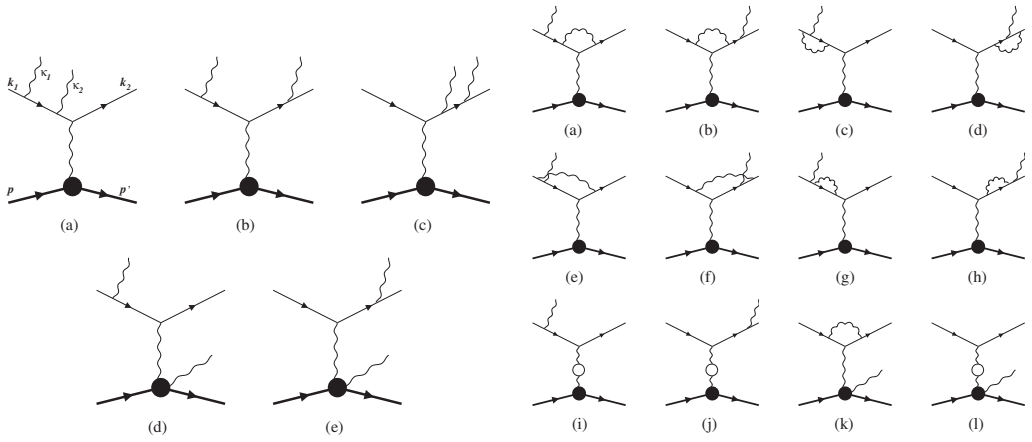

Figure 3-10: The next order Feynman diagrams related to RC calculations. The original image was imported from [180].

Secondly, it really generates the radiative photons at s-peak or p-peak. Especially, the p-peak photon can affect the reconstruction quality of e'. Lastly, the extracted cross section must be RC corrected to the Born cross section and compared with the theoretical calculation. The RC factor F_{rad} is defined as $\frac{d\sigma_{obs.}}{d\sigma_{Born}}$ [181], where $d\sigma_{obs.}$ is the observed cross section and $d\sigma_{Born}$ is the tree-level cross section.

The *dvcsgen* and *aao_gen* generators stochastically generate the radiative soft photons γ' at s-peak and p-peak. The event without the soft photon is dubbed as the "nonradiated" event. The partial cross section for the nonradiated event is not the same with $d\sigma_{Born}$ due to the virtual correction. The differential cross section and RC factor at specific (x_B, Q^2, $-t$, ϕ) can be calculated using *dvcsgen* with or without performing event generation.

3.6.1 Monte Carlo Estimators

The extracted cross section data will be compared with the theoretical prediction at the fixed kinematics. The experimentally determined cross section is the integrated cross section in the bin. The mean value theorem for integrals states that there can exist a kinematics within the bin volume that has

$$d\sigma((x_B)^*, (Q^2)^*, (-t)^*, (\phi)^*) = < d\sigma(x_B, Q^2, -t, \phi) > |_{bin} \ . \tag{3.31}$$

However, it does not provide the specific values of $((x_B)^*, (Q^2)^*, (-t)^*, (\phi)^*)$. Traditionally, the RC factors are calculated within the bin, which contributes another uncertainty when performing the corrections for the binned data. The Monte Carlo Estimator (Horvitz–Thompson estimator) F_N, which is defined for estimating the integration $\int dAf(x_B, Q^2, -t, \phi)$ using the MC sample, is defined as follows [182, 183].

$$F_N = \frac{1}{N} \sum_{i=1}^{N} \frac{f(x_B, Q^2, -t, \phi)}{p(x_B, Q^2, -t, \phi)} \ . \tag{3.32}$$

The subscript N is to denote the number of samples in the MC data set. The mean value of F_N is the estimator for the integration, i.e.,

$$< F_N > = E\left[\frac{1}{N} \sum_{i=1}^{N} \frac{f(x_B, Q^2, -t, \phi)}{p(x_B, Q^2, -t, \phi)}\right] \sim \int dAf(x_B, Q^2, -t, \phi). \tag{3.33}$$

The differential volume dA is given as $dx_B dQ^2 d(-t) d\phi$. In this analysis, the PDF $p(x_B, Q^2, -t, \phi)$ is unknown, but is proportional to $d\sigma_{MC,obs.}(x_B, Q^2, -t, \phi)$.

$$p(x_B, Q^2, -t, \phi) = \frac{\frac{d\sigma_{MC,obs.}}{dx_B dQ^2 d|t| d\phi}(x_B, Q^2, -t, \phi)}{\int dA \frac{d\sigma_{MC,obs.}}{dx_B dQ^2 d|t| d\phi}(x_B, Q^2, -t, \phi)}. \tag{3.34}$$

The average of the variable k is

$$< k > = \int dAp(x_B, Q^2, -t, \phi)k = \frac{\int dA \frac{d\sigma_{MC,obs.}}{dx_B dQ^2 d|t| d\phi}(x_B, Q^2, -t, \phi)k}{\int dA \frac{d\sigma_{MC,obs.}}{dx_B dQ^2 d|t| d\phi}(x_B, Q^2, -t, \phi)}. \tag{3.35}$$

Each integration in the eqn. 3.35 can be estimated by eqn. 3.33, and eqn. 3.35 is reduced to

$$< k > = \sum_{i=1}^{N} k_i/N + O(1/\sqrt{N}). \tag{3.36}$$

The average weight (cross section) $\bar{d\sigma}$ is

$$\bar{d\sigma} = \frac{\int dA \frac{d\sigma_{MC,obs.}}{dx_B dQ^2 d|t| d\phi}(x_B, Q^2, -t, \phi)}{\int dA} \tag{3.37}$$

$$= N / \left[\sum_{i=1}^{N} 1 / \frac{d\sigma_{MC,obs.}}{dx_B dQ^2 d|t| d\phi}_i \right] . \tag{3.38}$$

The estimation of the Born cross section is,

$$\frac{d\sigma}{dx_B dQ^2 d|t| d\phi} = \frac{N(e'p'\gamma)^{e'p'\gamma}_{\text{exp.}} - N(e'p'\gamma)^{\text{DV}\pi^0\text{P}}_{\text{sim.}}}{Acc. \times F_{rad} \times F_{bin} \times F_{eff.} \times L}, \tag{3.39}$$

where the last correction F_{bin} is introduced for the finite bin size correction to convert the average cross section (observed) to the cross section at fixed kinematics. The global efficiency $F_{eff.}$ is the detector performance compared to that determined in the simulation using GEANT4. The integrated luminosity L can be estimated by the Faraday cup data. The radiative corrections and the finite bin size corrections have been done independently. We take advantage of the *dvcsgen* that saves the observed cross section $\frac{d\sigma_{MC,obs.}}{dx_B dQ^2 d|t| d\phi}(x_B, Q^2, -t, \phi)$, and the Born cross section $\frac{d\sigma_{MC,Born}}{dx_B dQ^2 d|t| d\phi}(x_B, Q^2, -t, \phi)$ at the same time. In principle,

$$F_{rad} = \frac{\bar{d\sigma}_{obs.}}{\bar{d\sigma}_{Born.}} \tag{3.40}$$

$$F_{bin} = \frac{\bar{d\sigma}_{Born.}}{d\sigma_{Born.}(< x_B >, < Q^2 >, < -t >, \phi)} \tag{3.41}$$

$$F_{rad} \times F_{bin} = \frac{\bar{d\sigma}_{obs.}}{d\sigma_{Born.}(< x_B >, < Q^2 >, < -t >, \phi)} . \tag{3.42}$$

It is important to have a good estimate of $\frac{d\sigma_{MC,obs.}}{dx_B dQ^2 d|t| d\phi}(x_B, Q^2, -t, \phi)$ in the event generator to minimize the bias from choosing an unrealistic model.

Chapter 4

Data Post-Processing

In this chapter, we describe the post-processing of the data based on the simulation. We first corrected the energy loss of the proton using the simulation data. After applying the proton loss corrections to the experimental data and the simulation, we reduced the reconstruction bias by correcting the single particle kinematics in the experimental data. To match the resolution, the kinematics of the simulated data was smeared.

4.1 Energy Loss Correction for Charged Particles

A charged particle loses its energy through its passage through material via ionization and radiation [1]. This causes an underestimation of the individual charged particle energy, a shift in the polar angle, and further affects the event selection on the exclusive channels.

We followed convention to define the deviation δ as the reconstructed value subtracted from the generated, or the true value, i.e. $\delta p \equiv p_{gen.} - p_{rec.}$. In this way, we could simply add δ values to the original reconstructed values, i.e. the corrected momentum is simply, $p_{rec.} + \delta p$. The configuration used for the simulation is rga fall 2018 for both gemc and reconstruction. The polarity was defined over the electron trajectory so that the inbending and the outbending corresponded to a toroidal magnetic field of -100% and +100% respectively. Also, if not denoted, p means the

reconstructed momentum.

4.1.1 Electron Energy Loss

The deviation of electron momentum variable due to energy loss is smaller and more centered than that for the proton energy loss. Thus, we focus on the proton energy loss. The distributions of variables of the electrons are presented below.

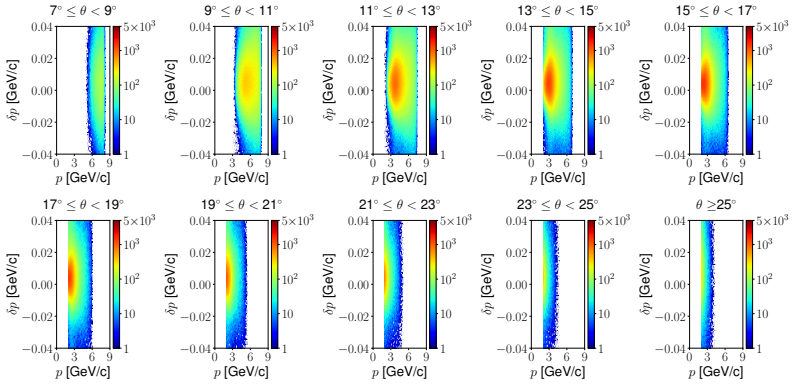

Figure 4-1: The distributions of reconstructed momenta from the generated momenta δp vs. the reconstructed momentum p of the electrons for the inbending polarity. Each panel corresponds to electrons in the selected polar angle range, which is specified in each title.

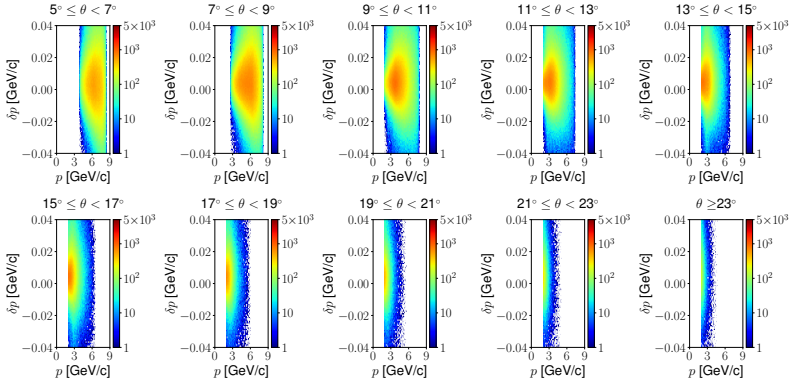

Figure 4-2: The distributions of reconstructed momenta from the generated momenta $\delta p's$ vs. the reconstructed momentum p's of the electrons for the outbending polarity.

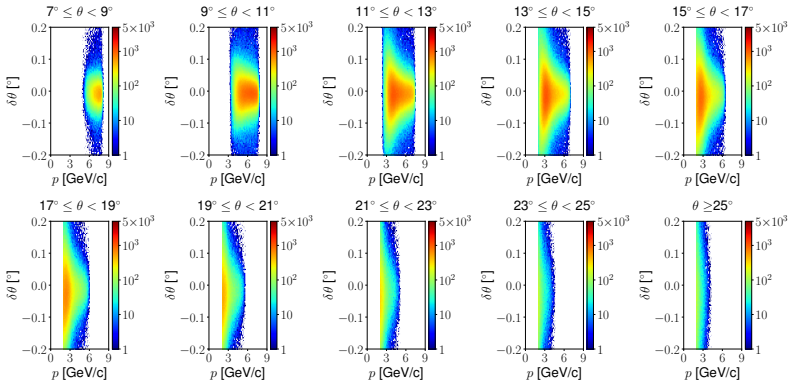

Figure 4-3: The distributions of reconstructed polar angles from the generated polar angles $\delta\theta$'s vs. the reconstructed momenta p's of the electrons for the inbending polarity.

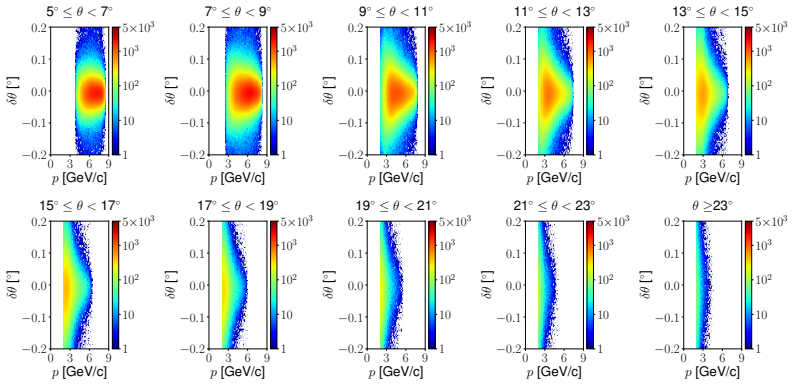

Figure 4-4: The distributions of reconstructed polar angle from the generated polar angle $\delta\theta$ vs. the reconstructed momenta p's of the electrons for the outbending polarity.

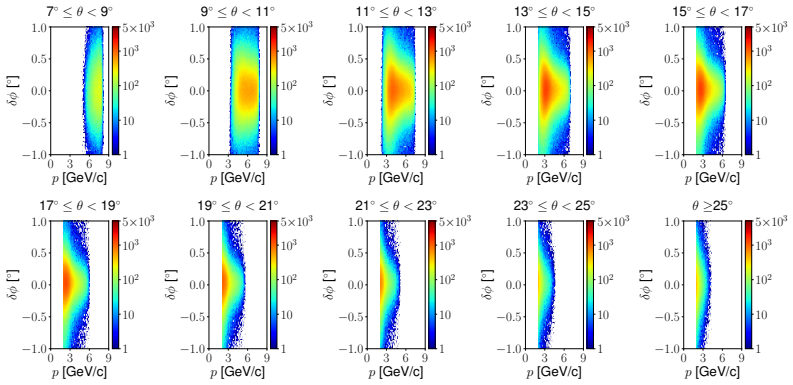

Figure 4-5: The distributions of reconstructed azimuthal angle from the generated azimuthal angle $\delta\phi$'s vs. the reconstructed momenta p's of the electrons for the inbending polarity.

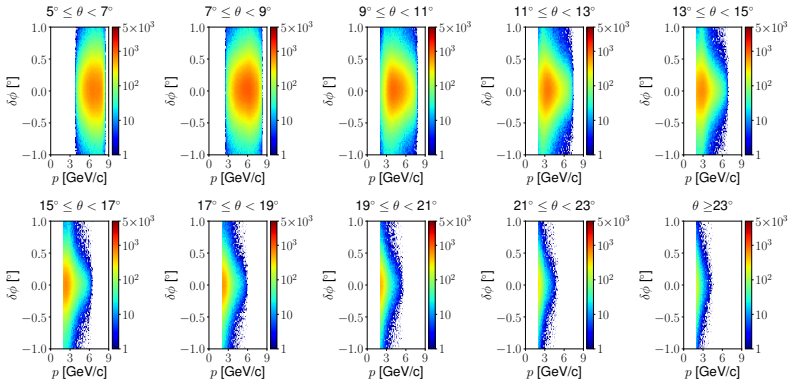

Figure 4-6: The distributions of reconstructed azimuthal angle from the generated azimuthal angle $\delta\phi$'s vs. the reconstructed momenta p's of the electrons for the out-bending polarity.

4.1.2 Detector Regions for Proton Energy Loss Correction

The proton energy loss can be effectively characterized by the reconstructed momentum, polar angle and azimuthal angle. This is because proton energy loss depends on its trajectories. As the protons are independently reconstructed in FD and CD, the proton data set is firstly divided into the FD and CD protons for the energy loss correction. The FD protons are further divided into two categories. The outer trajectories penetrate the CVT material, which is thicker than for the case of the inner trajectories. This results in the ambiguous overlap of two bands at $\delta p - p$ for the FD protons as shown in the Fig. 4-7-a. The two bands will be called the upper and lower band, where the upper band has the higher δp values at the low p region.

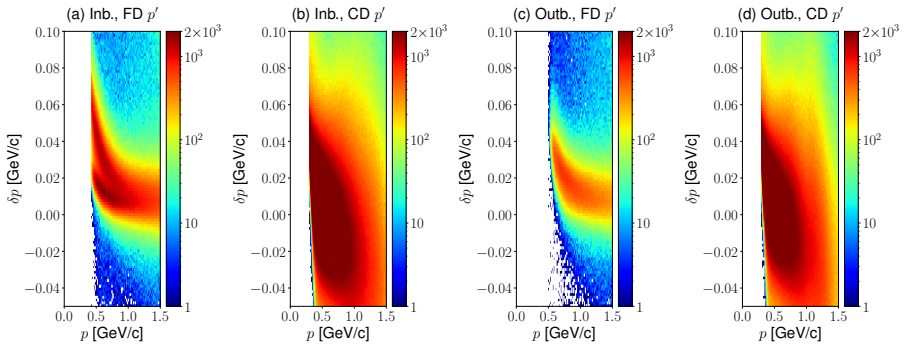

Figure 4-7: The distributions of reconstructed momenta from the generated momenta δp's vs. the reconstructed momenta p's of the protons in all polarity configurations. The protons can be reconstructed from the forward detector hits in (a) the inbending polarity and (b) the outbending polarity, and from the central detector hits in the (c) inbending polarity, and the (d) outbending polarity.

The simulation data points $(p, \delta p)$ at $\delta p - p$ plane are roughly split by the curve $\delta p = \frac{0.088}{p_{rec.}^{1.5}}$ for the FD protons. This type of classification is presented in Fig. 4-8. The top and bottom row plots in Fig. 4-8 show the upper and lower band respectively. This curve is not retrieved at the experimental data set as $p_{gen.}$ is not accessible, and neither is δp. Each band raises the possibility that they are alternatively separated by either $\theta_{rec.}$, or by the local hit position, $\theta_{\mathrm{DC,region1}}$. The fundamental reason that these bands appear is that the tracks lose energy in the CVT (See Section 4.1.3). Thus, it is more reasonable to use the most sensitive detector to CVT energy loss,

i.e., DC region 1, the closest to the central detector. The following condition is used to make a separation by $\theta_{\mathrm{DC,region1}}$ presented in Fig. 4-9.

$$\theta_{\mathrm{DC,region1}} \begin{cases} < -53.1468 + 79.6131 \times (p - 0.3)^{0.05739} & \text{(lower band)} \\ \geq -53.1468 + 79.6131 \times (p - 0.3)^{0.05739} & \text{(upper band)} \ , \end{cases} \tag{4.1}$$

where $\theta_{\mathrm{DC,region1}}$ is defined by $\tan^{-1}(\frac{\sqrt{x^2+y^2}}{z})$ in degrees, and x, y, z are the hit positions of the DC 1 (layer 6).

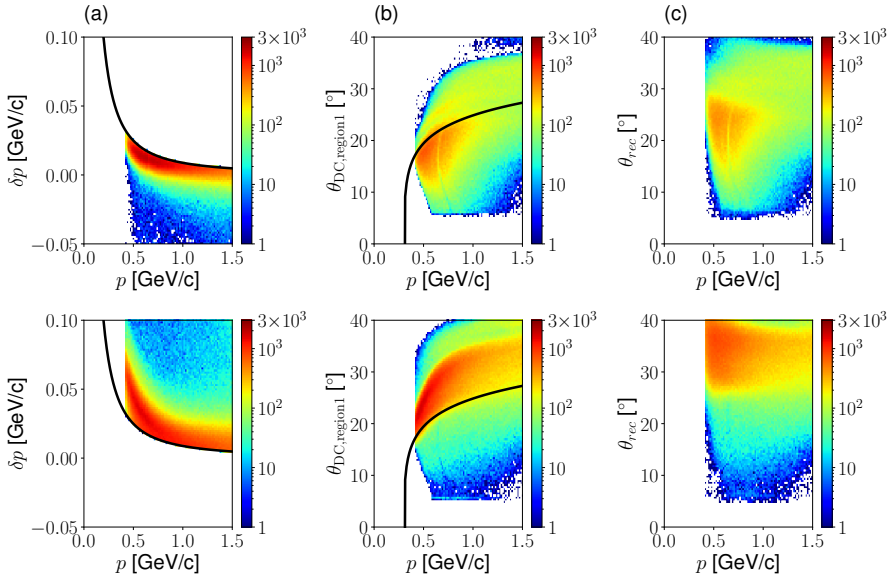

Figure 4-8: The plots in the first column: δp vs. p, the middle column: $\theta_{\mathrm{DC,region1}}$ vs. p, and the last column: $\theta_{rec.}$ vs. p. The top row plots are from the lower band and the bottom row plots are from the upper band where the band is defined over the curve in δp vs. p plot.

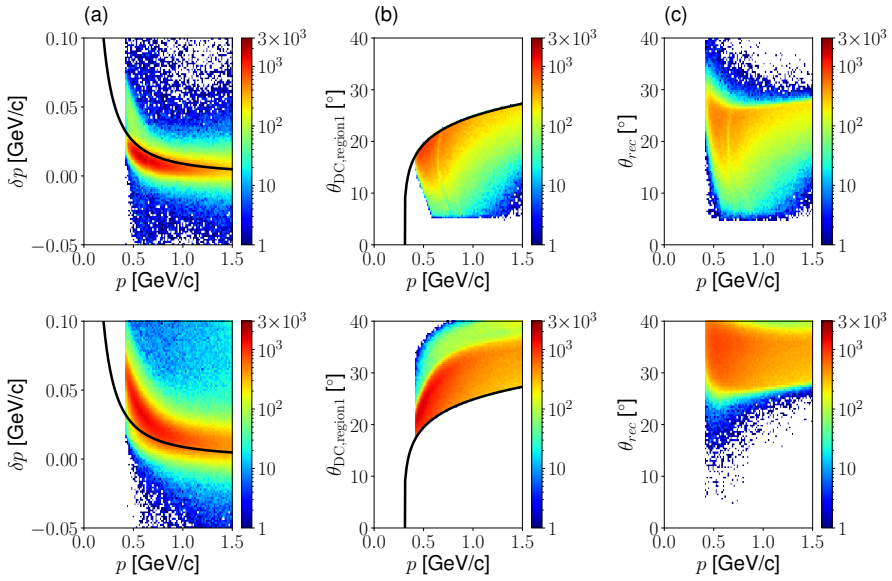

Figure 4-9: The plots in the first column: δp vs. p, the middle column: $\theta_{\mathrm{DC,region1}}$ vs. p, and the last column: $\theta_{rec.}$ vs. p. The top row plots are from the lower band and the bottom row plots are from the upper band where the band is defined over the curve in $\theta_{\mathrm{DC,region1}}$ vs. p plot.

4.1.3 Details of the Two-Band Issue

A follow-up study has been performed with the aim of understanding the reason for the two reconstruction bands appear. From Fig. 4-9, the differences in δp can originate either from the differences in the energy loss in material thickness or from the reconstruction bias. The configuration files used for the GEMC [176] called the gcards have been set up for each experimental configuration [184]. Each detector component like the CVT is encoded in the gcards as an xml format. By deleting the correponding lines, the interested detector can be removed in the geant4 simulation.

A simulation of 500 MeV/c momentum protons, where the band issue is the most prominent, has been carried out in the forward detector region for inbending polarity. The possible origins of the two bands in the central detectors are selectively turned on and off. They include the CTOF, CND, CVT. In conclusion, removing CTOF or CND did not produce any significant changes from the reference result. However, removing CVT resolved the two band issue. This effect is a sum of energy loss from the BMT and the SVT (Fig. 4-10).

Another possibility is that the bands can be due to a reconstruction bias. This was studied by removing the central detector in a yaml file, another configuration file for the CLARA, reconstruction software suite [177]. It was found that there was no difference from the reference.

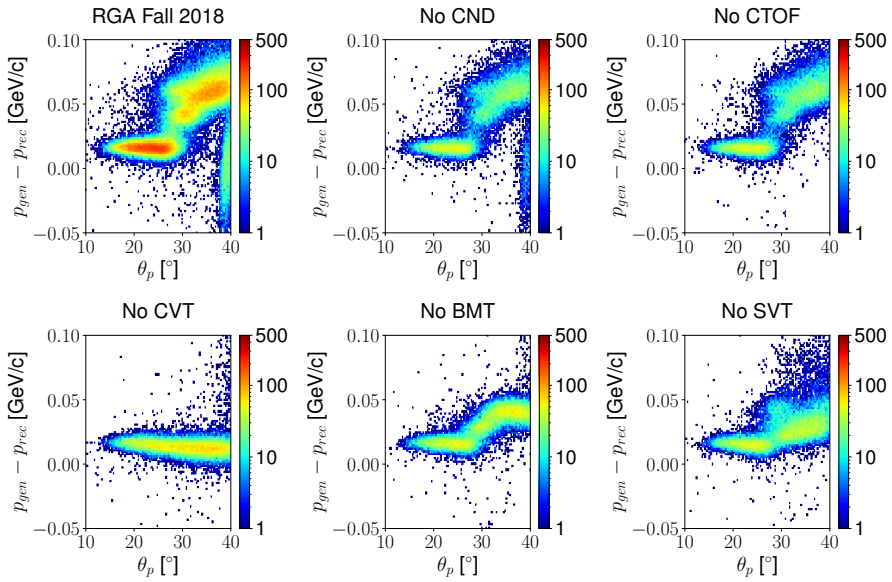

Figure 4-10: The distributions of reconstructed polar angle from the generated polar angle $\delta\theta$'s vs. the reconstructed momenta p's of the protons for inbending polarity for the various detector configurations (see each plot's title). The top left corner, which is the reproduced rga fall 2018 configuration as a reference has three broad regions. The flat band near the polar angle 20° and 0.02 GeV/c is the lower band of Fig. 4-7. Then, the upper band appears at around 0.05 GeV/c at higher polar angle. The vertical shape around 40° results from the protons reconstructed at the central detectors, which does not show when the CTOF or CVT is not present.

4.1.4 Proton Energy Loss Correction

The correction procedure consists of roughly three steps: (a) fitting the deviations for the data in a certain polar angle range with specific functions, (b) fitting the coefficients with regard to the polar angle, (c) applying corrections with the fitted coefficients for the quality assessment. The examples of (a), (b), and (c) are presented in Fig. 4-11 for the protons reconstructed in the lower band of the inbending polarity,

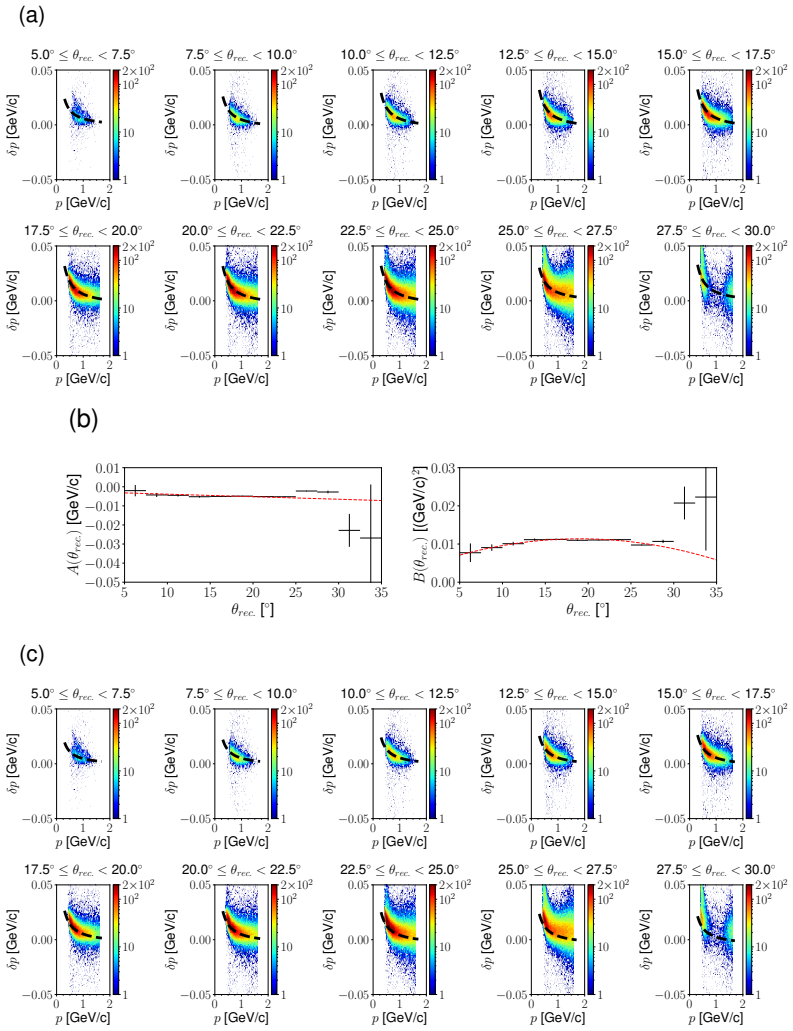

Figure 4-11: The procedures of correction: (a) fitting the proton momentum deviation of each polar angle range, (b) fitting the coefficients w.r.t. the polar angle, and (c) applying the coefficients fitted in the step (b).

forward detector. The functional forms of correction models are as follows.

$$p_{\text{new}} = p + A_p + B_p/p \tag{4.2}$$

$$\theta_{\text{new}} = \begin{cases} \theta + A_\theta + B_\theta \times \exp(C_\theta p) \\ \theta + D_\theta + E_\theta/p^2 \end{cases} \tag{4.3}$$

$$\phi_{\text{new}} = \begin{cases} \phi + A_\phi + B_\phi \times \exp(C_\phi p) \\ \phi + D_\phi + E_\phi/p^2. \end{cases} \tag{4.4}$$

The momentum variables with the subscript 'new' are the result of the energy loss corrections. Note that the polar angle and azimuthal angle can have different functions in some cases. The distinctive symbols are used to differentiate the function forms. i.e., if D_ϕ, E_ϕ are used, eqn. 4.4 is used. The rest of this subsection lays out each coefficient as a function of (p, θ). The decimals are truncated for simplicity. Similar plots to the electron corrections in Section 4.1.1 are presented with correction results in dotted curves. Captions are simplified to improve readability.

1. The FD protons in the lower band were corrected with the following coefficients for the inbending polarity. The correction of momentum, polar angle, azimuthal angles can be found in Figs. 4-11-c, 4-12 and 4-15. The fitting results in Fig. 4-11-b were reproduced with the latest simulation data set that was analyzed in Chapter 5. The fitted results are slightly different from eqns. 4.5–4.6 that had been studied with the simulation data set. The existing fitting results introduced in this section were applied to the data sets used for the analysis since the differences were minor.

$$A_p = -5.19\times10^{-4} - 1.81\times10^{-4} \times \theta \tag{4.5}$$

$$B_p = 3.29\times10^{-3} + 5.74\times10^{-4} \times \theta - 1.41\times10^{-5} \times \theta^2 \tag{4.6}$$

$$D_\theta = -1.67\times10^{-1} + 6.98\times10^{-3}\times\theta \tag{4.7}$$

$$E_\theta = 2.34\times10^{-1} - 1.34\times10^{-2}\times\theta \tag{4.8}$$

$$D_\phi = 2.12\times10^{-1} - 1.15\times10^{-2}\times\theta \tag{4.9}$$

$$E_\phi = -8.94\times10^{-1} + 1.66\times10^{-1}\times\theta - 8.91\times10^{-3}\times\theta^2 + 1.65\times10^{-4}\times\theta^3. \tag{4.10}$$

2. The FD protons in the upper band were corrected with the following coefficients for the inbending polarity. The corresponding correction plots can be found in Figs. 4-14–4-16.

$$A_p = -3.03\times10^{-1} + 1.83\times10^{-2}\times\theta - 2.86\times10^{-4}\times\theta^2 \quad (4.11)$$

$$B_p = 2.01\times10^{-1} - 1.13\times10^{-2}\times\theta + 1.82\times10^{-4}\times\theta^2. \quad (4.12)$$

$$D_\theta = 2.04\times10 - 1.81\times\theta + 5.33\times10^{-2}\times\theta^2 - 5.23\times10^{-4}\times\theta^3 \quad (4.13)$$

$$E_\theta = 8.74 - 7.64\times10^{-1}\times\theta + 2.22\times10^{-2}\times\theta^2 - 2.16\times10^{-4}\times\theta^3 \quad (4.14)$$

$$A_\phi = 5.47\times10^{-1} - 4.90\times10^{-2}\times\theta + 1.11\times10^{-3}\times\theta^2 \quad (4.15)$$

$$B_\phi = -4.07\times10^{2} + 2.44\times10\times\theta - 3.36\times10^{-1}\times\theta^2 \quad (4.16)$$

$$C_\phi = 2.06\times10 - 1.43\times\theta + 2.01\times10^{-2}\times\theta^2. \quad (4.17)$$

3. The CD protons were corrected with the following coefficients for the inbending polarity. The corresponding correction plots can be found in Figs. 4-17–4-19.

$$A_p = 1.94 - 1.16\times10^{-1}\times\theta + 2.24\times10^{-3}\times\theta^2 - 1.41\times10^{-5}\times\theta^3 \quad (4.18)$$

$$B_p = -7.38\times10^{-1} + 4.43\times10^{-2}\times\theta - 8.51\times10^{-4}\times\theta^2 + 5.37\times10^{-6}\times\theta^3 \quad (4.19)$$

$$A_\theta = -1.10\times10^{2} + 8.87\times\theta - 0.27\times\theta^2 + 3.54\times10^{-3}\times\theta^3 - 1.75\times10^{-5}\times\theta^4 \quad (4.20)$$

$$B_\theta = 9.52\times10^{2} - 5.75\times10\times\theta + 1.15\times\theta^2 - 7.58\times10^{-3}\times\theta^3 \quad (4.21)$$

$$C_\theta = -2.00\times10^{2} + 1.19\times10\times\theta - 2.38\times10^{-1}\times\theta^2 + 1.55\times10^{-3}\times\theta^3 \quad (4.22)$$

$$A_\phi = 4.95 - 3.27\times10^{-1}\times\theta + 7.39\times10^{-3}\times\theta^2 - 6.84\times10^{-5}\times\theta^3 + 2.12\times10^{-7}\times\theta^4 \quad (4.23)$$

$$B_\phi = 1.72\times10^{5} - 1.37\times10^{4}\times\theta + 4.01\times10^{2}\times\theta^2 - 5.13\times\theta^3 + 2.42\times10^{-2}\times\theta^4 \quad (4.24)$$

$$C_\phi = 1.20\times10^{2} - 5.87\times\theta + 7.44\times10^{-2}\times\theta^2 - 2.43\times10^{-4}\times\theta^3. \quad (4.25)$$

4. The FD protons in the lower band were corrected with the following coefficients for the outbending polarity. The corresponding correction plots can be found in

Figs. 4-20–4-22.

$$A_p = 5.08\times10^{-2} - 4.70\times10^{-3}\times\theta + 1.08\times10^{-4}\times\theta^2 \quad (4.26)$$

$$B_p = -1.47\times10^{-2} + 1.58\times10^{-3}\times\theta - 3.19\times10^{-5}\times\theta^2 \quad (4.27)$$

$$D_\theta = -2.56\times10 + 3.30\times\theta - 1.43\times10^{-1}\times\theta^2 + 2.08\times10^{-3}\times\theta^3 \quad (4.28)$$

$$E_\theta = 9.13\times10 - 1.20\times10\times\theta + 5.28\times10^{-1}\times\theta^2 - 7.73\times10^{-3}\times\theta^3 \quad (4.29)$$

$$D_\phi = -2.05\times10 + 1.67\times\theta - 3.42\times10^{-2}\times\theta^2 \quad (4.30)$$

$$E_\phi = 3.50\times10 - 2.91\times\theta + 6.04\times10^{-2}\times\theta^2. \quad (4.31)$$

5. The FD protons in the upper band were corrected with the following coefficients for the outbending polarity. The corresponding correction plots can be found in Figs. 4-23–4-25.

$$A_p = 9.83\times10^{-2} - 6.65\times10^{-3}\times\theta + 1.03\times10^{-4}\times\theta^2 \quad (4.32)$$

$$B_p = -9.61\times10^{-2} + 6.86\times10^{-3}\times\theta - 9.76\times10^{-5}\times\theta^2 \quad (4.33)$$

$$D_\theta = -1.69 + 9.57\times10^{-2}\times\theta - 1.44\times10^{-3}\times\theta^2 \quad (4.34)$$

$$E_\theta = 1.50\times10 - 1.40\times\theta + 4.39\times10^{-2}\times\theta^2 - 4.58\times10^{-4}\times\theta^3 \quad (4.35)$$

$$D_\phi = 6.75 - 4.3\times10^{-1}\times\theta + 6.90\times10^{-3}\times\theta^2 \quad (4.36)$$

$$E_\phi = -1.69 + 1.06\times10^{-1}\times\theta - 1.50\times10^{-3}\times\theta^2. \quad (4.37)$$

6. The CD protons were corrected with the following coefficients for the outbending polarity. The corresponding correction plots can be found in Figs. 4-26–4-28.

$$A_p = 1.93 - 1.14\times10^{-1}\times\theta + 2.15\times10^{-3}\times\theta^2 - 1.33\times10^{-5}\times\theta^3 \tag{4.38}$$

$$B_p = -7.56\times10^{-1} + 4.46\times10^{-2}\times\theta - 8.38\times10^{-4}\times\theta\times\theta + 5.17\times10^{-6}\times\theta^3 \tag{4.39}$$

$$A_\theta = -5.79\times10 + 4.67\times\theta - 0.14\times\theta^2 + 1.86\times10^{-3}\times\theta^3 - 9.20\times10^{-6}\times\theta^4 \tag{4.40}$$

$$B_\theta = 3.00\times10^3 - 2.18\times10^2\times\theta + 5.85\times\theta^2 - 6.80\times10^{-2}\times\theta^3 + 2.89\times10^{-4}\times\theta^4 \tag{4.41}$$

$$C_\theta = -1.82\times10^2 + 1.10\times10\times\theta - 2.25\times10^{-1}\times\theta^2 + 1.49\times10^{-3}\times\theta^3 \tag{4.42}$$

$$A_\phi = 7.59 - 5.28\times10^{-1}\times\theta + 1.32\times10^{-2}\times\theta^2 - 1.42\times10^{-4}\times\theta^3 + 5.63\times10^{-7}\times\theta^4 \tag{4.43}$$

$$B_\phi = 1.08\times10^5 - 8.68\times10^3\times\theta + 2.57\times10^2\times\theta^2 - 3.31\times\theta^3 + 1.57\times10^{-2}\times\theta^4 \tag{4.44}$$

$$C_\phi = 1.92\times10^2 - 1.01\times10\times\theta + 1.57\times10^{-1}\times\theta^2 - 7.71\times10^{-4}\times\theta^3 \tag{4.45}$$

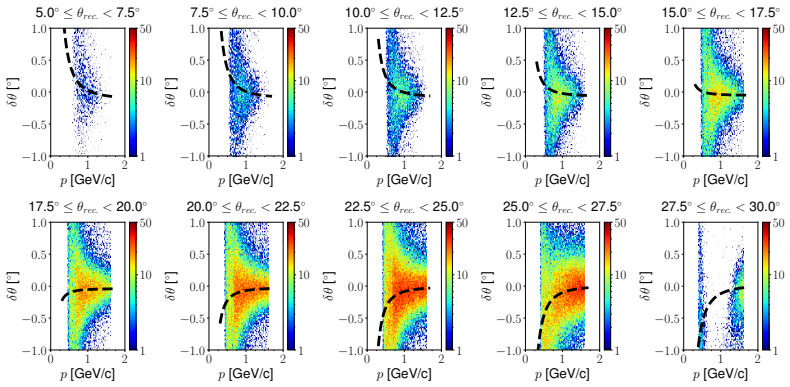

Figure 4-12: The $\delta\theta$ vs. p's of protons for the inbending polarity, lower band of FD, in the selected polar angle ranges described in each title.

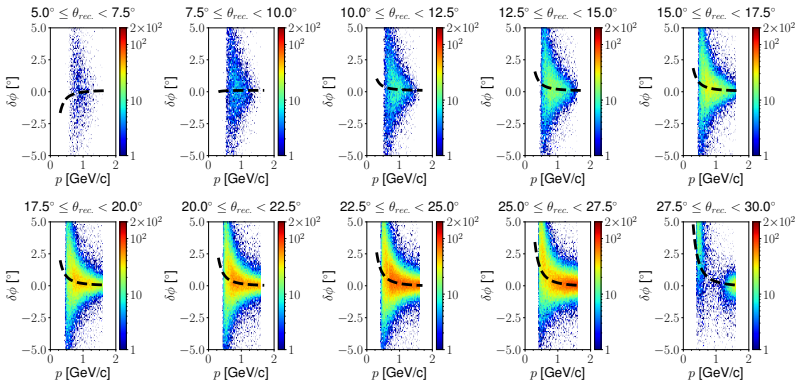

Figure 4-13: The $\delta\phi$ vs. p of protons for the inbending polarity, lower band of FD, in the selected polar angle ranges described in each title.

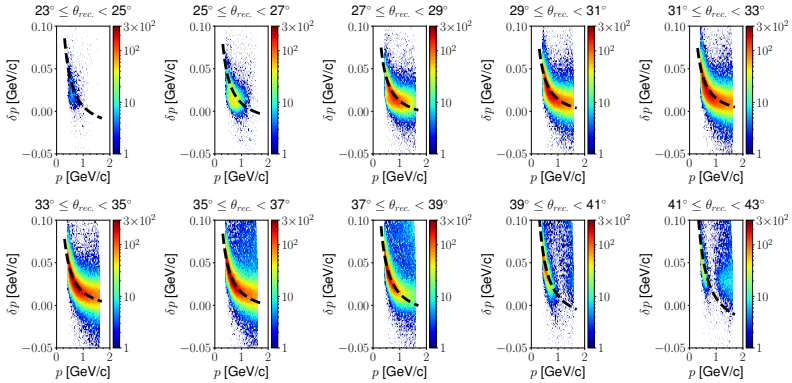

Figure 4-14: The δp vs. p of protons for the inbending polarity, upper band of FD, in the selected polar angle ranges described in each title.

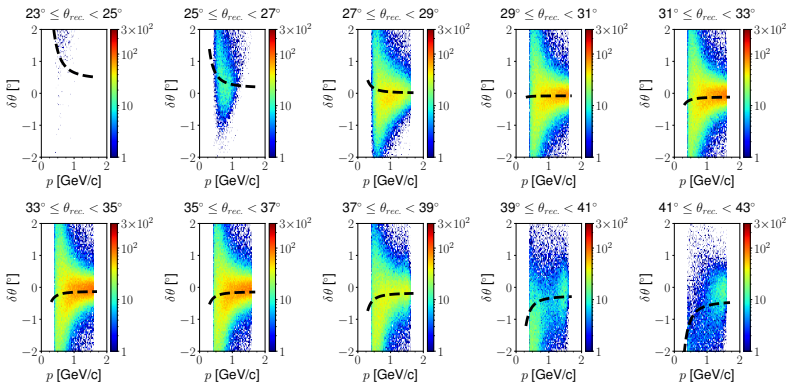

Figure 4-15: The $\delta\theta$ vs. p of protons for the inbending polarity, upper band of FD, in the selected polar angle ranges described in each title.

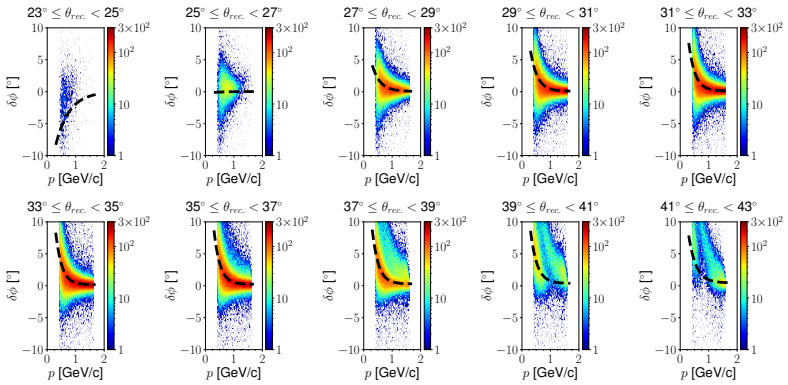

Figure 4-16: The $\delta\phi$ vs. p's of protons for the inbending polarity, upper band of FD in the selected polar angle ranges described in each title.

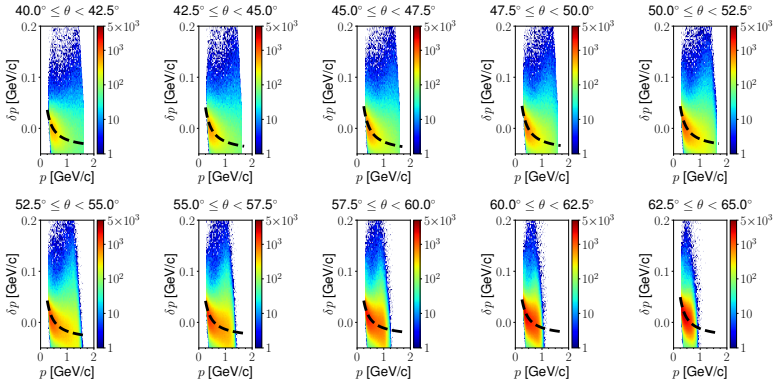

Figure 4-17: The δp vs. p of protons for the inbending polarity, CD, in the selected polar angle ranges described in each title.

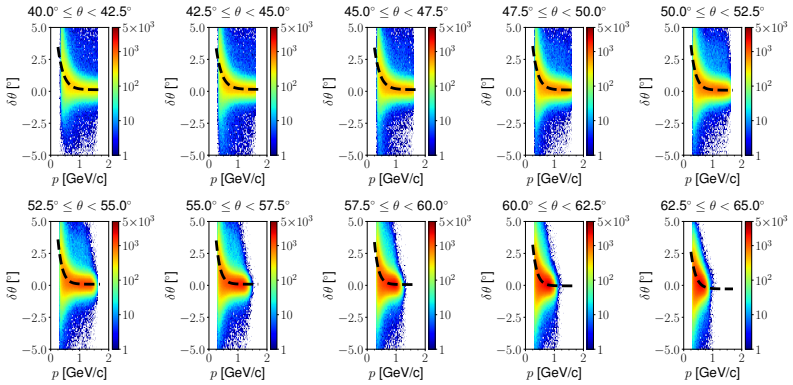

Figure 4-18: The $\delta\theta$ vs. p of protons for the inbending polarity, CD, in the selected polar angle ranges described in each title.

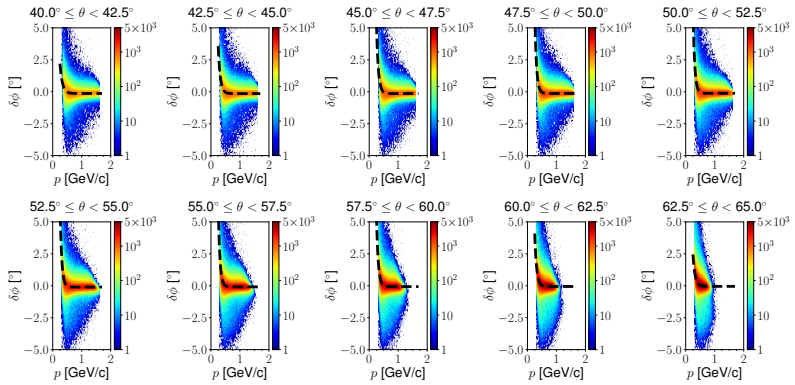

Figure 4-19: The $\delta\phi$ vs. p's of protons for the inbending polarity, CD in the selected polar angle ranges described in each title.

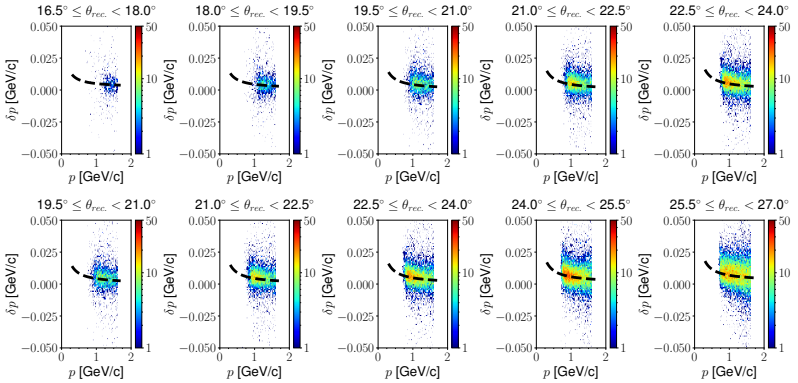

Figure 4-20: The δp vs. p's of protons for the outbending polarity, lower band of FD, in the selected polar angle ranges described in each title.

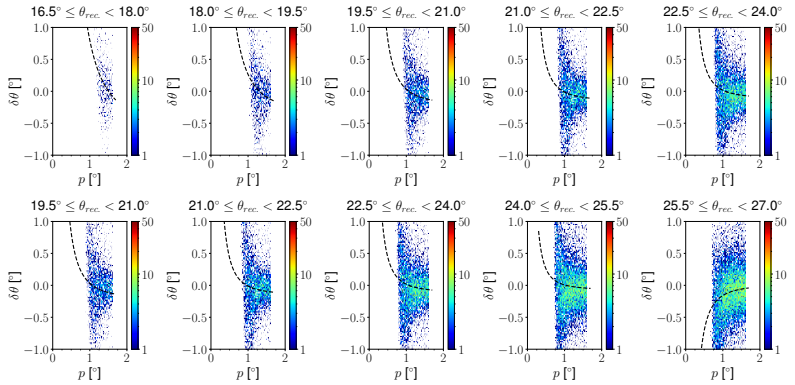

Figure 4-21: The $\delta\theta$ vs. p's of protons for the outbending polarity, lower band of FD, in the selected polar angle ranges described in each title.

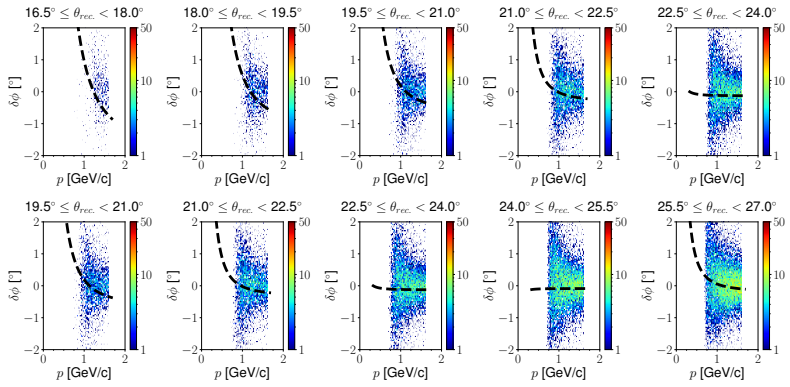

Figure 4-22: The $\delta\phi$ vs. p's of protons for the outbending polarity, lower band of FD, in the selected polar angle ranges described in each title.

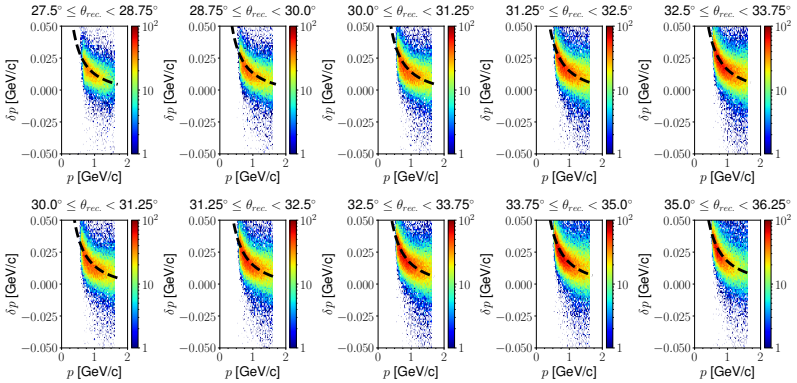

Figure 4-23: The δp vs. p's of protons for the outbending polarity, upper band of FD, in the selected polar angle ranges described in each title.

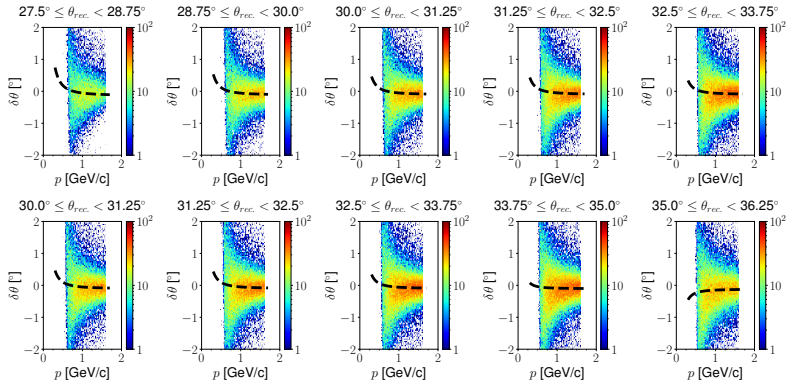

Figure 4-24: The $\delta\theta$ vs. p's of protons for the outbending polarity, upper band of FD, in the selected polar angle ranges described in each title.

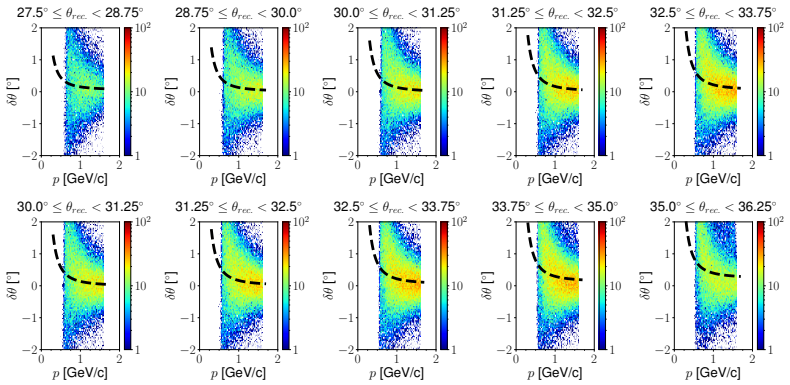

Figure 4-25: The $\delta\phi$ vs. p's of protons for the outbending polarity, upper band of FD, in the selected polar angle ranges described in each title.

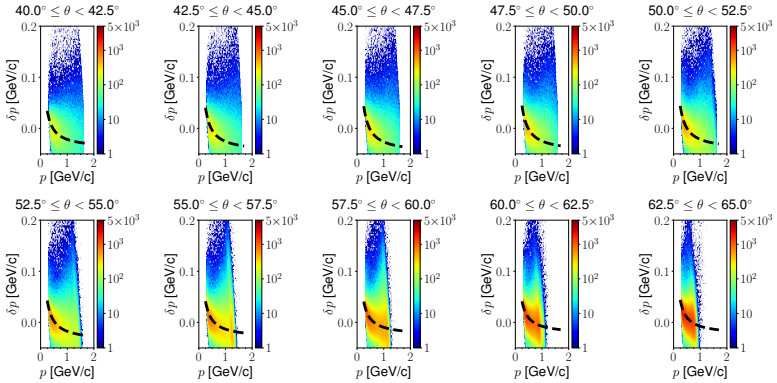

Figure 4-26: The δp vs. p of protons for the outbending polarity, CD, in the selected polar angle ranges described in each title.

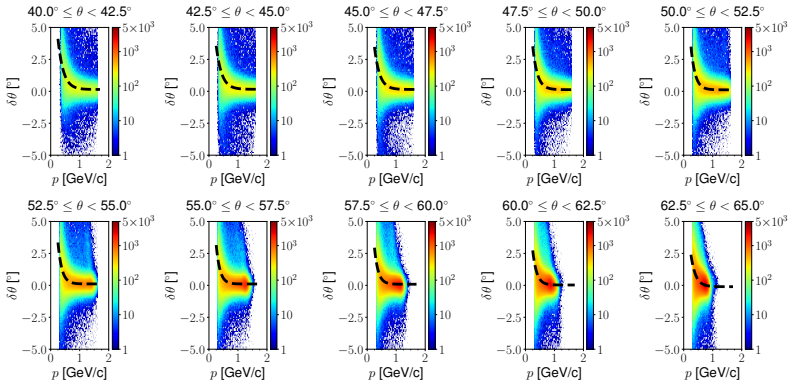

Figure 4-27: The $\delta\theta$ vs. p of protons for the outbending polarity, CD, in the selected polar angle ranges described in each title.

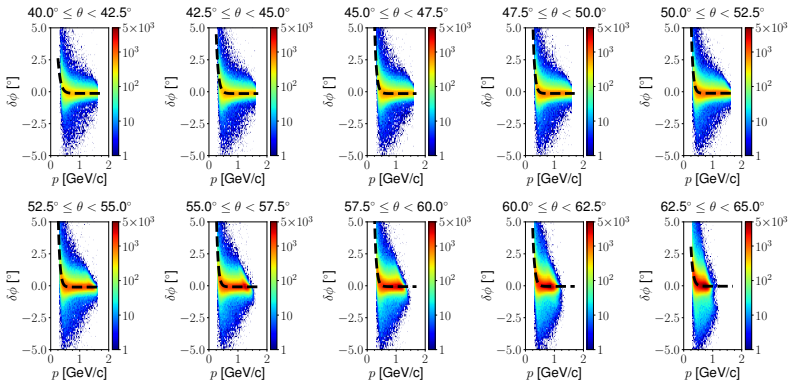

Figure 4-28: The $\delta\phi$ vs. p's of protons for the outbending polarity, CD in the selected polar angle ranges described in each title.

4.1.5 Biases for Higher Momentum Protons

The proton energy loss corrections in this chapter were developed for the BH-DVCS events that are dominated by low momentum protons of $p < 1$ GeV/c. Another set of corrections was developed independently, for the FD protons [185]. The correction is as follows:

$$p_{\text{new}} = p + \exp(A - B \times p) + C \ , \tag{4.46}$$

with (A, B, C) = (-2.739, -3.932, 2.907×10^{-3}), (-1.2, -4.228, 7.502×10^{-3}), (-2.739, -3.932, 2.907×10^{-3}), (-1.871, -3.063, 7.517×10^{-3}) for the inbending lower band, inbending upper band, outbending lower band, and inbending upper band, respectively. Even though this correction was developed for all proton momenta, we selectively take this correction for $p > 1$ GeV/c. In conclusion, we use eqn. 4.2 for FD protons with $p > 1$ GeV/c.

4.1.6 Benchmarks for corrections

The benchmark plots after the corrections have been applied are shown in Fig. 4-29. Each plot shows that the correction both improves the central position and reduces the widths of the distributions of $MM^2_{e'p'}$, δp, $\delta\theta$ and $\delta\phi$.

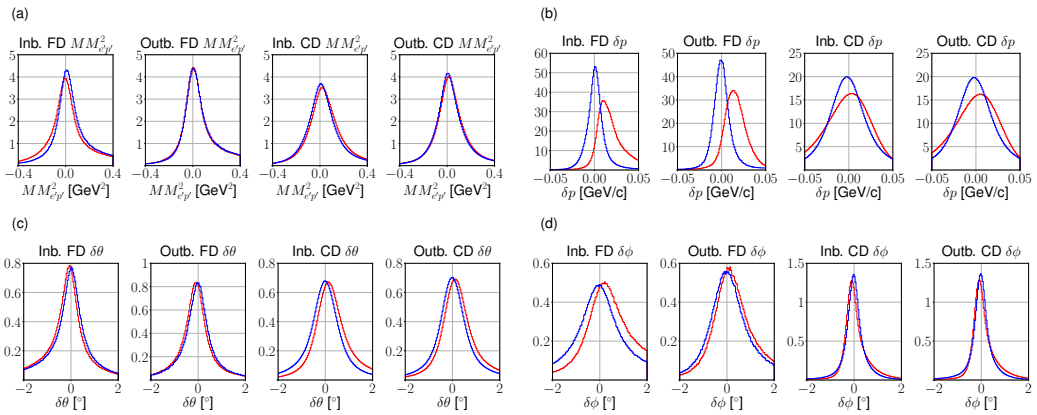

Figure 4-29: Benchmark plots of (a) exclusivity variables $MM^2_{e'p'}$ (4 plots of top left), (b) momentum (δp) (4 plots of top right), (c) polar angle ($\delta\theta$) (4 plots of bottom left), and (d) azimuthal angle ($\delta\phi$) (4 plots of bottom right). The red and blue curves show the variables before and after the corrections respectively.

4.2 Resolution Matching

The detector responses in the GEMC simulation are designed to reflect the nominal resolutions, rather conservatively. If the distributions of kinematic variables in the simulation were wider than the experimental data in some part of phase space, it would be difficult to deconvolute the smearing effect. As the CLAS12 experiment is in its early stage, work is underway to reduce the reconstruction bias and to improve the detector resolution matching. In this analysis, we use the post-processing of the reconstructed data by smearing the reconstructed momentum variables using the gaussian kernels, and correct the experimental momentum variables with simple models.

This section describes three categories: kinematic correction of experimental data, smearing of simulation data and final level event selection. The three steps are convoluted; they were updated concurrently and iteratively.

4.2.1 Kinematics Correction of Experimental Data

We performed the correction of the kinematics of p' and γ as follows and assumed the proton energy loss correction was already applied. In this section $\tilde{p}_{p'}$, $\tilde{\theta}_{p'}$, $\tilde{p}_{\gamma}$, $\tilde{\theta}_{\gamma}$

denotes the corrected momentum.

$$\tilde{p}_{p'} = p_{p'} + \begin{cases} 0.01 & \text{(CD)} \\ 0 & \text{(FD, Inb.)} \\ -0.02 & \text{(FD, Outb.)} \end{cases} \tag{4.47}$$

$$\tilde{\theta}_{p'} = \theta_{p'} + \begin{cases} -2.13\times10^{-3}\theta_{p'}^2 + 1.98\times10^{-1}\theta_{p'} - 4.76 - \frac{0.2}{(1+\exp(-20(\tilde{p}_{p'}-0.55))} & \text{(CD)} \\ \min(1.671p_{p'}^3 - 4.918p_{p'}^2 + 5.151p_{p'} - 2.434, 0) & \text{(FD, Inb.)} \\ \max(0.1(\theta_{p'} - 27^\circ), 0) & \text{(FD, Outb.)} \end{cases} \tag{4.48}$$

$$\tilde{p}_{\gamma} = p_{\gamma} + \begin{cases} (-4.67 \times 10^{-3}p_{\gamma}^2 + 8.02 \times 10^{-2}p_{\gamma} - 0.352) + 0.25 & \text{(FT, Outb.)} \\ f(p_{\gamma}, s) & \text{(FD, Inb.)} \\ g(p_{\gamma}, s) & \text{(FD, Outb.)}, \end{cases} \tag{4.49}$$

where the functions $f(p_\gamma, s)$ and $g(p_\gamma, s)$ are defined as follows.

$$f(p_\gamma, s) = f_1(f_2(p_\gamma, (a_{2,s}, a_{1,s}, a_{0,s}]), [b_{2,s}, b_{1,s}, b_{0,s}]) \tag{4.50}$$

$$g(p_\gamma, s) = g_1(p_\gamma, [c_{2,s}, c_{1,s}, c_{0,s}])r(p_\gamma) \tag{4.51}$$

$$f_2(x, [a_{2,s}, a_{1,s}, a_{0,s}]) = \begin{cases} a_{2,s}p_\gamma(p_\gamma - a_{1,s})^3(p_\gamma - a_{0,s}) & (s = 1, 2, 3, 6) \\ a_{2,s}p_\gamma^3 + a_{1,s}p_\gamma^2 + a_{0,s}p_\gamma & (s = 4, 5) \end{cases} \tag{4.52}$$

$$f_1(x, [b_{2,s}, b_{1,s}, b_{0,s}]) = \begin{cases} b_{2,s}p_\gamma(p_\gamma - b_{1,s})^3(p_\gamma - b_{0,s}) & (s = 1, 2, 3) \\ b_{2,s}p_\gamma^3 + b_{1,s}p_\gamma^2 + b_{0,s}p_\gamma & (s = 4, 5, 6) \end{cases} \tag{4.53}$$

$$g_1(x, [c_{3,s}, c_{2,s}, c_{1,s}, c_{0,s}]) = c_{3,s}p_\gamma^3 + c_{2,s}p_\gamma^2 + c_{1,s}p_\gamma + c_{0,s} \tag{4.54}$$

$$r(p_\gamma) = 1/(1 + e^{-(p_\gamma - 2.2)/0.15}) \ , \tag{4.55}$$

with the fitting parameters $[a_{2,s}, a_{1,s}, a_{0,s}]$, $[b_{2,s}, b_{1,s}, b_{0,s}]$, and $[c_{3,s}, c_{2,s}, c_{1,s}, c_{0,s}]$ that are sorted at Table 4.1.

Table 4.1: Fitting parameters a, b and c for each sectors that were used for kinematics correction.

	Sector 1	Sector 2	Sector 3	Sector 4	Sector 5	Sector 6
$a_{2,s}$	-7.32×10^{-5}	1.35×10^{-4}	-4.37×10^{-5}	-4.28×10^{-5}	2.50×10^{-4}	-4.54×10^{-5}
$a_{1,s}$	1.480	3.070	7.19×10^{-1}	2.34×10^{-3}	-3.14×10^{-3}	5.17×10^{-1}
$a_{0,s}$	9.344	9.248	9.873	1.03×10^{-2}	2.32×10^{-2}	9.447
$b_{2,s}$	-1.68×10^{-5}	-3.40×10^{-5}	-6.20×10^{-5}	1.32×10^{-4}	-1.35×10^{-4}	2.63×10^{-4}
$b_{1,s}$	8.21×10^{-1}	2.720	2.793	-1.62×10^{-3}	2.82×10^{-4}	-2.93×10^{-3}
$b_{0,s}$	8.894	8.419	8.865	9.78×10^{-3}	6.50×10^{-3}	1.39×10^{-2}
$c_{3,s}$	-6.15×10^{-4}	-3.34×10^{-4}	-9.11×10^{-4}	1.17×10^{-4}	-1.19×10^{-4}	-8.93×10^{-4}
$c_{2,s}$	1.13×10^{-2}	6.56×10^{-3}	1.57×10^{-2}	-9.05×10^{-4}	9.79×10^{-4}	1.31×10^{-2}
$c_{1,s}$	-6.00×10^{-2}	-3.83×10^{-2}	-8.06×10^{-2}	2.15×10^{-3}	-4.00×10^{-3}	-5.80×10^{-2}
$c_{0,s}$	1.15×10^{-1}	9.34×10^{-2}	1.54×10^{-1}	3.31×10^{-2}	4.99×10^{-2}	1.11×10^{-1}

4.2.2 Smearing the Simulation Data

As discussed earlier in this chapter, it is best to have the simulation data set with reconstructed particles, whose resolutions are the same as the experimental data set. Failure in doing so propagates to the exclusivity variables mismatches and disturbs the precise cross section analysis. It is ideal to adjust the lowest level detector properties to achieve resolution matching. This is a complex task for a large detector like CLAS12 and is a work in progress. Instead, the smearing procedure was applied to the reconstructed momentum variables to compensate for overestimated reconstruction quality, effectively. The multiplicative and additive models were applied to momentum magnitude variables and angular variables respectively. The smearing scales were regulated by sigmoid functions, denoted by R if needed to prevent excessive smearing near the threshold.

$$\tilde{p}_{p'} = p_{p'} \times Gauss(1, \sigma_{p_{p'}} \times R_{p_{p'}}) \tag{4.56}$$

$$\tilde{\theta}_{p'} = \theta_{p'} + Gauss(0, \sigma_{\theta_{p'}}) \tag{4.57}$$

$$\tilde{\phi}_{p'} = \phi_{p'} + Gauss(0, \sigma_{0,\ \phi_{p'}} + \sigma_{1,\ \phi_{p'}} \times R_{\phi_{p'}}) \tag{4.58}$$

$$\tilde{p}_{\gamma} = p_{\gamma} \times Gauss(1, \sigma_{0,p_{\gamma}} + \sigma_{1,p_{\gamma}} \times R_{p_{\gamma}}) \tag{4.59}$$

The momentum smearing parameters of CD protons are as follows.

$$\sigma_{p_{p'}} = \begin{cases} 9.26\times10^{-2}p_{p'}^3 + 1.37\times10^{-1}p_{p'}^2 - 2.30\times10^{-1}p_{p'} + 1.39\times10^{-1} & (p_{p'} < 0.85) \\ 0.1 & (p_{p'} \geq 0.85) \end{cases} \tag{4.60}$$

The FD proton momentum smearing parameters in eqn. 4.56 are expressed as the following functional form for the inbending polarity.

$$\sigma_{p_{p'}} = \begin{cases} A_{4,s}p_{p'}^4 + A_{3,s}p_{p'}^3 + A_{2,s}p_{p'}^2 + A_{1,s}p_{p'} + A_{0,s} & (0.55 < p_{p'} \leq 1.55) \\ A_{4,s}0.55^4 + A_{3,s}0.55^3 + A_{2,s}0.55^2 + A_{1,s}0.55 + A_{0,s} & (p_{p'} < 0.55) \\ A_{4,s}1.55^4 + A_{3,s}1.55^3 + A_{2,s}1.55^2 + A_{1,s}1.55 + A_{0,s} & (p_{p'} \geq 1.55), \end{cases} \tag{4.61}$$

where each coefficient $A_{i,s}$'s can be found in Table 4.2.

Table 4.2: Smearing parameters $A_{4,s}$, $A_{3,s}$, $A_{2,s}$, $A_{1,s}$ and $A_{0,s}$ for each sectors.

	Sector 1	Sector 2	Sector 3	Sector 4	Sector 5	Sector 6
$A_{4,s}$	-0.233	0.277	0.0728	-0.204	0.277	-0.219
$A_{3,s}$	1.216	-1.366	-0.223	0.977	-1.059	1.132
$A_{2,s}$	-2.279	2.318	0.0888	-1.766	1.362	-2.153
$A_{1,s}$	1.812	-1.619	0.225	1.411	-0.641	1.763
$A_{0,s}$	-0.445	0.466	-0.0889	-0.342	0.1377	-0.447

The FD proton momentum smearing parameters in eqn. 4.56 for the outbending polarity are as follows.

$$\sigma_{p_{p'}} = \begin{cases} 0.1 & (p_{p'} < 0.95) \\ 0.045(1.2 - x)/(1.2 - 0.95) + 0.055 & (0.95 \leq p_{p'} < 1.2) \\ 0.055 & (1.2 \leq p_{p'} < 1.575) \\ 0.015(1.9 - x)/(1.9 - 1.575) + 0.04 & (1.575 \leq p_{p'} < 1.9) \\ 0.04 & (p_{p'} \geq 1.9). \end{cases} \tag{4.62}$$

The CD proton angular variables were smeared with the following factors and additive model (eqns. 4.57 and 4.58).

$$\sigma_{\theta_{p'}} = \begin{cases} -2.797p_{p'}^3 + 9.351p_{p'}^2 - 9.488p_{p'} + 3.503 & (p_{p'} < 1.34 \text{ GeV/c}) \\ 0.85 & (p_{p'} \geq 1.34 \text{ GeV/c}) \end{cases} \tag{4.63}$$

$$\sigma_{0,\phi_{p'}} = 0.8 \tag{4.64}$$

$$\sigma_{1,\phi_{p'}} = 2.2, \tag{4.65}$$

whereas the FD angular variables were not smeared out. The photon momentum variables were smeared with multiplicative model (eqn. 4.59) as follows.

$$\sigma_{0,p_\gamma} = \begin{cases} 0.013 & \text{(FT)} \\ 0 & \text{(FD)} \end{cases} \qquad \sigma_{1,p_\gamma} = \begin{cases} 0.003 & \text{(FT)} \\ 0.0395 & \text{(FD).} \end{cases} \tag{4.66}$$

Finally, the regulators applied to the smearing factors (eqns. 4.56, 4.58 and 4.59) are paramterized as follows.

$$R_{p_{p'}} = \begin{cases} 2(1/(1+\exp(-(p_{p'}-0.3)/0.01)) - 0.5) & \text{(CD)} \\ 1/(1+\exp(-(p_{p'}-0.5)/0.05)) & \text{(FD, Inb.)} \\ 1/(1+\exp(-(p_{p'}-0.6)/0.05)) & \text{(FD, Outb.)} \end{cases} \tag{4.67}$$

$$R_{\phi_{p'}} = \begin{cases} 1/(1+\exp(5.518(p_{p'}-0.625))) & \text{(CD)} \\ 0 & \text{(FD)} \end{cases} \tag{4.68}$$

$$R_{p_\gamma} = \begin{cases} 1/(1+\exp(0.761(p_\gamma - 6))) & \text{(FT)} \\ 1/(1+\exp(5.308(p_\gamma - 8.005))) & \text{(FD).} \end{cases} \tag{4.69}$$

Chapter 5

Results

5.1 CLAS12 Quality Assurance

To minimize large systematic effects from data with quality issues, Quality Assurance (QA) was performed in this analysis. The CLAS12 QA has been developed for the RG-A data, and the database is saved in the dedicated github repository [186]. A run is a time unit of data taking that shares the same detector setting such as the trigger configuration and the requested beam current. A typical run approximately records 100M triggered events and is taken in about 4 hours. The run properties are accessible from the run condition dataBase (RCDB[1]). The inbending data set consists of 174 runs from 5032–5419, and the outbending data set consists of 186 runs from 5422–5666. The initial run period 5422–5476 for the outbending data set has a slightly larger toroid current +1.00796 that had a marginal effect on the data analysis.

The number of exclusive events $ep \to e'p'\gamma$ that were defined with the exclusivity cuts ($N(e'p'\gamma)^{e'p'\gamma}_{\text{exp.}}$) was normalized to the QA passed beam charge (Q) as an additional quality check for each run. The number of events per charge is stable for the data that passed the 'golden cut' of the QA (Fig. 5-1). The run ranges are charaterized by beam currents delivered to the beamline; the 45, 50, 55 nA for inbending and 40, 50 nA for outbending.

[1] https://clasweb.jlab.org/rcdb/runs/5032-5666

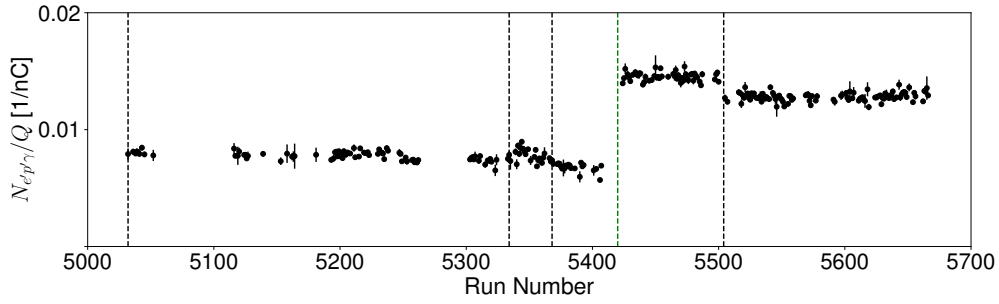

Figure 5-1: The number of exclusivity events $N(e'p'\gamma)^{e'p'\gamma}_{\text{exp.}}$ normalized to beam charge in nC. The dotted lines roughly separates the run ranges with different beam currents. Especially, the green dotted line is the border between the inbending and outbending run periods.

5.2 Event Selection Revisited

The 3σ window for exclusivity variables for DVπ^0P events can be determined without considering the background channel thanks to the very strong experimental trace, IM_{π^0}. The exclusivity variables were fitted for each polarity and event topology. The π^0 photon energy threshold is constrained to reduce the random coincidence rate between the prevalent radiative photons and fake neutral signals; but this limit need not be as high as the 2 GeV for DVCS events. The threshold in the DVπ^0P wagon is 150 MeV. From the 2D histogram of IM_{π^0} vs p_{γ_2}, we decided to increase this threshold to 400 MeV.

Finally, the 3σ ranges of exclusivity variables are set for each detector configuration. For the DVCS events, the variable cuts are defined by a set of upper bounds ub and lower bounds lb as follows:

- $lb_{MM^2_{e'p'}} \leq MM^2_{e'p'} < ub_{MM^2_{e'p'}}$
- $lb_{MM^2_{e'\gamma}} \leq MM^2_{e'\gamma} < ub_{MM^2_{e'\gamma}}$
- $lb_{MM^2_{e'p'\gamma}} \leq MM^2_{e'p'\gamma} < ub_{MM^2_{e'p'\gamma}}$
- $lb_{ME_{e'p'\gamma}} \leq ME_{e'p'\gamma} < ub_{ME_{e'p'\gamma}}$
- $lb_{MPt_{e'p'\gamma}} \leq MPt_{e'p'\gamma} < ub_{MPt_{e'p'\gamma}}$
- $\theta_{\gamma_{det.}\gamma_{rec.}} < ub_{\theta_{\gamma_{det.}\gamma_{rec.}}}$

- $\phi_{H\Gamma} < ub_{\phi_{H\Gamma}}$
- $a_2\theta_{e'}^2 + a_1\theta_{e'} + a_0 \leq \theta_{e'\gamma} < b_2\theta_{e'}^2 + b_1\theta_{e'} + b_0$.

The unit of variables are GeV^2 for $MM^2_{e'p'}$, $MM^2_{e'\gamma}$, $MM^2_{e'p'\gamma}$, GeV for $ME_{e'p'\gamma}$, GeV/c for $MPt_{e'p'\gamma}$ and $^\circ$ for angular variables $\theta_{\gamma_{det.}\gamma_{rec.}}$, $\phi_{H\Gamma}$, $\theta_{e'\gamma}$ and $\theta_{e'}$. The lower and upper bounds are summarized in Table 5.1.

Likewise, the DVπ^0P event selection is also refined with the following cuts on the exclusivity variables:

- $lb_{IM_{\pi^0}} < IM_{\pi^0} < ub_{IM_{\pi^0}}$
- $lb_{MM^2_{e'p'}} < MM^2_{e'p'} < ub_{MM^2_{e'p'}}$
- $lb_{MM^2_{e'\pi^0}} < MM^2_{e'\pi^0} < ub_{MM^2_{e'\pi^0}}$
- $lb_{MM^2_{e'p'\pi^0}} < MM^2_{e'p'\pi^0} < ub_{MM^2_{e'p'\pi^0}}$
- $lb_{ME_{e'p'\pi^0}} < ME_{e'p'\pi^0} < ub_{ME_{e'p'\pi^0}}$
- $lb_{MPt_{e'p'\pi^0}} < MPt_{e'p'\pi^0} < ub_{MPt_{e'p'\pi^0}}$
- $\theta_{\pi^0_{det.}\pi^0_{rec.}} < ub_{\theta_{\pi^0_{det.}\pi^0_{rec.}}}$
- $\phi_{H\Pi} < ub_{\phi_{H\Pi}}$.

Similarly, the units are GeV^2 for $MM^2_{e'p'}$, $MM^2_{e'\pi^0}$, $MM^2_{e'p'\pi^0}$, GeV for IM_{π^0} and $ME_{e'p'\pi^0}$, GeV/c for $MPt_{e'p'\pi^0}$ and $^\circ$ for angular variables $\theta_{\pi^0_{det.}\pi^0_{rec.}}$, $\phi_{H\Pi}$, $\theta_{e'\pi^0}$ and $\theta_{e'}$. The lower and upper bounds are summarized in Table 5.1.

The distributions of the exclusivity variables are presented at Figs. 5-2–5-13 with red curves for the experimental distributions and the blue curves for the simulation distributions. For the BH-DVCS candidates that contain copious DVπ^0P backgrounds, the simulation distribution is a mixture of two distributions, the DVCS and the DVπ^0P misidentified events with a reasonable estimation of the π^0 contamination.

The $ep \to e'p'\gamma$ and $ep \to e'p'\gamma\gamma$ exclusive sets are defined as sets of individual particles that satisfy 3σ cuts on exclusivity variables in Tables 5.1 and 5.2 respectively. The $ep \to e'p'\gamma$ or $ep \to e'p'\gamma\gamma$ exclusive events are accordingly defined as one that possess at least one $ep \to e'p'\gamma$ or $ep \to e'p'\gamma\gamma$ exclusive event. There is a

Table 5.1: The lower and upper bounds for the $ep \to e'p'\gamma$ event selection within 3σ window. The 3σ curves of $\theta_{e'\gamma} - \theta_{e'}$ are identical for the inbending and outbending BH-DVCS selection. The lower $\theta_{e'\gamma}$ regions in (CD, FT) configuration were included as discussed in Section 3.3, and presented in this table at the bottom row of (CD, FT) columns.

	Inb. (FD, FD)	Inb. (CD, FD)	Inb. (CD, FT)	Outb. (FD, FD)	Outb. (CD, FD)	Outb. (CD, FT)
$lb_{MM^2_{e'p'}}$	-0.144	-0.272	-0.365	-0.174	0.226	-0.244
$ub_{MM^2_{e'p'}}$	0.190	0.294	0.391	0.225	-0.196	0.321
$lb_{MM^2_{e'\gamma}}$	0.0505	0.166	0.322	1.940	0.0356	0.418
$ub_{MM^2_{e'\gamma}}$	1.989	1.790	1.479	0.160	1.902	1.352
$lb_{MM^2_{e'p'\gamma}}$	-0.0177	-0.0161	-0.0108	-0.0202	-0.0163	-8.84×10^{-3}
$ub_{MM^2_{e'p'\gamma}}$	0.0142	0.0139	0.008	0.0162	0.0138	6.53×10^{-3}
$lb_{ME_{e'p'\gamma}}$	-0.740	-0.557	-0.387	-0.519	-0.631	-0.275
$ub_{ME_{e'p'\gamma}}$	0.976	0.672	0.360	0.772	0.755	0.299
$ub_{MPt_{e'p'\gamma}}$	0.291	0.0919	0.0844	0.340	0.147	0.0627
$ub_{\theta_{\gamma_{det.}\gamma_{rec.}}}$	1.487	0.654	0.582	1.645	0.839	0.578
$ub_{\phi_{H\Gamma}}$	8.36	5.034	5.633	6.342	5.181	4.742
a_2	0.0214	0.0164	0.0267 0.051	0.0214	0.0164	0.0267 0.051
a_1	-0.379	0.408	-0.0625 -0.047	-0.379	0.408	-0.0625 -0.047
a_0	21.998	4.901	7.73 -0.492	21.998	4.901	7.73 -0.492
b_2	0.028	0.047	-2.21×10^{-3} -3.82×10^{-4}	0.028	0.047	-2.21×10^{-3} -3.82×10^{-4}
b_1	-1.001	-1.677	0.863 0.777	-1.001	-1.677	0.863 0.777
b_0	49.895	46.014	10.287 0.867	49.895	46.014	10.287 0.867

Table 5.2: The lower and upper bounds for the DVπ^0P exclusivity variables within 3σ window.

	Inb. (FD, FD)	Inb. (CD, FD)	Inb. (CD, FT)	Outb. (FD, FD)	Outb. (CD, FD)	Outb. (CD, FT)
$lb_{IM_{\pi^0}}$	0.0910	0.107	0.126	0.105	0.106	0.124
$ub_{IM_{\pi^0}}$	0.178	0.162	0.149	0.164	0.163	0.151
$lb_{MM^2_{e'p'}}$	-0.271	-0.283	-0.384	-0.256	-0.218	-0.378
$ub_{MM^2_{e'p'}}$	0.335	0.354	0.610	0.323	0.294	0.575
$lb_{MM^2_{e'\pi}}$	0.117	0.007	0.0974	0.0491	-0.0142	0.107
$ub_{MM^2_{e'\pi}}$	1.762	1.922	1.641	1.828	1.876	1.665
$lb_{MM^2_{e'p'\pi}}$	-0.0224	-0.0250	-0.02944	-0.0240	-0.0219	-0.035
$ub_{MM^2_{e'p'\pi}}$	0.0189	0.0208	0.02564	0.0195	0.0182	0.0324
$lb_{ME_{e'p'\pi}}$	-0.685	-0.677	-0.474	-0.583	-0.597	-0.476
$ub_{ME_{e'p'\pi}}$	0.816	0.822	0.481	0.754	0.700	0.514
$ub_{MPt_{e'p'\pi}}$	0.180	0.176	0.1272	0.177	0.194	0.146
$ub_{\theta_{\pi^0_{det.}\pi^0_{rec.}}}$	1.363	1.476	0.955	1.940	1.761	1.114
$ub_{\phi_{H\Pi}}$	9.190	10.203	9.259	7.498	9.530	10.69

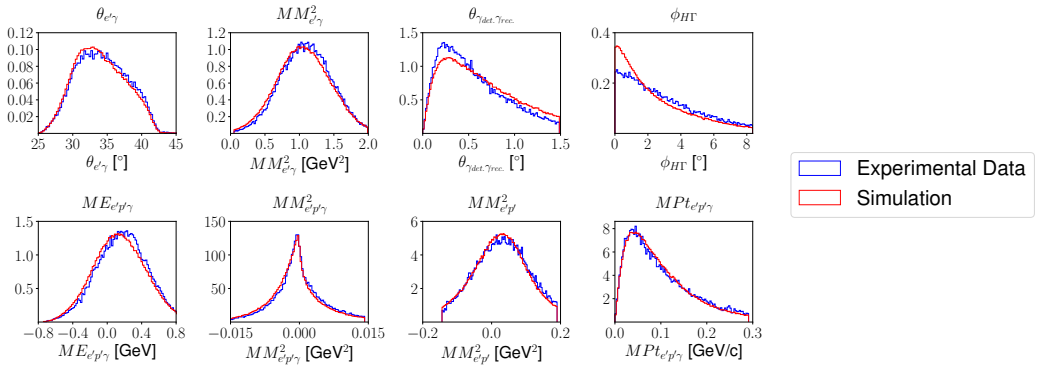

Figure 5-2: The kinematic and exclusivity variables of BH-DVCS candidates with (FD, FD) topology and inbending polarity configuration. The blue curves are the experimental distributions and the red curves are the simulation distributions.

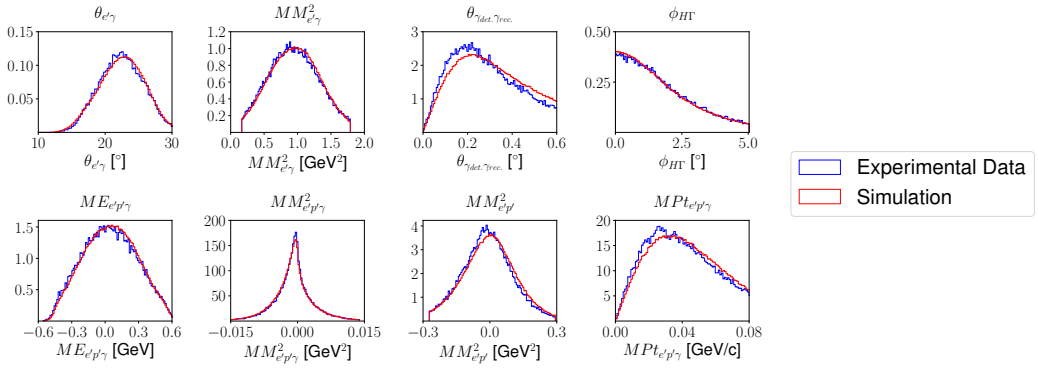

Figure 5-3: The kinematic and exclusivity variables of BH-DVCS candidates with (CD, FD) topology and inbending polarity configuration. The blue curves are the experimental distributions and the red curves are the simulation distributions.

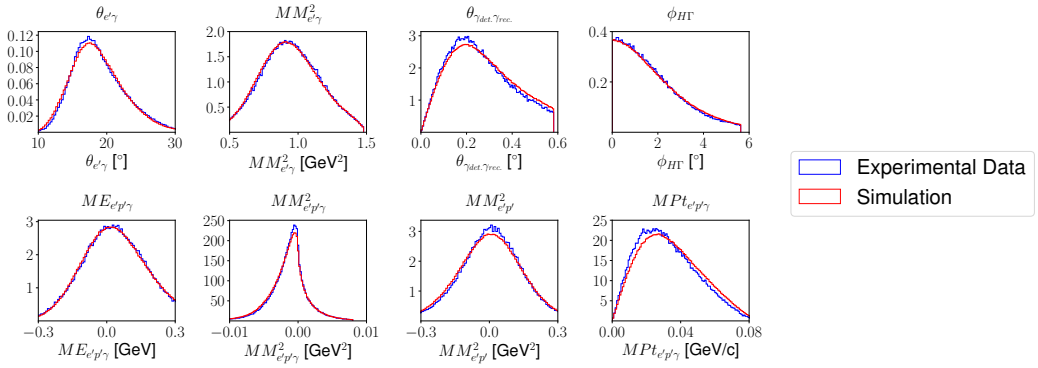

Figure 5-4: The kinematic and exclusivity variables for BH-DVCS candidates with (CD, FT) topology and inbending polarity configuration. The blue curves are the experimental distributions and the red curves are the simulation distributions.

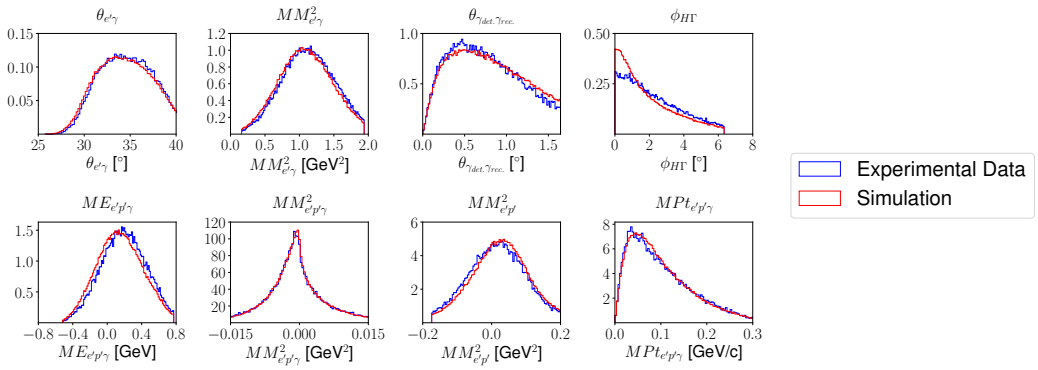

Figure 5-5: The kinematic and exclusivity variables of BH-DVCS candidates with (FD, FD) topology and outbending polarity configuration. The blue curves are the experimental distributions and the red curves are the simulation distributions.

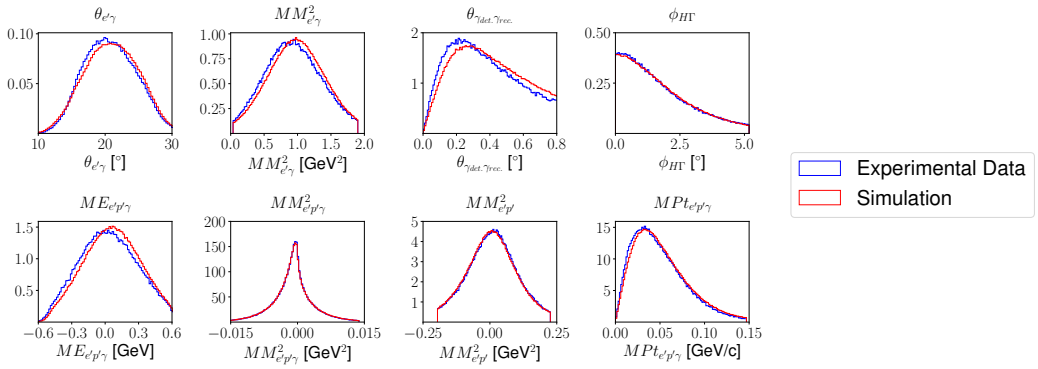

Figure 5-6: The kinematic and exclusivity variables of BH-DVCS candidates with (CD, FD) topology and outbending polarity configuration. The blue curves are the experimental distributions and the red curves are the simulation distributions.

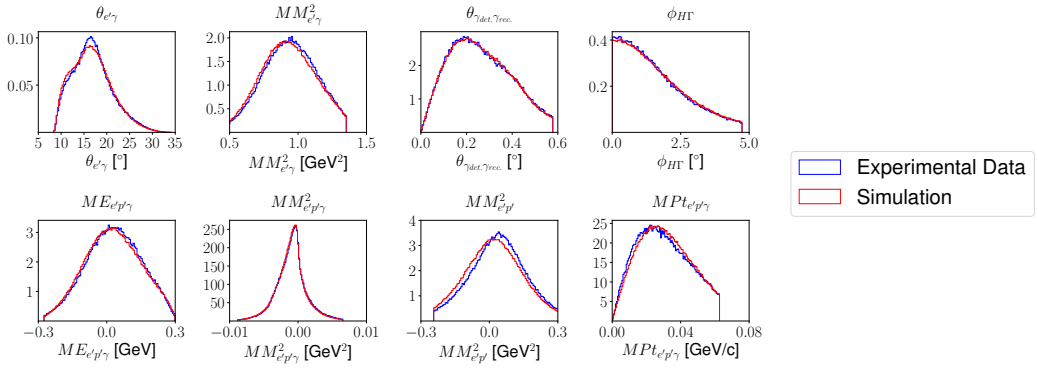

Figure 5-7: The kinematic and exclusivity variables of BH-DVCS candidates with (CD, FT) topology and outbending polarity configuration. The blue curves are the experimental distributions and the red curves are the simulation distributions.

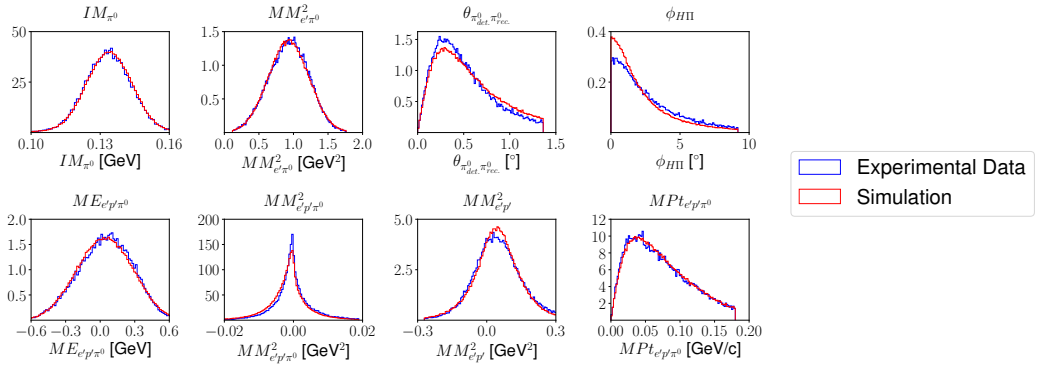

Figure 5-8: The kinematic and exclusivity variables of DVπ^0P candidates with (FD, FD) topology and inbending polarity configuration. The blue curves are the experimental distributions and the red curves are the simulation distributions.

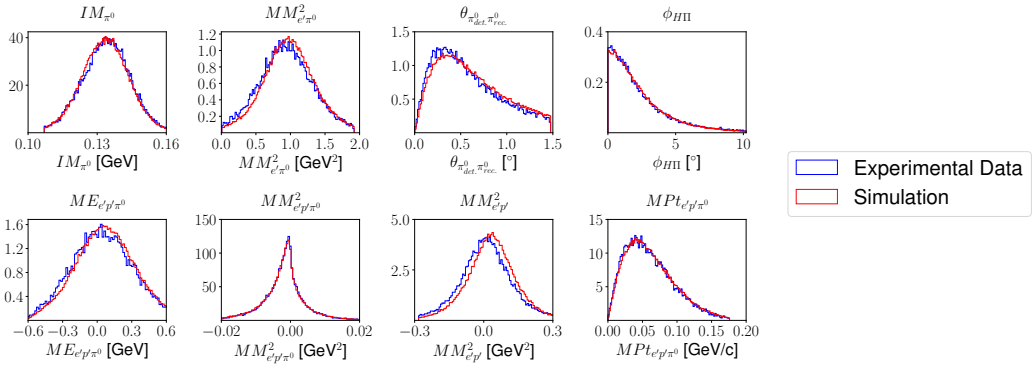

Figure 5-9: The kinematic and exclusivity variables of DVπ^0P candidates with (CD, FD) topology and inbending polarity configuration. The blue curves are the experimental distributions and the red curves are the simulation distributions.

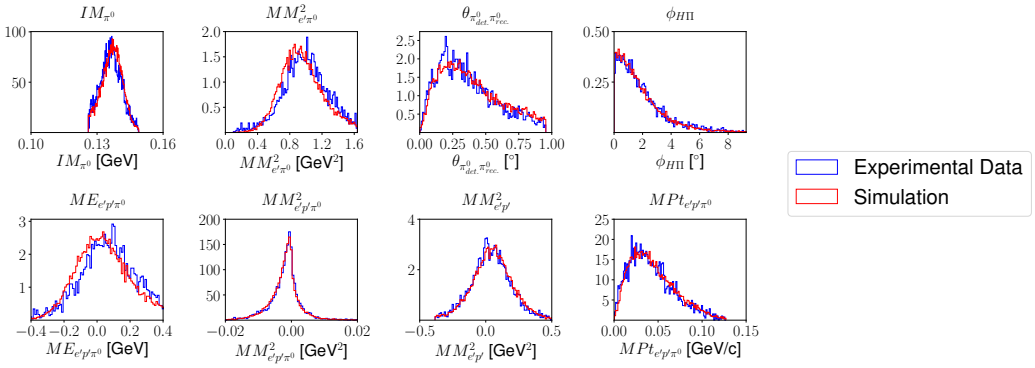

Figure 5-10: The kinematic and exclusivity variables of DVπ^0P candidates with (CD, FT) topology and inbending polarity configuration. The blue curves are the experimental distributions and the red curves are the simulation distributions.

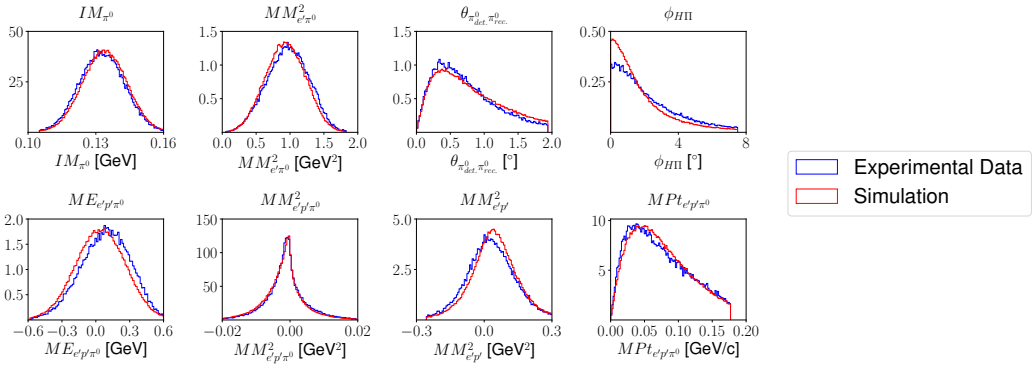

Figure 5-11: The kinematics and exclusivity variables of DVπ^0P candidates with (FD, FD) topology and outbending polarity configuration. The blue curves are the experimental distributions and the red curves are the simulation distributions.

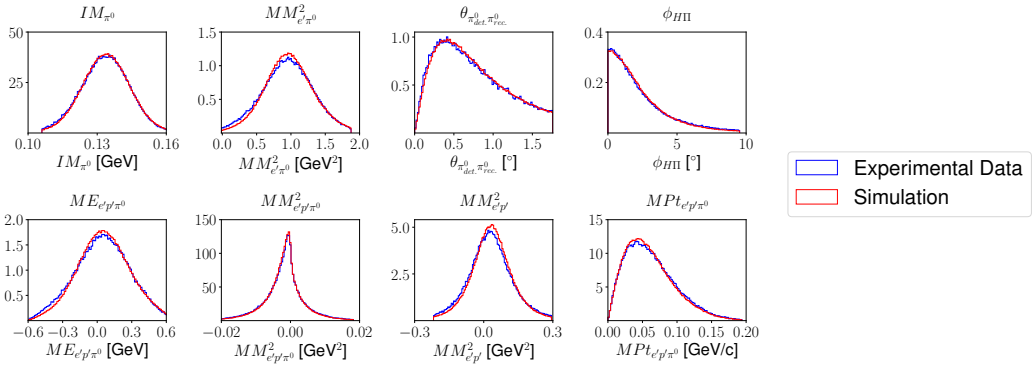

Figure 5-12: The kinematic and exclusivity variables of DVπ^0P candidates with (CD, FD) topology and outbending polarity configuration. The blue curves are the experimental distributions and the red curves are the simulation distributions.

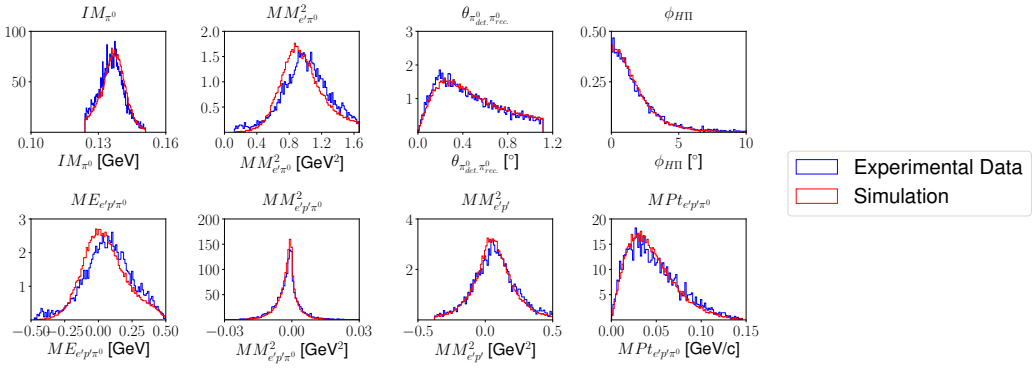

Figure 5-13: The kinematic and exclusivity variables of DVπ^0P candidates with (CD, FT) topology and outbending polarity configuration. The blue curves are the experimental distributions and the red curves are the simulation distributions.

Table 5.3: The excluded regions in PCAL for the electrons and photon reconstruction. The unit of l_U, l_V, l_W is in cm.

1	2	3	4	6
74< l_W <79.8	111.2< l_U <119.3	l_W <14	l_V <14	170< l_W <192
83.6< l_W <92.2	113< l_V <118.7		229.4< l_V <240.7	
212.5< l_W <230	l_W <14		135< l_W <150	

possibility that multiple $e'p'\gamma$ or $e'p'\gamma\gamma$ exclusive sets in one exclusive event. But, the multiple exclusive sets do not result in large uncertainties for following reasons. First, the number of exclusive events are not augmented by counting multiple exclusive sets in the same event because they are still in the same event. Second, the number of exclusive events that contain multiple exclusive sets are negligible. The estimates of such events in $ep \to e'p'\gamma$ channel are 1.7%, 0.2%, 1.5% and 0.2% for inbending experimental, inbending simulation, outbending experimental and outbending simulation data respectively. However, the existence of multiple exclusive sets in one event complicate connecting the survival rates of individual PID cut to its effect on the number of exclusive events.

The remaining part of this section describes the additional PID cuts to those introduced in Chapter 2. The PID cuts in Chapter 2 were mostly developed for the BSA studies without meticulous discussions regarding the inefficiencies. To improve the data quality, some inefficient regions at detector local coordinates were further surveyed and removed.

The electrons and photons in the experimental data sets were not properly reconstructed when they were recorded in certain PCAL regions. As these inefficient zones were not excluded in the simulation, the electrons and photons that are associated with the (l_U, l_V, l_W) coordinates in Table 5.3 were excluded.

The CVT has 12 layers in total with the 6 inner layers of SVT and the other 6 outer layers of BMT. The 2D histogram of two polar angles, the reconstructed $\theta_{p'}$ at vertex and the polar angle coordinate of the detector hit position θ_{CVT}, is presented in Fig. 5-14. The plot implies that the reconstruction quality drops at the detector borders, which can be confirmed at the 1D histograms of $\theta_{p'}$ and θ_{CVT}.

Here, we propose a quadrangle-shaped fiducial cut in the $\theta - \theta_{\mathrm{CVT}}$ plane, and excluding three ϕ_{CVT} regions, (-95°, -80°), (25°, 40°) and (143°, 158°). The boundaries of the quadrangle were inferred by the experimental data distribution and the experimental data to simulation ratio of normalized distributions (Figs. 5-15–5-17). The sides of the quadrangle were similarly determined by collecting the edges of θ_{CVT} for a 1° window of $\theta_{p'} \in (45°, 65°)$. The edges were defined as the intersections of 50% height of the peak and the distribution, i.e., the bin with bin contents $\sim 1/2$ peak, or the Full Width at Half Maximum (FWHM). Explicitly, the quadrangle is defined as follows.

$$\theta_{p'} \leq 64.23° \tag{5.1}$$

$$\theta_{\mathrm{CVT}} \geq 44.5° \tag{5.2}$$

$$\theta_{\mathrm{CVT}} \leq -2.924 + 1.274 \times \theta_{p'} \tag{5.3}$$

$$\theta_{\mathrm{CVT}} \geq -3.523 + 1.046 \times \theta_{p'}. \tag{5.4}$$

Note that the reconstructed polar angle cut (eqn. 5.1) was applied after the momentum post-processing procedure introduced in Chapter 4. Similarly, the borders on ϕ_{CVT} (-95°, -80°), (25°, 40°) and (143°, 158°) were determined by investigating the density ratio of experimental data to the simulation data.

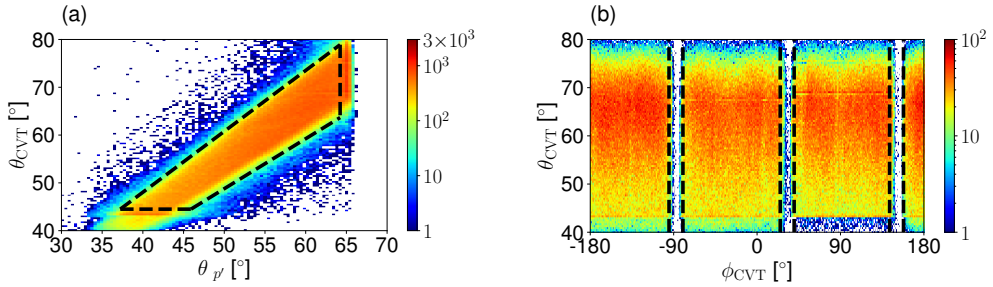

Figure 5-14: The proton fiducial cuts in the Central Detectors used in this analysis. Presented are (a) the 2D histogram of θ_{CVT} and $\theta_{p'}$ and (b) the 2d histogram of θ_{CVT} and ϕ_{CVT}. The red dotted lines define the fiducial cuts developed for this analysis.

In addition to the CVT fiducial cuts, the protons have 3σ cuts on χ and $vz_{e'} - vz_{p'}$ that are separately defined for each data set: inbending and outbending experimental data, and inbending and outbending simulation data. These 3σ windows are defined

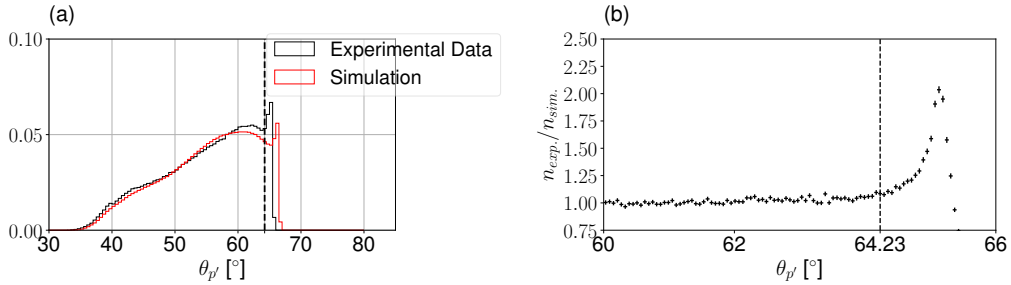

Figure 5-15: The proton polar angle ($\theta_{p'}$) to determine the maximum polar angle value. Panel (a) shows the 1D distribution of the $\theta_{p'}$ that behaves irregularly above some limits. Panel (b) shows the limit of $\theta_{p'}$ determined by the ratio of the experimental distribution (normalized density) to the simulation distribution.

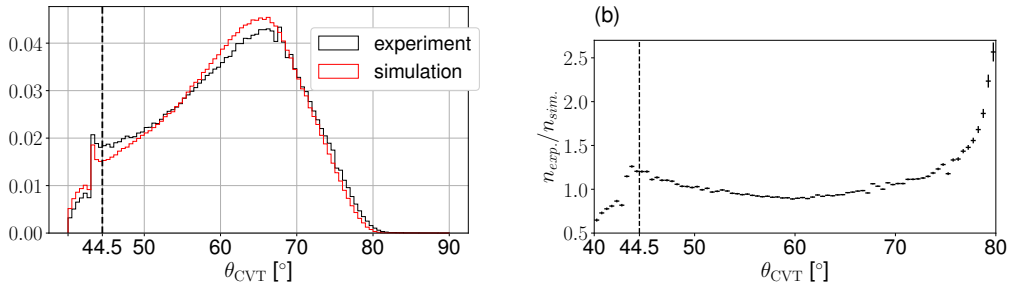

Figure 5-16: The proton polar angle ($\theta_{p'}$) to determine the maximum polar angle value. Panel (a) shows the 1D distribution of the θ_{CVT} that behaves irregularly below some limits. Panel (b) shows the limit of θ_{CVT} determined by the ratio of the experimental distribution (normalized density) to the simulation distribution.

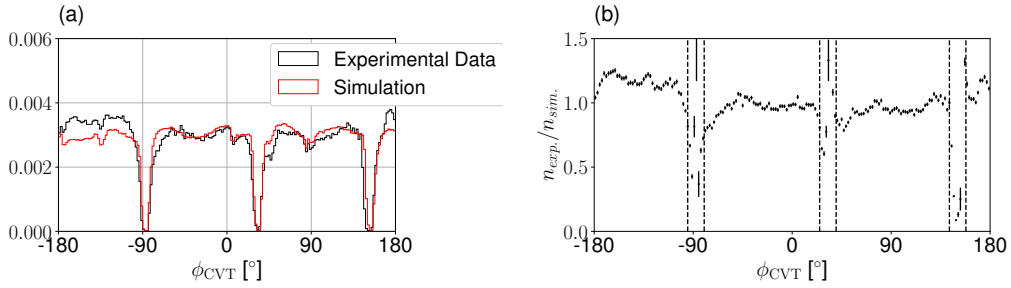

Figure 5-17: The proton CVT hit azimuthal coordinate (ϕ_{CVT}) to determine the fiducial regions. Panel (a) shows the 1D distribution of the ϕ_{CVT} that shows the poorly reconstructed regions. Panel (b) shows the exact boundaries determined by the ratio of the experimental distribution (normalized density) to the simulation distribution.

Table 5.4: 3σ windows of proton χ that are defined for each data set and detector configuration. The column heads use the abbreviations "Exp." for experimental data, "Sim." for simulation data, "Inb." for inbending, and "Outb." for outbending.

	Exp. Inb.	Sim. Inb.	Exp. Outb.	Sim. Outb.
CD	(-5.00, 6.345)	(-5.47, 6.273)	(-5.592,6.785)	(-5.629, 6.404)
FD Sector 1	(-3.296, 3.508)	(-3.362, 3.403)	(-3.905 4.088)	(-4.110, 4.150)
FD Sector 2	(-3.552, 4.000)	(-4.051, 3.907)	(-3.411 3.939)	(-4.554, 4.708)
FD Sector 3	(-3.446, 3.937)	(-3.697, 3.702)	(-4.042 5.954)	(-3.934, 4.170)
FD Sector 4	(-2.747, 3.190)	(-3.837, 3.792)	(-3.820 5.065)	(-4.062, 4.346)
FD Sector 5	(-2.851, 3.418)	(-3.756, 3.672)	(-3.384 4.232)	(-4.404, 4.457)
FD Sector 6	(-3.174, 3.514)	(-3.402, 3.351)	(-5.077 5.100)	(-4.222, 4.000)

Table 5.5: 3σ windows of proton $vz_{e'} - vz_{p'}$ that are defined for each data set and detector configuration. The column heads use the abbreviations "Exp." for experimental data, "Sim." for simulation data, "Inb." for inbending, and "Outb." for outbending.

	Exp. Inb.	Sim. Inb.	Exp. Outb.	Sim. Outb.
CD	(-2.011, 2.314)	(-1.268, 1.478)	(-2.737, 2.096)	(-1.473, 1.657)
FD Sector 1	(-3.209, 4.017)	(-3.398, 3.611)	(-4.435, 3.429)	(-3.407, 3.015)
FD Sector 2	(-3.612, 4.139)	(-3.633, 3.756)	(-4.646, 2.978)	(-3.389, 2.971)
FD Sector 3	(-3.328, 4.287)	(-3.714, 3.831)	(-3.922, 3.040)	(-3.480, 3.054)
FD Sector 4	(-3.411, 4.108)	(-3.406, 3.548)	(-4.646, 3.493)	(-3.387, 2.972)
FD Sector 5	(-3.607, 4.246)	(-3.289, 3.519)	(-3.901, 3.750)	(-3.383, 2.960)
FD Sector 6	(-2.999, 3.927)	(-3.561, 3.748)	(-3.846, 3.623)	(-3.573, 3.088)

by performing the gaussian cuts on the CD, and each sector of FD and described at Tables 5.4–5.5.

The additional FT-Cal fiducial cuts were defined for 4 small perforations that are marked in Fig. 5-18. The covers were designed as circles that include the perforation with the smallest possible size. The locations and radii of circles are as follows.

$$r = 1.60 \text{ cm} \qquad \text{center} = (-8.42,\ 9.89) \text{ cm} \qquad \text{(circle 1)} \tag{5.5}$$

$$r = 1.60 \text{ cm} \qquad \text{center} = (-9.89,\ -5.33) \text{ cm} \qquad \text{(circle 2)} \tag{5.6}$$

$$r = 2.30 \text{ cm} \qquad \text{center} = (-6.15,\ 13.00) \text{ cm} \qquad \text{(circle 3)} \tag{5.7}$$

$$r = 2.00 \text{ cm} \qquad \text{center} = (-6.50,\ 3.70) \text{ cm} \qquad \text{(circle 4)} \tag{5.8}$$

The effects of the PID cuts on the exclusive channel can be estimated by the

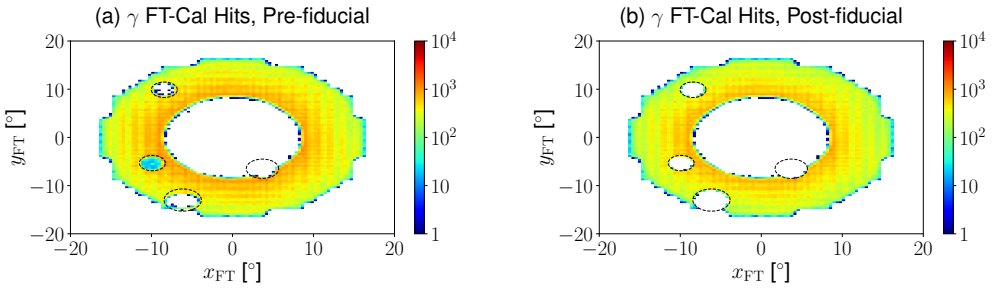

Figure 5-18: The 2D histograms of p' hit positions y_{FT} and x_{FT} of the photon candidate (a) before the RG-A PID cuts and (b) after the FT fiducial cuts for the concatenated data set of inbending and outbending polarities.

number of exclusive event after each cut. Table 5.6 list the survival rate for each particle by each PID cut. Here, the survival rate was defined as the ratio of the number survived relevant exclusive events after each PID cuts to the number of exclusive events with EB PID. By relevant, it means that the cuts on specific configuration must be defined over the configuration. For example, the survival rate by the proton DC fiducial cut should be surveyed for the FD protons.

The final level event selections are defined as follows.

1. $p_{e'} > 2$ GeV/c
2. $p_{\gamma} > 2$ GeV/c (BH-DVCS), $p_{\gamma_2} > 0.4$ GeV/c (DVπ^0P)
3. $p_{p'} > 0.3$ GeV/c (CD), 0.42 GeV/c (FD, Inb.), 0.5 GeV/c (FD, Outb.)
4. $Q^2 > 1$ (GeV/c)^2
5. $W > 2$ GeV
6. The electrons reconstructed in the same sector with photons were excluded.
7. The protons reconstructed in the same sector with photons were excluded when the protons have associated hits in the FD ECAL.
8. The PID cuts defined in Section 2.4 and this section were applied.
9. The 3σ exclusivity cuts described in this section were applied.

Table 5.6: The survival rates of each fiducial cut on the electrons, protons and photons that are marked at the row headers. The last three rows show the survival rates applied to the corresponding detector configuration. The columns 'Exp. Inb.', 'Sim. Inb.', 'Exp. Outb.' and 'Sim. Outb.' list the survival rates themselves at the corresponding configuration. The other columns 'Exp.:Sim. Inb.' and 'Exp.:Sim. Outb.' show the double ratio of the ratio of the survival rates at experimental data to the survival rates at simulation data.

	Exp. Inb.	Sim. Inb.	Exp.:Sim. Inb.	Exp. Outb.	Sim. Outb.	Exp.:Sim. Outb.
e' PCAL	86.3%	76.0%	113.6%	95.4%	94.4%	101.1%
e' DC	96.3%	90.2%	106.8%	89.1%	82.8%	107.7%
e' SF	90.6%	83.1%	109.1%	99.0%	98.9%	100.1%
e' vz	99.9%	99.9%	100.0%	99.9%	99.9%	100.0%
e' $E_{dep.}$	100.0%	100.0%	100.0%	100.0%	100.0%	100.0%
e' anti-π^-	93.9%	93.5%	100.4%	97.5%	98.5%	99.0%
p' DC	99.6%	98.6%	101.1%	97.3%	95.1%	102.3%
p' CVT	83.0%	76.8%	108.1%	65.2%	65.5%	99.5%
p' χ	96.0%	96.4%	99.5%	96.3%	97.2%	99.1%
p' $vz_{e'} - vz_{p'}$	91.8%	94.7%	96.9%	91.6%	94.5%	97.0%
γ β	99.7%	100.0%	99.7%	99.9%	100.0%	99.9%
γ PCAL	94.1%	90.8%	103.5%	92.1%	89.8%	99.6%
γ FT	98.5%	94.8%	103.9%	98.7%	94.7%	104.2%
(FD, FD)	62.8%	60.4%	104.1%	60.3%	55.6%	108.4%
(CD, FD)	54.8%	45.5%	120.6%	54.3%	49.1%	110.6%
(CD, FT)	59.9%	49.1%	122.0%	38.9%	34.7%	112.1%

5.3 Multidimensional Binning

It is important to choose an optimal multidimensional binning scheme for the cross section extraction. In this thesis, the bin shape was designed to be a four dimensional box. Some bins are not well fitted into the box due to the phase space condition. For example, Fig. 5-19 shows several triangular bins in the $Q^2 - x_B$ plane at the left side, whose hypotenuse is determined by $p_{e'} > 2$ GeV/c.

The advantage of finer binning is to provide improved density estimation. The acceptance corrections and the finite bin width effects should increase with the bin size. However, the bin size cannot be narrower than the effective resolutions in the binning variables to minimize bin migration. Extremely small bins would not have any statistical significance in each bin, which would lead to an invalid analysis. It is important to determine the optimal binning.

The different proton momentum thresholds were considered for the $|t|$ binning. The momentum thresholds required for the proton momentum reconstruction, 0.3 GeV/c for CD, 0.42 GeV/c for FD inbending, 0.5 GeV/c for FD outbending lead to $|t|$ threhsold of 0.09, 0.17 and 0.23 GeV^2 respectively. To consider the bin migration effect, the $|t|$ bin was loosely set as [0.110, 0.150, 0.250, 0.400, 0.600, 0.800, 1.000] GeV^2. The number of events in the first bin was estimated with CD protons only. Likewise, the FD outbending data was not used for the second bin event counting. There are not enough statistics above |t|=1 GeV^2 to determine the cross sections with reasonable precision from the RG-A fall 2018 data alone.

The $Q^2 - x_B$ phase space was evenly divided by the bin edges [1.000, 1.200, 1.456, 1.912, 2.510, 3.295, 4.326, 5.761, 7.000] (GeV/c)^2 and [0.062, 0.090, 0.118, 0.155, 0.204, 0.268, 0.357, 0.446, 0.581]. The $Q^2 - x_B$ bin boundaries are presented in $Q^2 - x_B$ plane with the 2D histogram of entire experimental data set in Fig. 5-19 with an explanation of the kinematics boundaries at the caption.

The ϕ distributions are binned in equal width bins of width 15°. Other possible binning schemes include (1) the adjusted equal width binning to widen the bin width at the central region to compensate for low statistics, and (2) the equal frequency

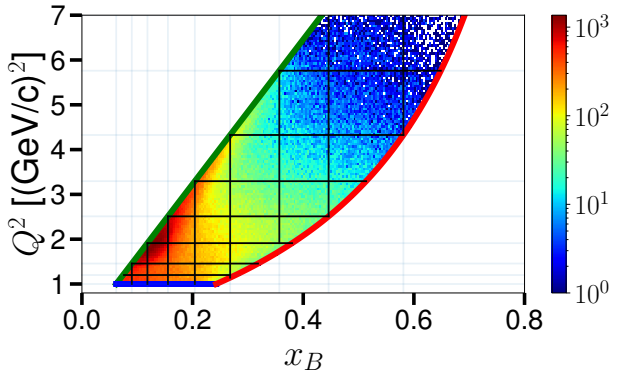

Figure 5-19: The 2D histograms of events in Q^2 and x_B for each configuration of final level BH-DVCS events. The kinematic regions are bordered by the certain required conditions: (1) $p_{e'} > 2$ GeV/c (green), (2) $Q^2 > 1$ (GeV/c)^2 (blue) and (3) $W > 2$ GeV (red).

binning. The chosen binning scheme has three advantages; (1) the binning scheme is symmetric with respect to $\phi = 180°$, (2) the frequency is directly translated into the probability distribution in the same $Q^2 - x_B - |t|$ bin, and (3) it was used by other experiments [107, 129].

The radiative events in BH-DVCS and DVπ^0P channels are simulated with the following condition with leeway to allow for the bin migration.

1. -5.5 cm$< vz_{e'} <$-0.5 cm
2. $W >$1.9 GeV
3. $E_{beam} =$ 10.604 GeV
4. 0.9 (GeV/c)$^2 < Q^2 <$14 (GeV/c)^2
5. 0.05$< x_B <$0.85
6. $p_{\gamma'} > 0.1$ GeV/c

The last condition on $p_{\gamma'}$ should be applied to the radiated photons γ'. The *dvcsgen* requires the upper bound of $|MM^2_{e'p'}|$ for the radiative event generation [180], which was set as 0.6 GeV^2 for this work.

The BH-DVCS events, once simulated without any thresholds of Q^2 and $|t|$, mostly end up simulated in the low Q^2 and $|t|$ regions as the cross sections are the highest in

such region. The lower limits of Q^2 and $|t|$ were reinforced to skirt this issue in a way that does not harm the interested kinematic bins. The thresholds were surveyed with sample simulation without the Q^2 and $|t|$ thresholds. The inbending data set extends up to Q^2 $\sim$1.4 (GeV/c)^2 at reconstructed momentum. To avoid bin migration, the Q^2 threshold at the event generation was set to $Q^2 > 1.2$ (GeV/c)^2 for the inbending polarity. The outbending data set extends to Q^2 $\sim$1 (GeV/c)^2, so the threshold was set to be 0.9 (GeV/c)^2. The proton momentum reconstruction threshold is the lowest in the CD at 0.3 GeV/c, which leads to a $|t|$ threshold as 0.085 GeV^2. As discussed in Section 3.3, the BH-DVCS $|t|$ upper limit is 1.79 GeV^2, well above the $|t|$ bin volume edge of $|t|$=1 GeV^2. The BH-DVCS event generation has an additional constraint on y: 0.19$< y <$0.85. This cut on y was placed to be consistent with the reconstructed electron momentum $p_{e'} > 2$ GeV/c.

The large statistics simulation was performed on the CLAS12 off-site simulation system that efficiently carries out the simulation using available cycles at computing centers worldwide including the MIT High Performance Research Computing Facility (HPRCF) at the Bates Research and Engineering Center through the Open Science Grid (OSG) [187, 188]. The simulation size was determined to be large enough to contain about 10 times the statistics of the experimental data in each topology to reduce the statistical uncertainty on one hand. On the other hand, the size was constrained by the fact that the computing resources and the storage quota assigned to the CLAS collaboration at the Jefferson Lab computing farm are shared among all users in the collaboration. The genearated events before the detector simulation are in Table 5.7.

Table 5.7: Statistics of the generated events before the detector simulation. The first three column headers indicate the simulated exclusive channels. The last column is the background merging currents that were used for the simulation. The row headers show the torus polarity. The last row is the simulation of the early outbending run with the torus current at +1.00796 times the nominal value.

	BH	BH-DVCS	DVπ^0P	Bkg. Merging
Inb.	200M	200M	100M	45 nA
	200M	200M	300M	50 nA
	200M	200M	100M	55 nA
	0	0	100M	Not used
	600M	600M	600M	Subtotal
Outb.	300M	300M	300M	50 nA
	300M	300M	100M	40 nA
	0	0	100M	Not used
	300M	300M	100M	40 nA (+1.00796)
	900M	900M	600M	Subtotal

5.4 Signal Yields and Acceptance Corrections

The raw yields are defined as the event counts in each bin before the background subtraction and the acceptance corrections. The CLAS12 detector has the three event topologies as discussed in Chapter 3. The event topologies are principally defined by the proton and photon angles. There is a small overlap between the FD and the CD detectors so that the same proton can be reconstructed in both detector system. However, the uncertainty from the duplicated measurement can be ignored as discussed in Section 5.2.

Typically, the acceptances are defined as $n_{rec.}/n_{gen.}$ in the simulation, where $n_{rec.}$ is the number of reconstructed events in the detector system. The acceptances were regarded as the probability to record the event in the detector. The caveat is that the simulation and the experimental data set can differ in the relative efficiencies among the detector subsystems. Matching the MC simulation with the experimental data set in terms of the resolution and the efficiency is a significant ongoing effort within the CLAS12 collaboration while this thesis is being written. To avoid this factor, the detector specific acceptance correction were performed. The sub-acceptances were defined as $n_{rec.,(FD,FD)}/n_{gen.,(FD,FD)}$, $n_{rec.,(CD,FD)}/n_{gen.,(CD,FD)}$,

and $n_{rec.,(CD,FT)}/n_{gen.,(CD,FT)}$ to invert the detected event counts. The denominators $n_{gen.,j}$ are the event candidates that can be reconstructed in the corresponding topology j. Simply,

$$j = \text{(FD, FD)} \qquad (\theta_\gamma \geq 5^\circ, \theta_{p'} < 40^\circ) \tag{5.9}$$

$$j = \text{(CD, FD)} \qquad (\theta_\gamma \geq 5^\circ, \theta_{p'} < 40^\circ) \tag{5.10}$$

$$j = \text{(CD, FT)} \qquad (\theta_\gamma < 5^\circ, \theta_{p'} \geq 40^\circ) \tag{5.11}$$

This method should consider the ratio of $n_{gen.,(FD,FD)} + n_{gen.,(CD,FD)} + n_{gen.,(CD,FT)}$ to $n_{gen.}$, which is usually 1. After the acceptance correction, the two data sets, inbending and outbending, were merged into common bins. The cross sections at the lowest two Q^2 bins are only filled by the outbending polarity data set.

The detector specific acceptance correction method stated above is referred to as "Acc. Separately" in Fig. 5-20. The figures of merit related to acceptance with the entire detector configuration, i.e., $(n_{rec.,(FD,FD)}+n_{rec.,(CD,FD)}+n_{rec.,(CD,FT)})/(n_{gen.,(FD,FD)} + n_{gen.,(CD,FD)}+n_{gen.,(CD,FT)})$ is presented as "Acc. Entirely". The systematic effect from using the different cross section models for the event generation was considered by simulating the pure BH and the BH-DVCS based on the VGG model. For the detector specific acceptance correction method, the effective acceptance was defined as the ratio of acceptance corrected yields to the number of generated events.

The reconstruction efficiencies drop in the measurements with higher beam current as discussed in Section 3.5.1. To consider this effect, the detector simulation was performed with various background merging currents (Table 5.7). The drops in reconstruction efficiency by the beam current was appproximately global for the entire bin. So, the data sets associated with various beam currents and background merging currents were merged for increasing statistics. The small deviation from nominal beam current was considered as the source of systematic uncertainty. The raw yields in the interested bin volume that passed the final level BH-DVCS and DVπ^0P selections are in Table 5.8.

The background estimation was performed for each detector subsystem by us-

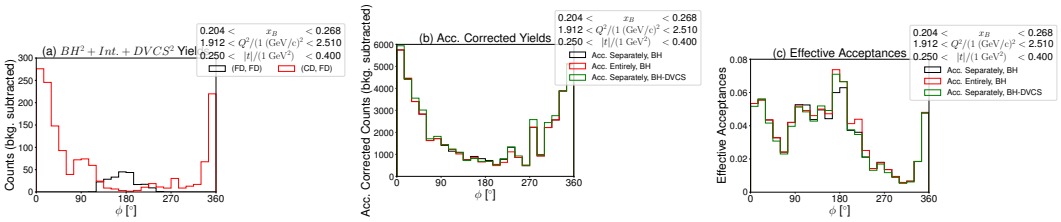

Figure 5-20: The raw yields and the acceptance correction steps in $0.204 < x_B < 0.268$, $1.912\ (\mathrm{GeV/c})^2 < Q^2 < 2.510\ (\mathrm{GeV/c})^2$, $0.25\ \mathrm{GeV}^2 < |t| < 0.40\ \mathrm{GeV}^2$. Panel (a) shows the raw yields detected at (FD, FD) and (CD, FD) that are shown as black and red histograms. Panels (b) and (c) show the accepted corrected yields and effective acceptances, which are shown as bar graphs. The colors of bar graphs are black, red and green for the detector specific acceptance method with pure BH simulation, the entire acceptance correction method with pure BH simulation and the detector specific acceptance method with BH-DVCS simulation respectively.

Table 5.8: Statistics of the generated events after the detector simulation. The column headers indicates the polarities and the detector configuration.

	Configuration	BH	BH-DVCS	DVπ^0P	DVπ^0P Misidentified
Inb.	Sim. (FD, FD)	95K	306K	207K	96K
	Sim. (CD, FD)	442K	607K	139K	27K
	Sim. (CD, FT)	1751K	1514K	197K	3K
	Exp. (FD, FD)	N/A	20K	21K	N/A
	Exp. (CD, FD)	N/A	45K	19K	N/A
	Exp. (CD, FT)	N/A	138K	3K	N/A
Outb.	Sim. (FD, FD)	12K	94K	142K	75K
	Sim. (CD, FD)	397K	735K	521K	132K
	Sim. (CD, FT)	748K	651K	35K	4K
	Exp. (FD, FD)	N/A	27K	28K	N/A
	Exp. (CD, FD)	N/A	167K	105K	N/A
	Exp. (CD, FT)	N/A	188K	6K	N/A

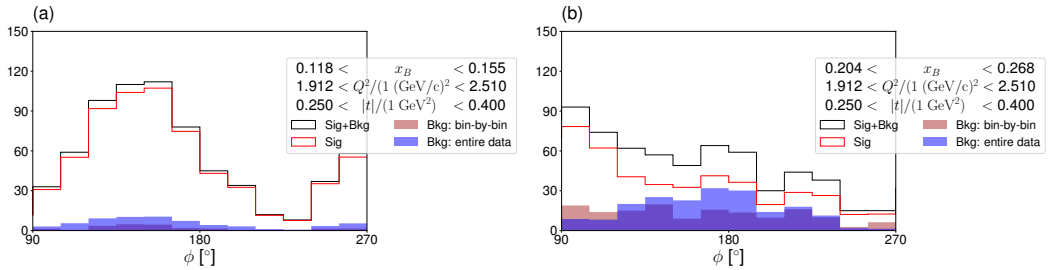

Figure 5-21: The raw yields and the background contamination. Presented bins are (a) 0.118< x_B <0.155, 1.912 (GeV/c)^2 < Q^2 <2.510 (GeV/c)^2, 0.250 GeV^2 < $|t|$ <0.400 GeV^2 and (b) 0.204< x_B <0.268, 1.912 (GeV/c)^2 < Q^2 <2.510 (GeV/c)^2, 0.25 GeV^2 < $|t|$ <0.40 GeV^2.

ing the DVπ^0P simulation (Fig. 5-21). Practically, the contamination ratio $c = \frac{N(e'p'\gamma)^{\mathrm{DV}\pi^0\mathrm{P}}_{\mathrm{exp.}}}{N(e'p'\gamma)^{e'p'\gamma}_{\mathrm{exp.}}}$ was assigned event by event after the background estimation in the arbitrary binning scheme. The statistical uncertainty in the contamination ratio was also assigned at this step. The background estimation binning scheme is not necessarily the same with the binning scheme for the cross section extraction. The total contamination is defined as the weighted event counts when the weight is the contamination ratio. The differences between the total contamination from the binning scheme results in the systematic uncertainties.

5.5 Radiative Corrections

The radiative corrections were performed using the method described in Section 3.6.1. There were two steps; The first step is the conversion of the integrated radiative cross section to the integrated Born cross section, and the next step is the conversion of the integrated Born cross section to the Born cross sections at one fixed kinematics as stated in Section 3.6. Even though the two steps are correlated, it is useful to separate them to study the systematic effects from using different cross section models. The one bin examples of radiative correction and the finite bin size correction using the pure BH are presented in Fig. 5-22.

The phase spaces are shared among the Born and radiative cross sections and the four dimensional kinematic distributions over (x_B, Q^2, $-t$, ϕ) are slightly different.

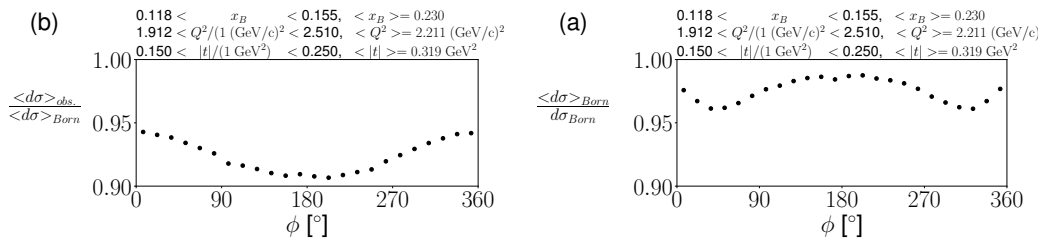

Figure 5-22: The two steps in applying radiative corrections. The radiative correction (a) and the finite bin size correction (b) using the pure BH are presented at the bin 0.118< x_B <0.155, 1.912 (GeV/c)^2 < Q^2 <2.510 (GeV/c)^2, 0.150 GeV^2 < $|t|$ <0.250 GeV^2.

To estimate the RC factors and finite bin size correction factors efficiently, the *dvcsgen* were programmed to print out the exact value of Born and radiative cross sections at the same kinematic points. Even though the MC data set follows the radiative cross sections as the probability distribution, the RC factors from this method are consistent within small uncertainty limits. The averaged Born cross sections is canceled when the RC factors and finite bin size correction were calculated based on the correct cross section model. Therefore, $F_{rad} \times F_{bin}$ were taken as the correction factors for the analysis, and the model uncertainties were estimating by F_{rad} and F_{bin} for the pure BH and BH-DVCS with VGG model.

5.6 Normalization and the Modified Cross Sections

The accumulated beam charges for BH-DVCS candidates are 30.40 mC for the inbending and 32.09 mC for the outbending polarities . The integrated charge 1 mC leads to 1.324 fb^{-1} for the 5 cm LH_2 target. Accordingly, the integrated luminosities are 40.25 fb^{-1} for the inbending and 42.49 fb^{-1} for the outbending, respectively. The charge is used to normalize the acceptance-corrected event counts.

The discrepancies between the detector efficiencies of the experimental apparatus and those in the MC simulation generate the detector efficiency corrections. While these are studied in the software work in the collaboration, the following strategy is used in this thesis to estimate the global normalization factor. The BH contribu-

tion to the unpolarized cross section is expected to be dominant at sufficiently high x_B, Q^2, y and sufficiently low $|t|$ at $\phi = 0,\ 360\ ^\circ$. The unpolarized cross sections $d\sigma_{unpol.}$ can be decomposed into the pure BH, the pure DVCS and the interference contributions $d\sigma_{unpol.,BH^2}$, $d\sigma_{unpol.,DVCS^2}, d\sigma_{unpol.,Int.}$ that can be expressed with the kinematics prefactor and cosine series of ϕ.

$$d\sigma_{unpol.,BH^2} = \Gamma \frac{1}{x_B^2 y^2 (1+\epsilon^2)^2 t \mathcal{P}_1(\phi)\mathcal{P}_2(\phi)} (c_0^{\mathrm{BH}} + c_1^{\mathrm{BH}} \cos(\phi) + c_2^{\mathrm{BH}} \cos(2\phi)) \quad (5.12)$$

$$d\sigma_{unpol.,DVCS^2} = \Gamma \frac{1}{y^2 Q^2} (c_0^{\mathrm{DVCS}} + c_1^{\mathrm{DVCS}} \cos(\phi) + c_2^{\mathrm{DVCS}} \cos(2\phi)) \quad (5.13)$$

$$d\sigma_{unpol.,Int.} = \Gamma \frac{1}{x_B y^3 t \mathcal{P}_1(\phi)\mathcal{P}_2(\phi)} (c_0^{\mathcal{I}} + c_1^{\mathcal{I}} \cos(\phi) + c_2^{\mathcal{I}} \cos(2\phi) + c_3^{\mathcal{I}} \cos(3\phi)). \quad (5.14)$$

The ϕ dependence in the BH prefactor follows the behavior of $1/\mathcal{P}_1\mathcal{P}_2$ as other terms are related to x_B, Q^2, and $|t|$. This motivates the study of modified cross sections $\mathcal{P}_1(\phi)\mathcal{P}_2(\phi)d\sigma$ [131] [2].

The raw unpolarized cross section was fitted with the following fitting function.

$$A + B\cos(\phi) + C\cos(2\phi). \quad (5.15)$$

Results of the fitting of the reduced cross section are presented in Fig. 5-23. The normalization was derived from the ratio of $\mathcal{P}_1(0)\mathcal{P}_2(0)d\sigma(0)$ of the experimental data to the pure BH. The survey of the normalization factors in the bin at sufficiently high x_B, Q^2, y and sufficiently low $|t|$ is 75 $\pm$ 10 %.

[2] The reference defined the modified cross section as $\mathcal{P}_1(\phi)\mathcal{P}_2(\phi)(d\sigma_{unpol.,DVCS^2} + d\sigma_{unpol.,Int.})$

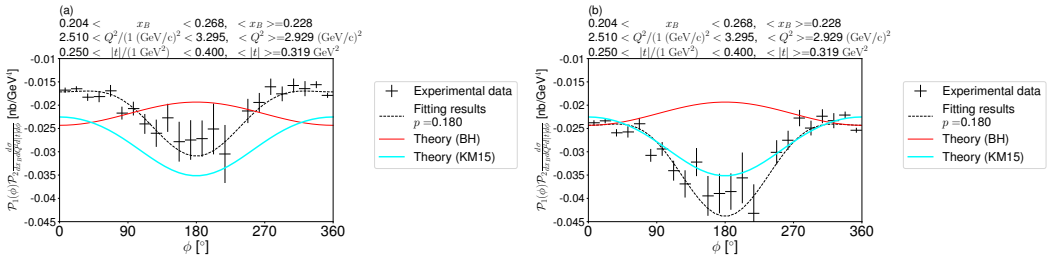

Figure 5-23: The modified cross sections (a) before the normalization and (b) after the normalization in 0.204< x_B <0.268, 2.929 $(\mathrm{GeV/c})^2$ < Q^2 <2.510 $(\mathrm{GeV/c})^2$, 0.25 GeV^2 < $|t|$ <0.40 GeV^2.

5.7 Error Analysis

The statistical uncertainty estimation can be determined using the following formulae:

$$\frac{d\sigma}{dQ^2 dx_B d|t| d\phi} \propto N(e'p'\gamma)^{\mathrm{BH-DVCS}}_{\mathrm{exp.}}/Acc. \tag{5.16}$$

$$N(e'p'\gamma)^{\mathrm{BH-DVCS}}_{\mathrm{exp.}} = N(e'p'\gamma)^{e'p'\gamma}_{\mathrm{exp.}} - N(e'p'\gamma)^{\mathrm{DV}\pi^0\mathrm{P}}_{\mathrm{exp.}} \tag{5.17}$$

$$N(e'p'\gamma)^{\mathrm{DV}\pi^0\mathrm{P}}_{\mathrm{exp.}} = N(e'p'2\gamma)^{\mathrm{DV}\pi^0\mathrm{P}}_{\mathrm{exp.}} \times \frac{N(e'p'\gamma)^{\mathrm{DV}\pi^0\mathrm{P}}_{\mathrm{sim.}}}{N(e'p'2\gamma)^{\mathrm{DV}\pi^0\mathrm{P}}_{\mathrm{sim.}}} \tag{5.18}$$

$$\delta N(e'p'\gamma)^{\mathrm{BH-DVCS}}_{\mathrm{exp.}} = \sqrt{(\delta N(e'p'\gamma)^{e'p'\gamma}_{\mathrm{exp.}})^2 + (\delta N(e'p'\gamma)^{\mathrm{DV}\pi^0\mathrm{P}}_{\mathrm{exp.}})^2} \tag{5.19}$$

$$\delta N(e'p'\gamma)^{e'p'\gamma}_{\mathrm{exp.}} = \sqrt{N(e'p'\gamma)^{e'p'\gamma}_{\mathrm{exp.}}} \tag{5.20}$$

$$\delta N(e'p'\gamma)^{\mathrm{DV}\pi^0\mathrm{P}}_{\mathrm{exp.}} = N(e'p'\gamma)^{\mathrm{DV}\pi^0\mathrm{P}}_{\mathrm{exp.}} \tag{5.21}$$

$$\times \sqrt{1/N(e'p'2\gamma)^{\mathrm{DV}\pi^0\mathrm{P}}_{\mathrm{exp.}} + 1/N(e'p'2\gamma)^{\mathrm{DV}\pi^0\mathrm{P}}_{\mathrm{sim.}} + 1/N(e'p'\gamma)^{\mathrm{DV}\pi^0\mathrm{P}}_{\mathrm{sim.}}} \tag{5.22}$$

$$Acc. = \frac{n_{rec.}}{n_{gen.}} \tag{5.23}$$

$$\frac{\delta Acc.}{Acc.} \sim \sqrt{\frac{1}{n_{rec.}}} \tag{5.24}$$

$$\sigma_{stat.} = \frac{d\sigma}{dQ^2 dx_B d|t| d\phi} \sqrt{\frac{1}{N_{rec.}} + \frac{1}{N(e'p'\gamma)^{e'p'\gamma}_{\mathrm{exp.}}} + (\frac{N(e'p'\gamma)^{\mathrm{DV}\pi^0\mathrm{P}}_{\mathrm{exp.}}}{N(e'p'\gamma)^{e'p'\gamma}_{\mathrm{exp.}}})^2 (1/N(e'p'2\gamma)^{\mathrm{DV}\pi^0\mathrm{P}}_{\mathrm{exp.}} + 1/N(e'p'2\gamma)^{\mathrm{DV}\pi^0\mathrm{P}}_{\mathrm{sim.}} + 1/N(e'p'\gamma)^{\mathrm{DV}\pi^0\mathrm{P}}_{\mathrm{sim.}})} . \tag{5.25}$$

Eqn. 5.24 assumed that the statistical uncertainty from generated events is negligible. The statistical uncertainty for the background estimation was assigned to the contamination ratio c, as discussed in Section 5.4.

The major sources of systematic uncertainties include the inefficiency drop as a function of increasing beam current, over- or underestimation of the smearing parameter, over- or underestimation of the π^0 background, and the radiative corrections. Alternative exclusivity cuts at 2σ (Table 5.9) and 4σ ranges (Table 5.10) were applied to investigate the systematic uncertainties. Additionally, the individual particle selection cuts can have different impacts in the experimental data and the simulation data. The most unstable cuts are the CD proton polar angle ceiling cut (64.23°), and the electron sampling fraction cut. The CD proton ceiling was adjusted to 59.23° and the electron sampling fraction cut of 3.5σ range was refined to 3σ to test the systematic effects. The resolution matching quality can affect the systematics, so the smearing parameter adjusted by 90% and 110% was applied to the total cross section contributions. The systematic uncertainty due to the π^0 background can be determined by estimating $\frac{N(e'p'2\gamma)^{\mathrm{DV}\pi^0\mathrm{P}}_{\mathrm{exp.}}}{N(e'p'2\gamma)^{\mathrm{DV}\pi^0\mathrm{P}}_{\mathrm{sim.}}}$ in different ways —bin-by-bin, or averaged in the entire kinematics region. The beam current contribution was estimated by simulating the DVCS and the DVπ^0P events at different background merging currents.

The systematic uncertainties in the unpolarized cross sections are summarized in Table 5.11.

Table 5.9: The lower and upper bounds for the $ep \to e'p'\gamma$ event selection within 2σ window.

	Inb. (FD, FD)	Inb. (CD, FD)	Inb. (CD, FT)	Outb. (FD, FD)	Outb. (CD, FD)	Outb. (CD, FT)
$lb_{MM^2_{e'p'}}$	-0.111	-0.178	-0.239	-0.116	-0.126	-0.15
$ub_{MM^2_{e'p'}}$	0.149	0.2	0.265	0.169	0.156	0.227
$lb_{MM^2_{e'\gamma}}$	0.446	0.402	0.527	0.349	0.407	0.572
$ub_{MM^2_{e'\gamma}}$	1.481	1.542	1.272	1.678	1.524	1.196
$lb_{MM^2_{e'p'\gamma}}$	-0.00693	-0.00743	-0.00439	-0.00745	-0.00456	-0.00315
$ub_{MM^2_{e'p'\gamma}}$	0.005	0.00589	0.00292	0.00553	0.00324	0.00237
$lb_{ME_{e'p'\gamma}}$	-0.511	-0.933	-0.2232	-0.828	-0.145	-0.237
$ub_{ME_{e'p'\gamma}}$	0.726	1.088	0.255	1.088	0.263	0.272
$ub_{MPt_{e'p'\gamma}}$	0.129	0.1	0.0458	0.11	0.0686	0.0487
$ub_{\theta_{\gamma_{det.}\gamma_{rec.}}}$	0.856	0.443	0.574	1.125	0.587	0.264
$ub_{\phi_{H\Gamma}}$	5.337	3.452	3.842	3.695	3.564	3.0

Table 5.10: The lower and upper bounds for the $ep \to e'p'\gamma$ event selection within 4σ window.

	Inb. (FD, FD)	Inb. (CD, FD)	Inb. (CD, FT)	Outb. (FD, FD)	Outb. (CD, FD)	Outb. (CD, FT)
$lb_{MM^2_{e'p'}}$	-0.241	-0.366	-0.491	-0.259	-0.267	-0.338
$ub_{MM^2_{e'p'}}$	0.279	0.388	0.517	0.312	0.297	0.415
$lb_{MM^2_{e'\gamma}}$	-0.177	-0.12	0.128	-0.397	-0.277	0.257
$ub_{MM^2_{e'\gamma}}$	2.127	2.074	1.672	2.45	2.22	1.512
$lb_{MM^2_{e'p'\gamma}}$	-0.0312	-0.0303	-0.0194	-0.0444	-0.0273	-0.0162
$ub_{MM^2_{e'p'\gamma}}$	0.027	0.027	0.0157	0.0374	0.0243	0.0132
$lb_{ME_{e'p'\gamma}}$	-0.881	-0.845	-0.527	-0.96	-0.898	-0.494
$ub_{ME_{e'p'\gamma}}$	1.056	0.99	0.551	1.192	1.023	0.516
$ub_{MPt_{e'p'\gamma}}$	0.251	0.119	0.14	0.341	0.131	0.0968
$ub_{\theta_{\gamma_{det.}\gamma_{rec.}}}$	1.736	0.944	0.778	2.725	1.148	0.778
$ub_{\phi_{H\Gamma}}$	11.358	6.536	7.384	7.762	6.695	6.209

Table 5.11: Major sources of systematic uncertainties. Each row presents the source of systematic uncertainty and its scale.

Sources	Typical Scale (%)
Event selection — exclusivity	11.8
Event selection — PID	12.9
Resolution matching	8.8
Acceptance corrections	9.3
Background estimation	12.8
Normalization	10
Radiative Correction	3.5
Finite bin width effect	3.6
Reconstruction efficiency	4
Total	27

5.8 Unpolarized Cross Sections

The unpolarized BH-DVCS cross sections for the nominal set-up uncertainties are presented in Figs. 5-24–5-29 for Q^2 <4.326 (GeV/c)^2, x_B <0.268, and $|t|$ <1.00 GeV^2. The theoretical predictions of the BH (red) and KM15 (cyan) curves are presented along with the data points. The BH-DVCS cross sections at higher Q^2 and x_B are presented for 0.250 GeV^2 < $|t|$ <0.800 GeV^2 in Figs. 5-30–5-32. Along with the averaged kinematic variables x_B, Q^2 and $|t|$, the bin numbers for them are presented instead of the full description of the bin for a space-efficient presentation. The bin numbers were defined in increasing order. For example, the 0-th bin of x_B is 0.062< x_B <0.90. The cross section data at the highest Q^2 bin, 5.761 (GeV/c)^2 < Q^2 <7.000 (GeV/c)^2 will optimally impose coarser binning in x_B and $|t|$ for increasing statistics and will not be presented in this thesis.

The total unpolarized cross sections $d\sigma_{unpol.}$ can be decomposed into the pure BH $d\sigma_{unpol.,BH^2}$, the pure DVCS $d\sigma_{unpol.,DVCS^2}$, and the BH-DVCS interference terms $d\sigma_{Int.}$ as discussed in Section 5.6. The pure BH cross sections $d\sigma_{unpol.,BH^2}$ are exactly calculable up to the knowledge of the elastic form factors. The remaining terms

$d\sigma_{unpol.,Int.+DVCS^2}$ are given as

$$d\sigma_{unpol.,Int.+DVCS^2} = d\sigma_{unpol.} - d\sigma_{unpol.,BH^2} \tag{5.26}$$

$$= d\sigma_{unpol.,Int.} + d\sigma_{unpol.,DVCS^2}. \tag{5.27}$$

This leads to the next steps for the CFF study [77]: (1) Rosenbluth-type separation of the Interference term and the pure DVCS term and (2) CFF extraction using each term. As a first step, it is interesting to characterize $d\sigma_{unpol.,Int.+DVCS^2}$. The typical plot of $d\sigma_{unpol.,Int.+DVCS^2}$ as a function of ϕ is shown in Fig. 5-33. The plateau region for ϕ in [90°, 270°] is found. The collection of the plateaux for the various x_B and Q^2 at one $|t|$ bin is presented in Fig. 5-34.

We define the following quantity X to quantify the interference and DVCS contribution using the plateau.

$$X \equiv \int_{\frac{\pi}{2}}^{\frac{3\pi}{2}} d\phi \frac{d\sigma}{dx_B dQ^2 d|t| d\phi}. \tag{5.28}$$

Figs. 5-35 and 5-36 show the Q^2 dependence of X at one (x_B, $|t|$) bin and $|t|$ dependence of X at one (x_B, Q^2) bin respectively. The KM15 model and experimental data agree in X as implied in Fig. 5-34.

The collection of Q^2 and $|t|$ dependence plots is presented in Figs. 5-37–5-38 for Q^2 <3.295 (GeV/c)^2 and $|t|$ <0.800 GeV^2. The qunatity X decreases in Q^2 and $|t|$ without irregular behavior. The curves can be roughly fitted by a power law in Q^2 and $|t|$ in Figs. 5-37–5-38, respectively. The exponents are -2.70 – -1.70 for Q^2 and -0.59 – -1.70 for $|t|$.

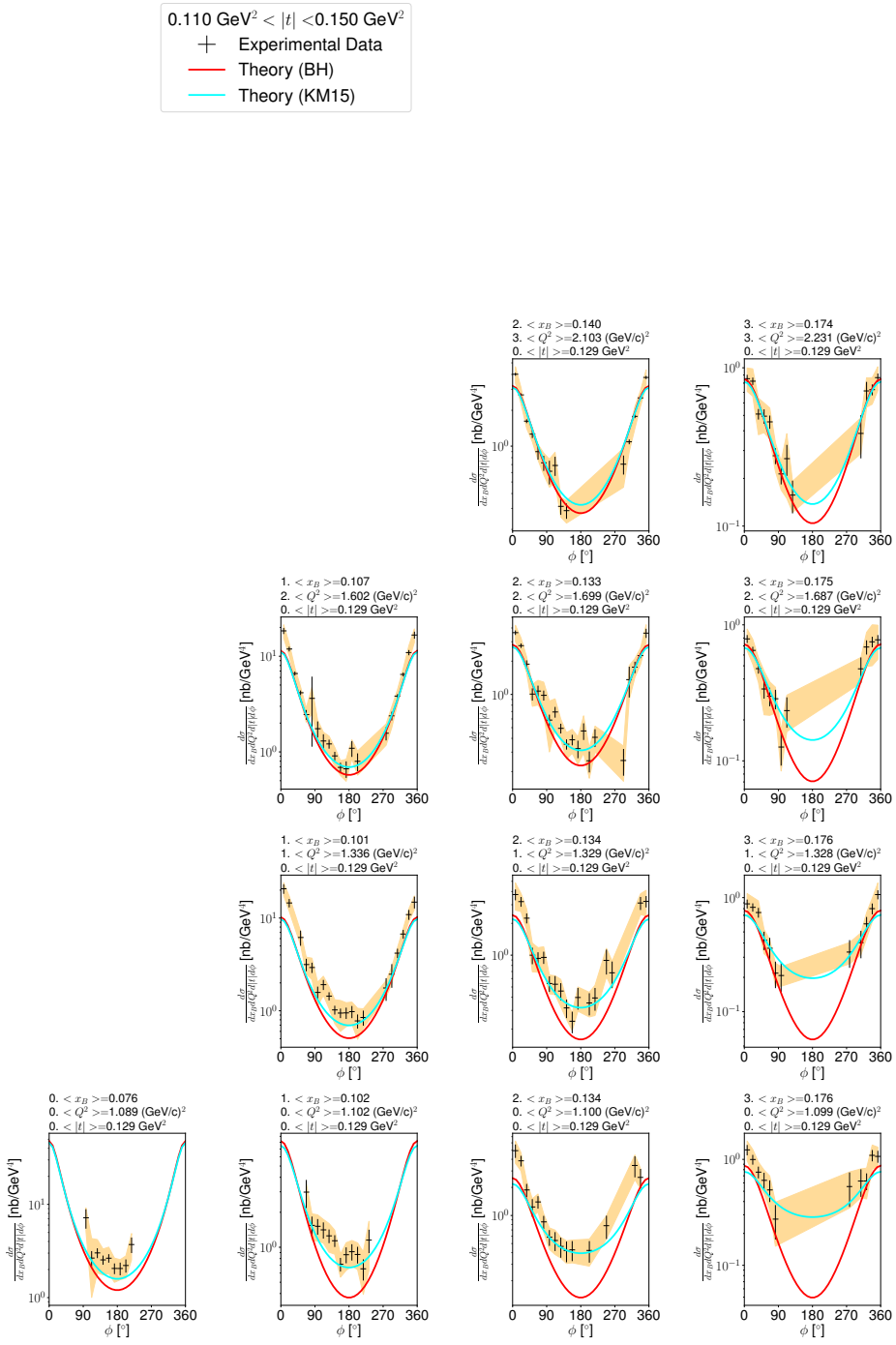

Figure 5-24: The unpolarized cross section plots in 0.110 GeV^2 $< |t| <$0.150 GeV^2 bins. The statistical uncertainty is represented by the crosses. The stamp sized cross section panels are presented in the Q^2 and x_B plane in a way that the vertical and horizontal grids are on Q^2 and x_B respectively. Each panel title has the average value of the x_B, Q^2 and $|t|$. The orange band represents the $1\sigma_{syst.}$ range.

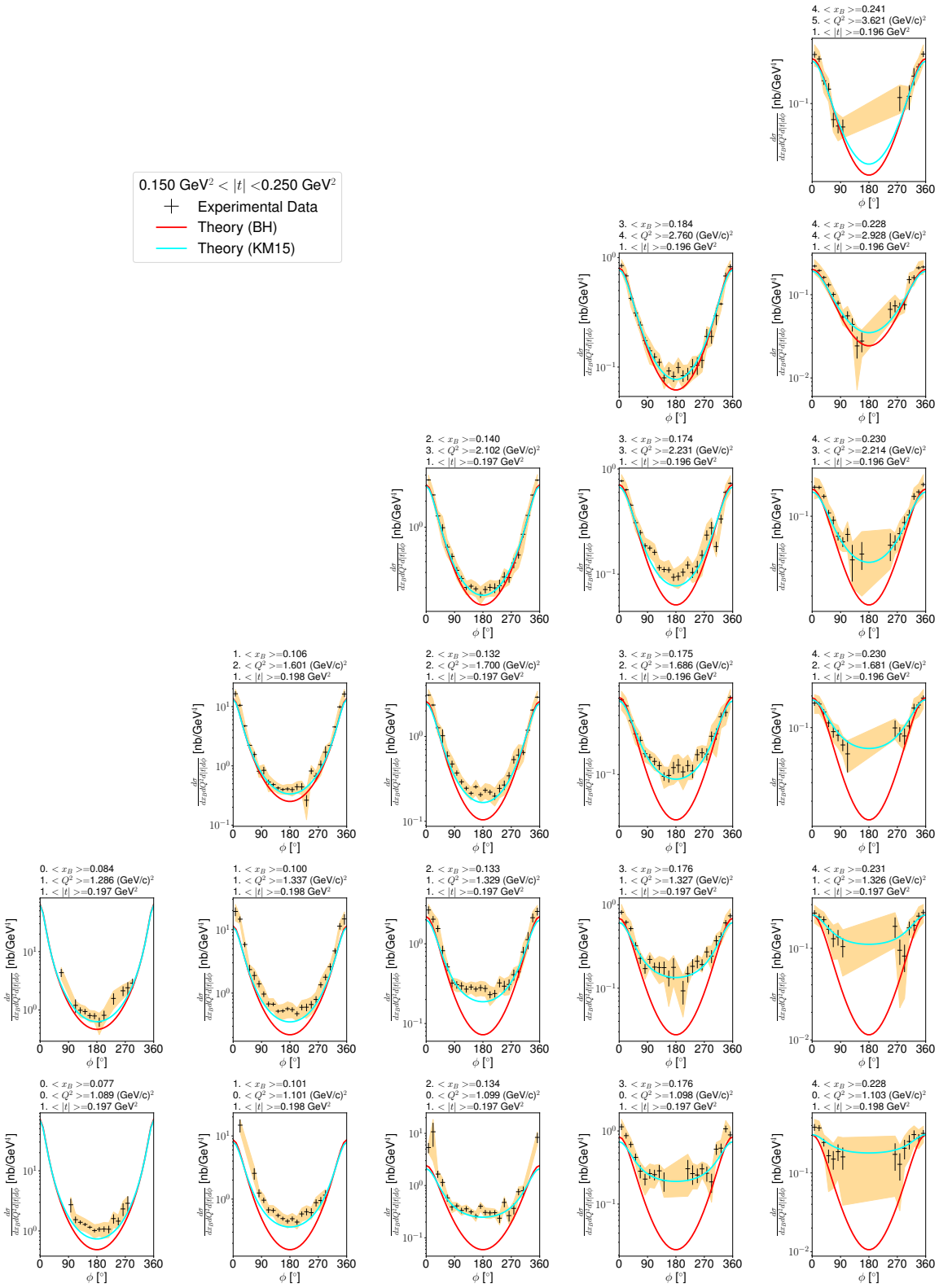

Figure 5-25: The unpolarized cross section in $x_B < 0.268$, Q^2 <4.326 $(\mathrm{GeV/c})^2$, 0.150 $\mathrm{GeV}^2 < |t| <$0.250 GeV^2 bins.

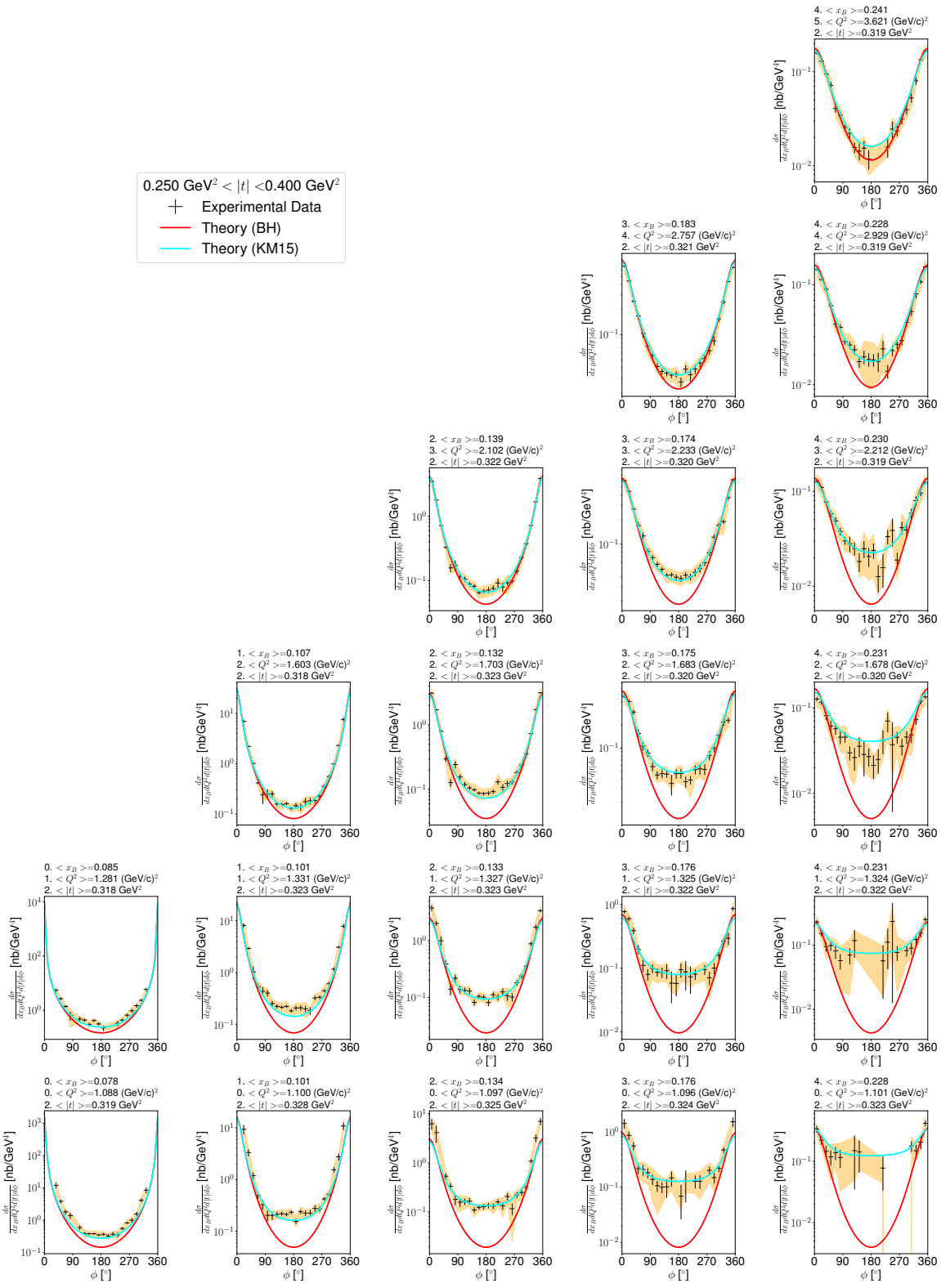

Figure 5-26: The unpolarized cross section in $x_B < 0.268$, Q^2 <4.326 $(\mathrm{GeV/c})^2$, 0.250 $\mathrm{GeV}^2 < |t| <$0.400 GeV^2 bins.

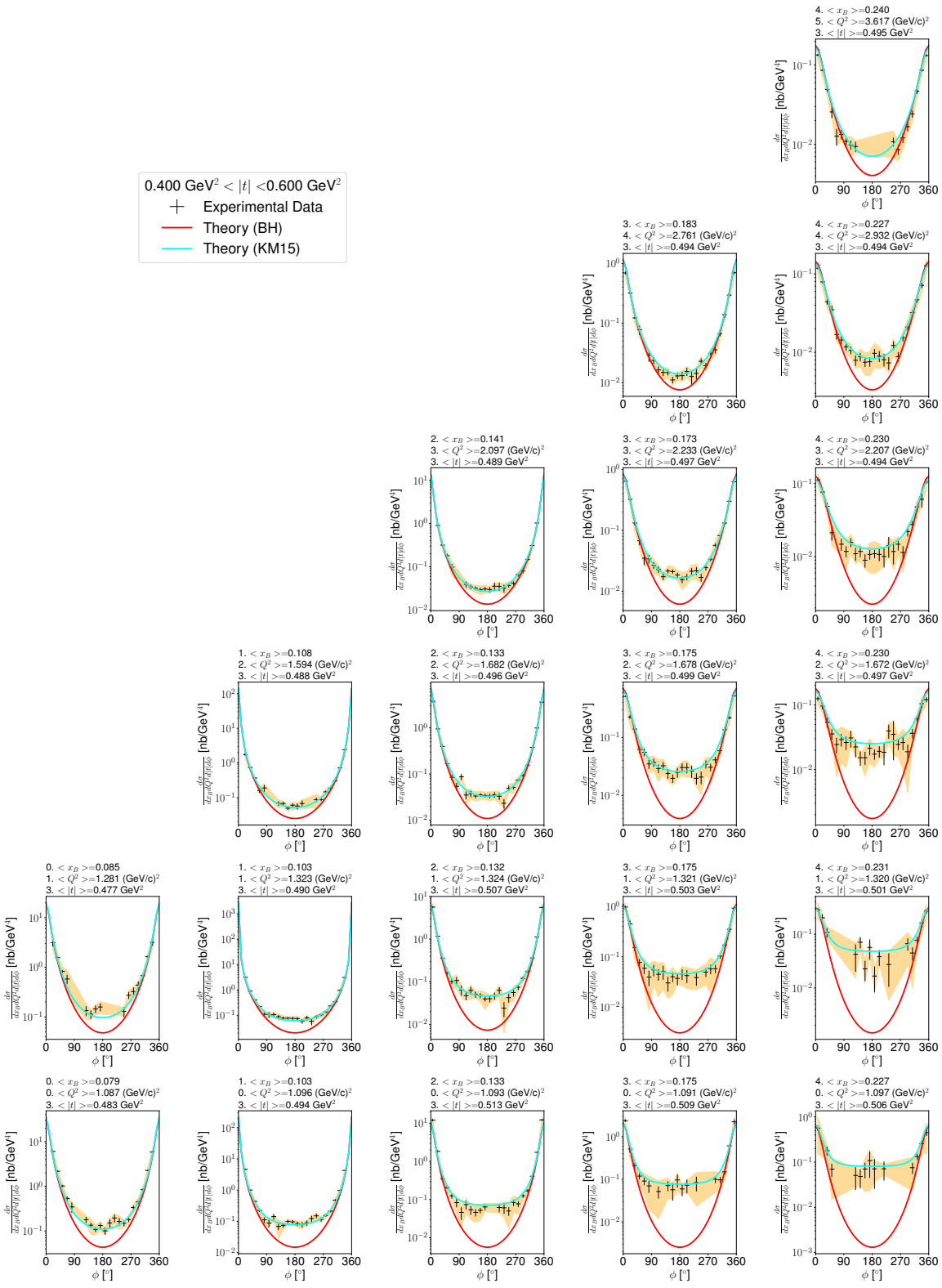

Figure 5-27: The unpolarized cross section in $x_B < 0.268$, Q^2 <4.326 $(\mathrm{GeV/c})^2$, 0.400 $\mathrm{GeV}^2 < |t| <$0.600 GeV^2 bins.

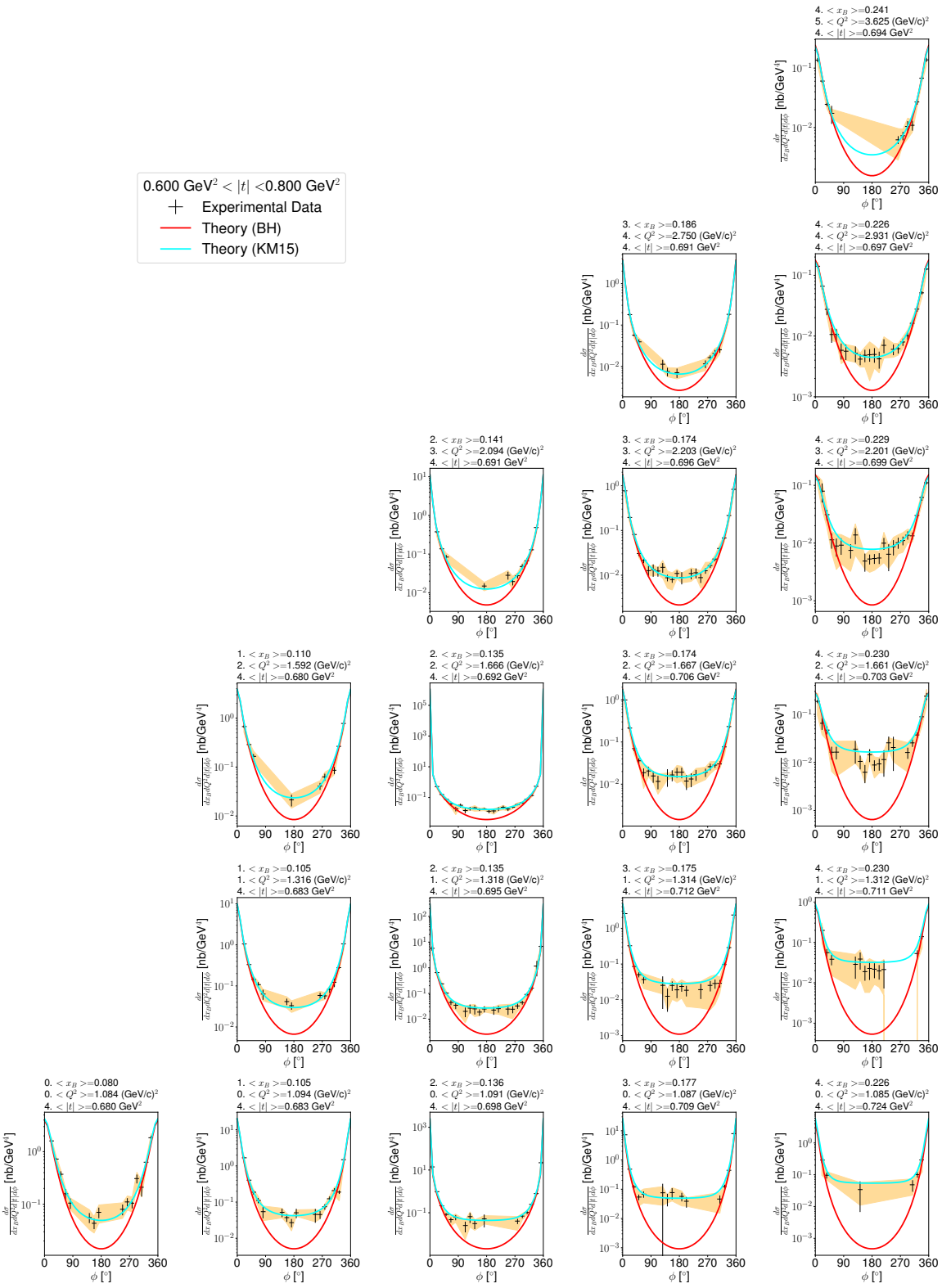

Figure 5-28: The unpolarized cross section in $x_B < 0.268$, Q^2 <4.326 (GeV/c)^2, 0.600 GeV^2 < $|t|$ <0.800 GeV^2 bins.

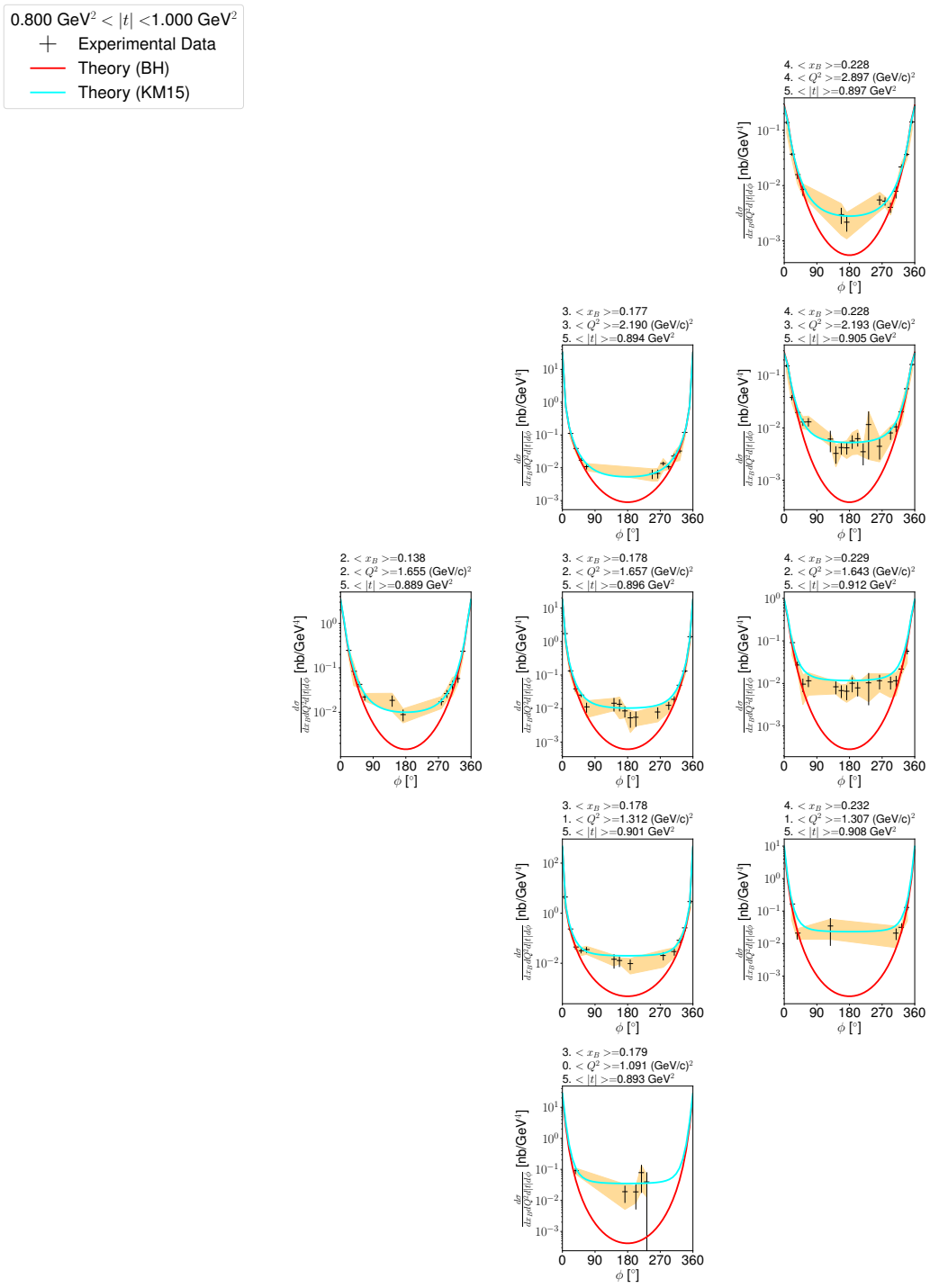

Figure 5-29: The unpolarized cross section in $x_B < 0.268$, Q^2 <4.326 $(\mathrm{GeV/c})^2$, 0.800 $\mathrm{GeV}^2 < |t| <$1.000 GeV^2 bins.

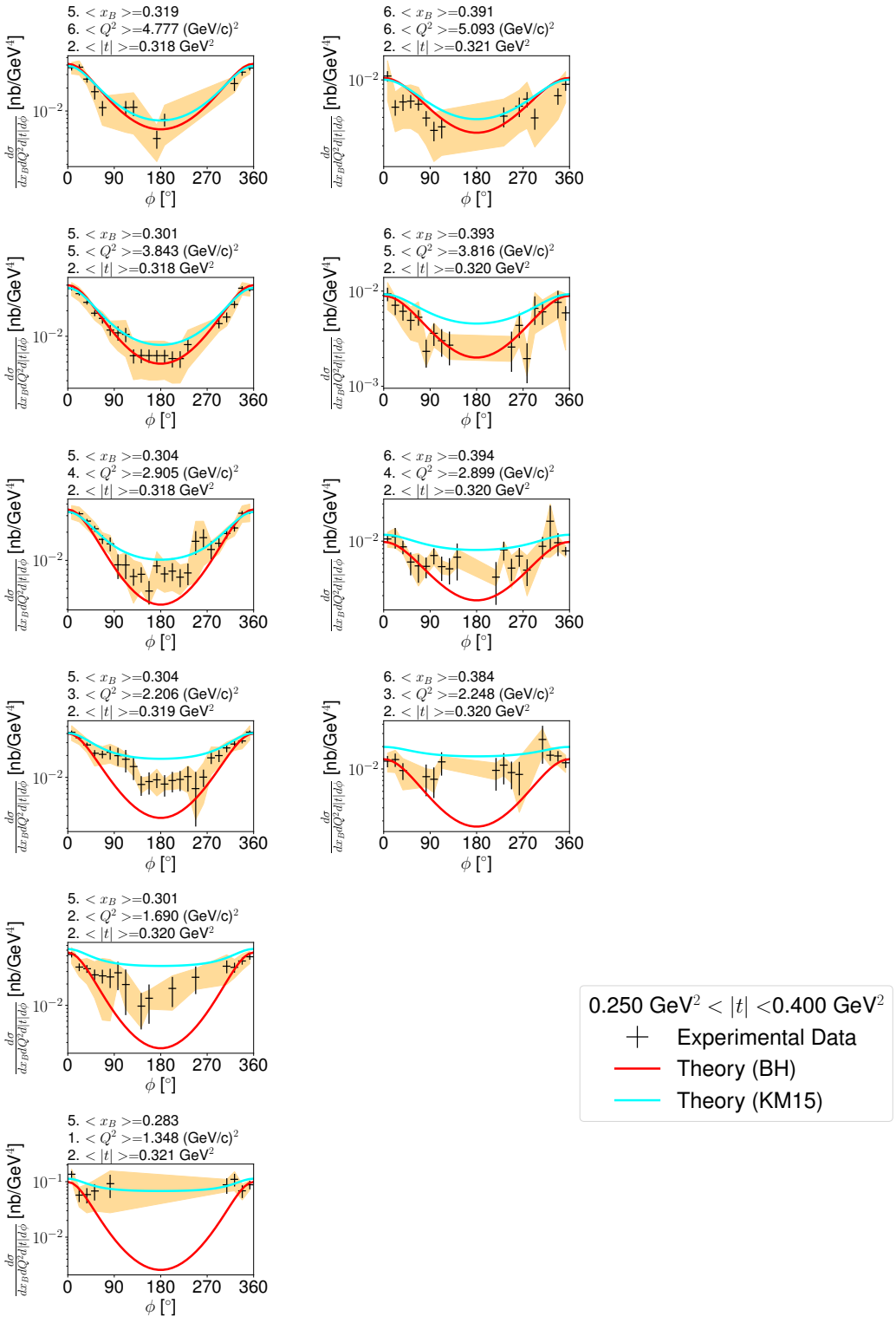

Figure 5-30: The unpolarized cross section in x_B >0.268, 1.200 (GeV/c)^2 < Q^2 <5.761 (GeV/c)^2, 0.400 GeV^2 < $|t|$ <0.600 GeV^2 bins.

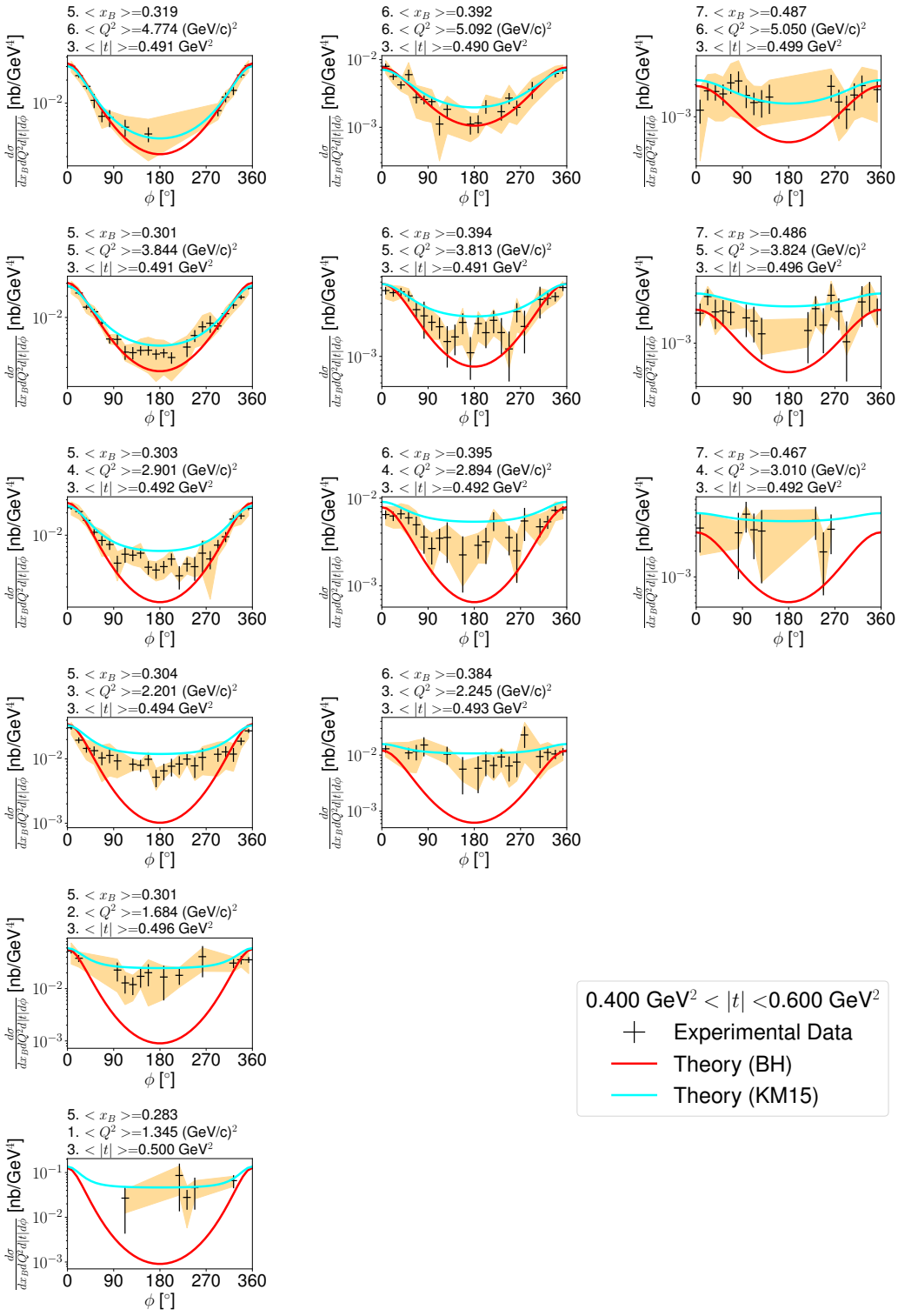

Figure 5-31: The unpolarized cross section in x_B >0.268, 1.200 (GeV/c)^2 < Q^2 <5.761 (GeV/c)^2, 0.600 GeV^2 < $|t|$ <0.800 GeV^2 bins.

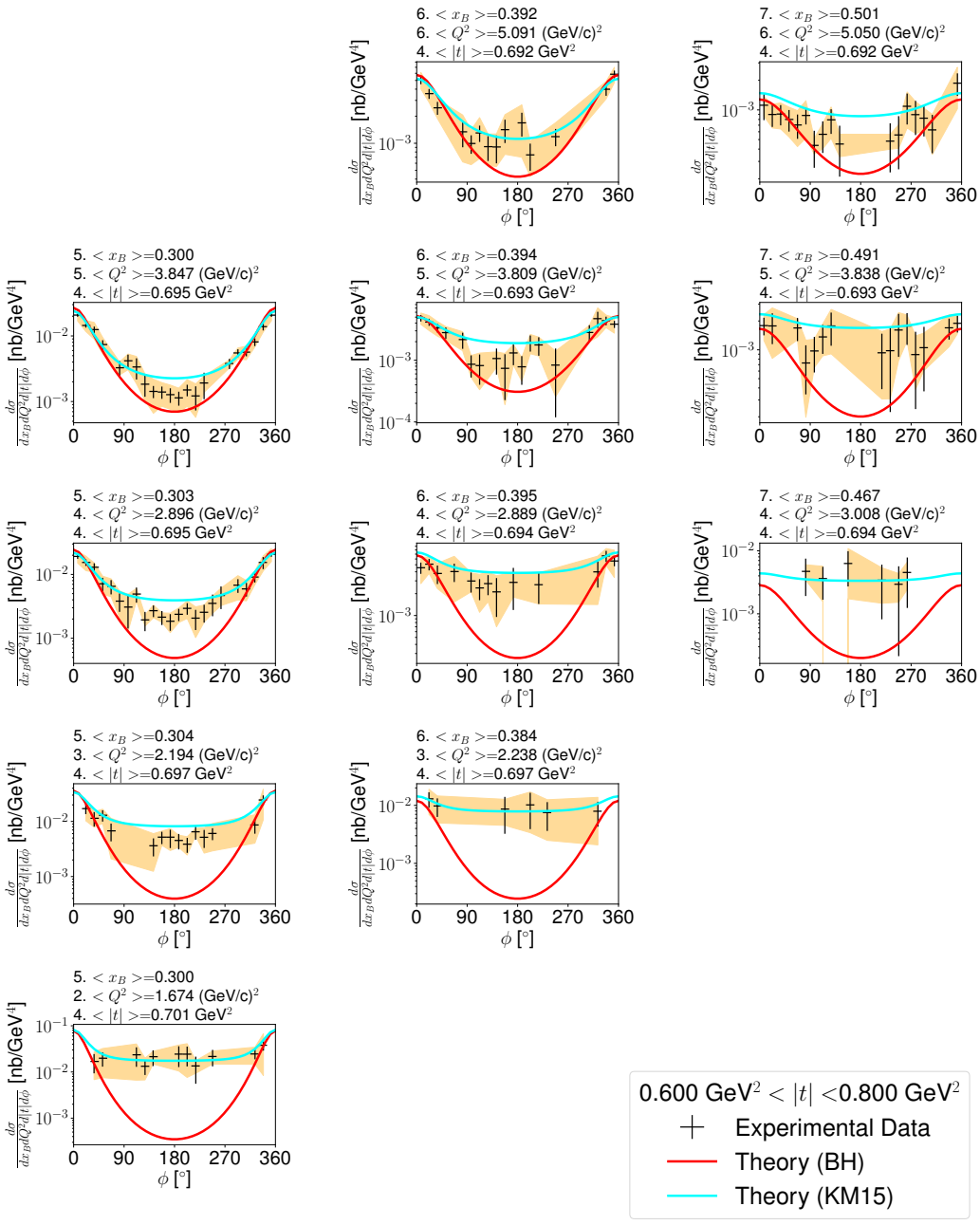

Figure 5-32: The unpolarized cross section in x_B >0.268, 1.200 (GeV/c)^2 < Q^2 <5.761 (GeV/c)^2, 0.800 GeV^2 < |t| <1.000 GeV^2 bins.

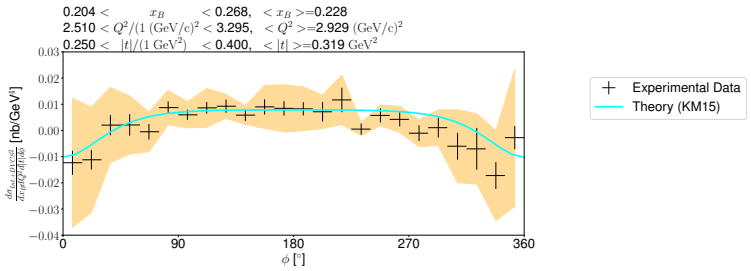

Figure 5-33: The pure DVCS and the interference contribution $d\sigma_{unpol.,Int.+DVCS^2}$ as a function of ϕ in one bin, 0.204< x_B <0.268, 2.510 (GeV/c)^2 < Q^2 <3.295 (GeV/c)^2 and 0.250 GeV^2 < |t| <0.400 GeV^2.

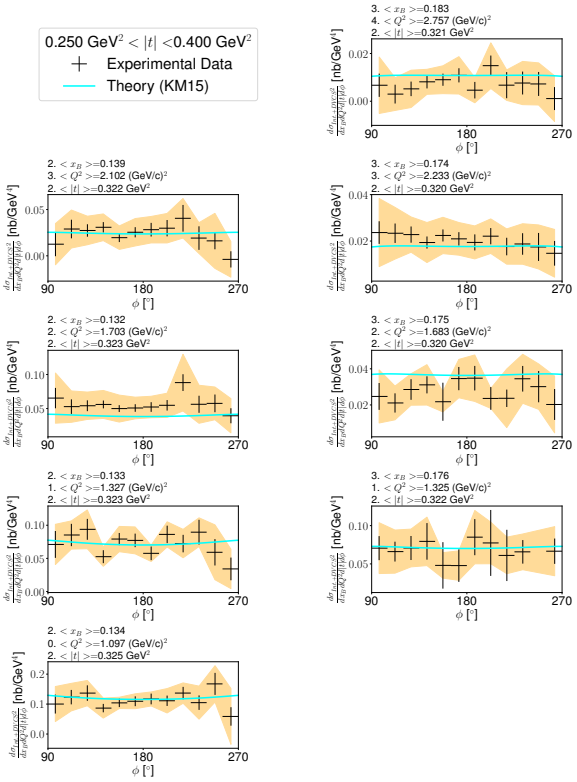

Figure 5-34: The pure DVCS and the interference contribution $d\sigma_{unpol.,Int.+DVCS^2}$ as a function of ϕ in Q^2−x_B landscape for 0.118< x_B <0.204, 1.000 (GeV/c)^2 < Q^2 <3.295 (GeV/c)^2 and 0.250 GeV^2 < |t| <0.400 GeV^2. The ϕ ranges are from 90° to 270°.

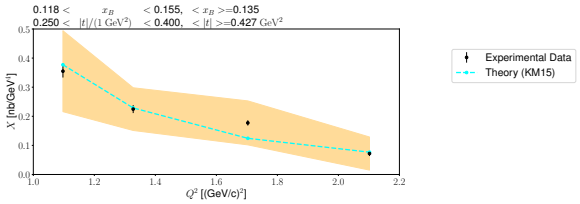

Figure 5-35: The plot showing the Q^2 dependence of X in 0.118< x_B <0.155, 0.250 GeV^2 < $|t|$ <0.400 GeV^2. The black dots with vertical error bars are the experimental data. The orange band represents the $1\sigma_{syst.}$ range, which is consistent with the KM prediction shown as the cyan dotted curve.

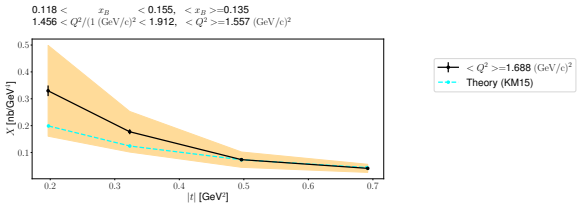

Figure 5-36: The plot showing the Q^2 dependence of X in 0.118< x_B <0.155, 1.456 (GeV/c)^2 < Q^2 <1.912 (GeV/c)^2.

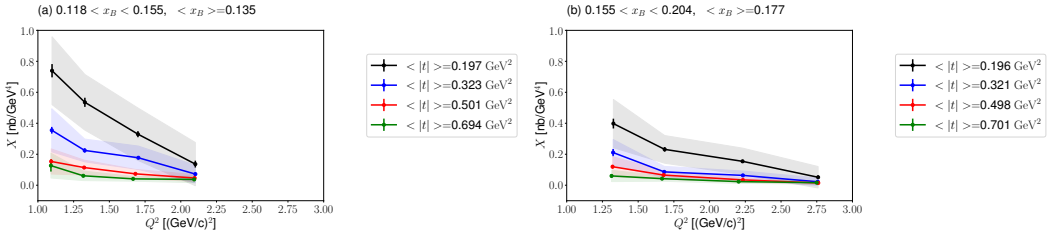

Figure 5-37: The plots showing the Q^2 dependence of X at (a) < x_B >= 0.135 and (b) < x_B >=0.177.

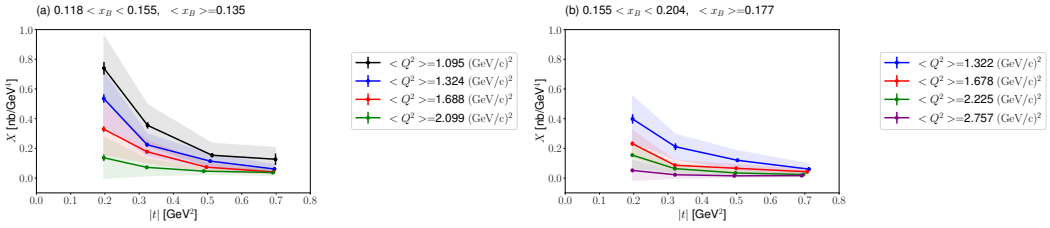

Figure 5-38: The plots showing the $|t|$ dependence of X at (a) < x_B >= 0.135 and (b) < x_B >=0.177.

5.9 Polarized Cross Sections

The polarized cross sections in one $|t|$ bin for the nominal set-up are presented in Fig. 5-39. The KM15 prediction is presented with the cyan curves. The systematic uncertainties in the helicity dependent cross sections are derived in a similar way to derivation of the unpolarized cross section systematic uncertainties. However, each helicity state splits the number of events, and moreover the minus helicity state has usually less statistics whereas the plus state is higher. Estimating the polarized cross section uncertainties is thus challenging, and the statistical uncertainty is about $\sqrt{2}$ times the statistical uncertainty of the unpolarized cross section. To tackle this challenge, the helicity dependent cross sections will be studied with a coarser binning. Fig. 5-39 shows the absolute polarized cross section at one bin, $0.204 < x_B < 0.268$, $2.929\ (\mathrm{GeV/c})^2 < Q^2 < 2.510\ (\mathrm{GeV/c})^2$, $0.250\ \mathrm{GeV}^2 < |t| < 0.400\ \mathrm{GeV}^2$. The modified polarized cross section is shown in Fig. 5-40 for the same bin. The BMK approximation predicts the polarized cross sections to have the following forms.

$$d\sigma_{pol.,\ DVCS^2} = \Gamma \frac{1}{y^2 Q^2} s_1^{\mathrm{DVCS}} \sin(\phi) \tag{5.29}$$

$$d\sigma_{pol.\ Int.} = \Gamma \frac{1}{x_B y^3 t \mathcal{P}_1(\phi)\mathcal{P}_2(\phi)} (s_1^{\mathcal{I}} \sin(\phi) + s_2^{\mathcal{I}} \sin(2\phi)) \tag{5.30}$$

For high Q^2, where the interference term is dominant, the modified polarized cross sections is predicted to follow a sine function. The one bin result at Fig. 5-40 is fitted to the sine function with the p-value 0.838.

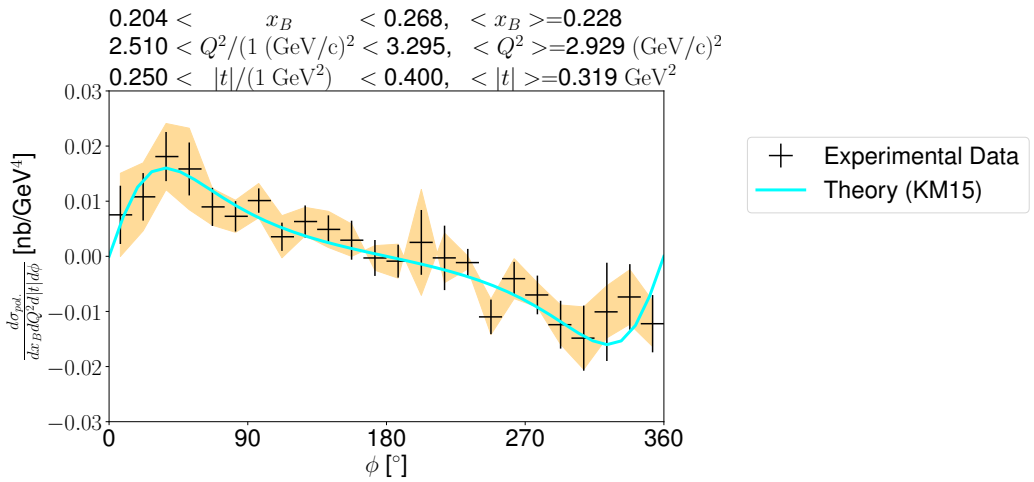

Figure 5-39: The pure DVCS and the interference contribution $d\sigma_{unpol.,Int.+DVCS^2}$ as a function of ϕ in 0.204< x_B <0.268, 2.929 $(\mathrm{GeV/c})^2$ < Q^2 <2.510 $(\mathrm{GeV/c})^2$, 0.25 GeV^2 < $|t|$ <0.40 GeV^2.

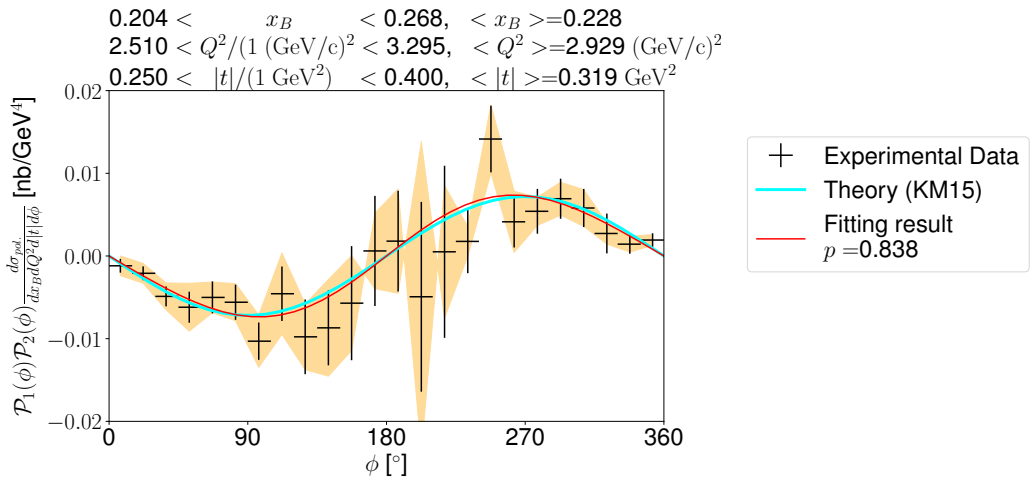

Figure 5-40: The pure DVCS and the interference contribution $d\sigma_{unpol.,Int.+DVCS^2}$ as a function of ϕ in 0.204< x_B <0.268, 2.929 $(\mathrm{GeV/c})^2$ < Q^2 <2.510 $(\mathrm{GeV/c})^2$, 0.25 GeV^2 < $|t|$ <0.40 GeV^2.

5.10 Conclusions

We have presented the BH-DVCS cross sections over a wide range of $(x_B, Q^2, |t|)$ kinematics. The BH-DVCS unpolarized and polarized cross sections are in reasonable agreement (within the 1σ systematic uncertainty level) with the KM15 model that resulted from fitting the previous experimental results from both collider and fixed-target experiments. This conclusion is consistent with the Hall A cross section results

performed recently [129], even though the reference reported tension in the fitted CFF terms. Together with the Hall A results, the measurement reported here is one of the earliest DVCS results from the JLab 12 GeV era as well as the first cross section determination from the CLAS12 experiment. While the Hall A measurement provides a more precise measurement, these data cover a much wider kinematic range, as illustrated in Fig. 5-41.

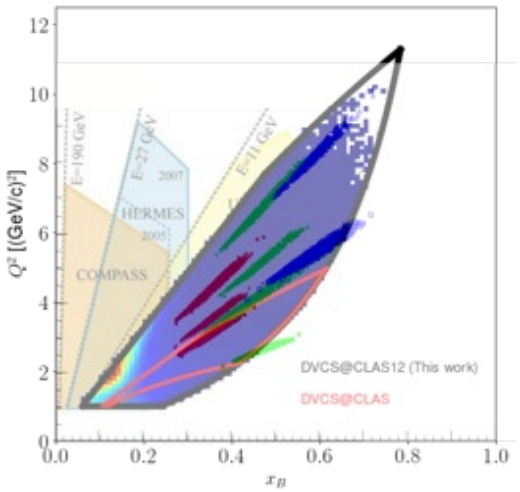

Figure 5-41: The $Q^2 - x_B$ kinematic reach of various fixed-target experiments. The original image was from [189]. The colored segments show the Hall A DVCS measurements after the CEBAF 12 GeV upgrade and were imported from [190] (x_B= 0.36 (red), 0.48 (green) and 0.6 (blue). The black and red feather-shaped figures enclose the DVCS $Q^2 - x_B$ regions at CLAS12 and CLAS.

The Q^2 and $|t|$ dependence of interference and DVCS contribution $d\sigma_{int.} + d\sigma_{DVCS^2}$ can be compared with the integral of unpolarized cross sections over $\phi \in (90°, 270°)$. The unpolarized cross section decreases in Q^2 and $|t|$, which is consistent with the theoretical prediction. The polarized cross section results clearly show the sine harmonics functional form, which is also consistent with the BMK approximation [76]. Combined, the results support the idea of perturbative QCD scaling at the presented kinematics region as discussed in [110] at higher x_B.

For a thorough CFF fitting with the experimental results, it is necessary to disentangle the interference term $d\sigma_{Int.}$ and the pure DVCS contribution $d\sigma_{DVCS^2}$ as discussed in Chapter 1. This step is often called the generalized Rosenbluth separa-

tion, which has been discussed in [126, 191, 192]. One method to perform this is to utilize the differences in ϕ dependences at the same (x_B, Q^2, $|t|$) bin. As presented Fig. 1-9, the interference term is predicted to be dominant at ϕ around 0° and 360°. However, these regions are also pure BH dominant. Thus, instead of normalizing the unpolarized cross sections to the pure BH in this region, as done here, more detailed studies of the CLAS12 detector efficiency will be required to achieve the final absolute cross sections. Another method is to incorporate the measurement from the different beam energies as performed in Hall A DVCS experiments [129, 191]. This technique will be also available at CLAS12 by including Run Group K data with lower beam energy (6.5 GeV and 7.5 GeV) and the unpolarized LH_2 target, which are being analyzed at present [193]. Processing of Run Group A data taken in spring 2019 with 10.2 GeV beam energy is ongoing. Including this data will add more statistics for the CFF fitting.

In addition to this work, there will be much more data on GPDs forthcoming from the CLAS12 detector. The proton DVCS BSA preliminary results are under CLAS12 internal review [194] for the same experimental set-up as reported in this thesis. The BMK approximation predicts that the CFF dependences of both the interference and pure DVCS terms should be slightly different when polarized targets are used. The cross sections, TSA, and BSA results with the polarized targets at CLAS12 will provide important data input for the global fitting program. The global fitting with the unpolarized and polarized target data is discussed in [131]. The data taking and processing with the longitudinally polarized NH_3 target is ongoing. Measurement of the DVCS process on the neutron is also ongoing with the CLAS12 detector. The collaboration has already performed measurements with an unpolarized LD_2 target [195]. The measurements on longitudinally polarized ND_3 [196] is in progress and will be followed by measurements on a polarized NH_3 target. The installation of longitudinally or transversely polarized ^{3}He targets is being studied [124, 125]. The GPDs $H, \tilde{H}, E, \tilde{E}$ accessible by DVCS measurements on unpolarized targets are occasionally referred to as chiral-even GPDs. The transversity (chiral-odd) GPDs and gluon GPDs are sensitive to DVMP channels. The analyses of RG-A data for

these exclusive channels are ongoing with the BSA [197, 198] and the cross section measurement [199, 200] technique. This first cross-section measurements of exclusive channels will be a valuable benchmark for further exclusive channel studies and the efficiency determination for the recently-built CLAS12 detector.

The GPD program addresses a number of important and fundamental scientific questions: studying the spin [52] and mass decomposition [201] of nucleons, the dynamic properties of proton [86–88] and imaging of nucleons [70]. To achieve the program goals, surveying the CFFs over a wide kinematics region is a central prerequisite. In addition to including the results in global fits [95], one can also demand consistency with lattice QCD calculations, as discussed in [96]. This measurement will benefit the global fitting program at the fixed-target experiment kinematics, and will also be useful in predicting DVCS results in future experiments. The fixed-target upgrade plans in Jefferson Lab include performing measurements with positron beam [120, 121], beam energy upgrade to 20–24 GeV [202] and installing a new detector Solenoidal Large Intensity Device (SoLID) at Hall A [203]. An upgrade of the COMPASS, AMBER/COMPASS++ experiment [204] at Super Proton Synchrotron (SPS), Conseil Européen pour la Recherche Nucléaire (CERN) is being discussed. DVCS study in collider kinematics is a principal scientific thrust of EIC [68, 132]. The updated global fits using the data reported here will improve the quality of predictions for these new facilities, and will aid the design of new detectors. Continuous studies based on the current and future measurements will make possible new insights into the QCD structure of hadronic matter.

Bibliography

[1] P. A. Zyla *et al.*, "Review of Particle Physics," *Progress of Theoretical and Experimental Physics*, vol. 2020, no. 8, 2020, 083C01.

[2] E. Tiesinga, P. J. Mohr, D. B. Newell, and B. N. Taylor, "CODATA Recommended Values of the Fundamental Physical Constants: 2018," *Journal of Physical and Chemical Reference Data*, vol. 50, no. 3, 2021.

[3] M. E. Peskin and D. V. Schroeder, *An Introduction to Quantum Field Theory.* Westview Press, 1995, Reading, USA: Addison-Wesley (1995) 842 p.

[4] C. N. Yang and R. L. Mills, "Conservation of isotopic spin and isotopic gauge invariance," *Phys. Rev.*, vol. 96, pp. 191–195, 1 1954.

[5] S. Weinberg, "A Model of Leptons," *Phys. Rev. Lett.*, vol. 19, no. 21, pp. 1264–1266, 1967.

[6] A. Salam and J. C. Ward, "Weak and Electromagnetic Interactions," *Il Nuovo Cimento*, vol. 11, no. 4, pp. 568–577, 1959.

[7] S. L. Glashow, "The Renormalizability of Vector Meson Interactions," *Nuclear Physics*, vol. 10, pp. 107–117, 1959.

[8] P. W. Higgs, "Broken Symmetries and the Masses of Gauge Bosons," *Phys. Rev. Lett.*, vol. 13, no. 16, pp. 508–509, 1964.

[9] H. Geiger and E. Marsden, "On a Diffuse Reflection of the α-Particles," *Proceedings of the Royal Society of London Series A*, vol. 82, no. 557, pp. 495–500, 1909.

[10] E. Rutherford, "The Scattering of Alpha and Beta Particles by Matter and the Structure of the Atom," *Phil. Mag. Ser. 6*, vol. 21, pp. 669–688, 1911.

[11] E. Rutherford, "Collision of α Particles with Light Atoms. IV. An Anomalous Effect in Nitrogen," *Phil. Mag. Ser. 6*, vol. 37, pp. 581–587, 1919.

[12] J. Chadwick, "Possible Existence of a Neutron," *Nature*, vol. 129, p. 312, 1932.

[13] R. W. McAllister and R. Hofstadter, "Elastic Scattering of 188-MeV Electrons from the Proton and the Alpha Particle," *Phys. Rev.*, vol. 102, pp. 851–856, 3 1956.

[14] M. Gell-Mann, "A Schematic Model of Baryons and Mesons," *Phys. Lett.*, vol. 8, pp. 214–215, 1964.

[15] G. Zweig, "An $SU(3)$ model for Strong Interaction Symmetry and Its Breaking. Version 1," CERN, Geneva, Tech. Rep., 1964.

[16] O. W. Greenberg, "Spin and Unitary Spin Independence in a Paraquark Model of Baryons and Mesons," *Phys. Rev. Lett.*, vol. 13, pp. 598–602, 1964.

[17] M. Y. Han and Y. Nambu, "Three Triplet Model with Double SU(3) Symmetry," *Phys. Rev.*, vol. 139, B1006–B1010, 1965.

[18] J. D. Bjorken and E. A. Paschos, "Inelastic Electron-Proton and γ-Proton Scattering and the Structure of the Nucleon," *Phys. Rev.*, vol. 185, pp. 1975–1982, 5 1969.

[19] D. P. Barber *et al.*, "Discovery of Three Jet Events and a Test of Quantum Chromodynamics at PETRA Energies," *Phys. Rev. Lett.*, vol. 43, p. 830, 1979.

[20] D. J. Gross and F. Wilczek, "Ultraviolet Behavior of Non-Abelian Gauge Theories," *Phys. Rev. Lett.*, vol. 30, no. 26, pp. 1343–1346, 1973.

[21] H. D. Politzer, "Reliable Perturbative Results for Strong Interactions?" *Phys. Rev. Lett.*, vol. 30, no. 26, pp. 1346–1349, 1973.

[22] M. Derrick *et al.*, "Measurement of the Proton Structure Function F_2 from the 1993 HERA Data," *Z. Phys. C*, vol. 65, pp. 379–398, 1995.

[23] I. Abt *et al.*, "Measurement of the Proton Structure Function $F_2(x, Q^2)$ in the Low x Region at HERA," *Nucl. Phys. B*, vol. 407, pp. 515–538, 1993.

[24] J. J. Sakurai, *Modern Quantum Mechanics; Rev. Ed.* Reading, MA: Addison-Wesley, 1994.

[25] Z. Ye, J. Arrington, R. J. Hill, and G. Lee, "Proton and Neutron Electromagnetic Form Factors and Uncertainties," *Phys. Lett. B*, vol. 777, pp. 8–15, 2018.

[26] R. G. Sachs, "High-Energy Behavior of Nucleon Electromagnetic Form Factors," *Phys. Rev.*, vol. 126, pp. 2256–2260, 6 1962.

[27] M. N. Rosenbluth, "High Energy Elastic Scattering of Electrons on Protons," *Phys. Rev.*, vol. 79, pp. 615–619, 4 1950.

[28] V. Punjabi, C. F. Perdrisat, M. K. Jones, E. J. Brash, and C. E. Carlson, "The Structure of the Nucleon: Elastic Electromagnetic Form Factors," *Eur. Phys. J. A*, vol. 51, p. 79, 2015.

[29] C. E. Carlson and M. Vanderhaeghen, "Two-Photon Physics in Hadronic Processes," *Annual Review of Nuclear and Particle Science*, vol. 57, no. 1, pp. 171–204, 2007.

[30] B. S. Henderson *et al.*, "Hard Two-Photon Contribution to Elastic Lepton-Proton Scattering Determined by the OLYMPUS Experiment," *Phys. Rev. Lett.*, vol. 118, p. 092 501, 9 2017.

[31] J. C. Bernauer, "Two-Photon Exchange: Future Experimental Prospects," *Few Body Syst.*, vol. 59, no. 6, p. 116, 2018.

[32] I. Friščić *et al.*, "Prototype Lead Tungstate Calorimeter Test for TPEX," Dec. 2021. arXiv: 2112.01606 [physics.ins-det].

[33] T. W. Donnelly, J. A. Formaggio, B. R. Holstein, R. G. Milner, and B. Surrow, *Foundations of Nuclear and Particle Physics*. Cambridge University Press, 2017.

[34] M. Thomson, *Modern Particle Physics*. New York: Cambridge University Press, 2013.

[35] J. D. Bjorken, "Asymptotic Sum Rules at Infinite Momentum," *Phys. Rev.*, vol. 179, pp. 1547–1553, 5 1969.

[36] E. D. Bloom *et al.*, "High-Energy Inelastic $e - p$ Scattering at 6° and 10°," *Phys. Rev. Lett.*, vol. 23, pp. 930–934, 16 1969.

[37] R. P. Feynman, "Very High-Energy Collisions of Hadrons," *Phys. Rev. Lett.*, vol. 23, pp. 1415–1417, 24 1969.

[38] C. G. Callan Jr. and D. J. Gross, "High-Energy Electroproduction and the Constitution of the Electric Current," *Phys. Rev. Lett.*, vol. 22, pp. 156–159, 1969.

[39] J. C. Collins, D. E. Soper, and G. F. Sterman, "Factorization of Hard Processes in QCD," *Adv. Ser. Direct. High Energy Phys.*, vol. 5, pp. 1–91, 1989.

[40] Y. L. Dokshitzer, "Calculation of the Structure Functions for Deep Inelastic Scattering and e+ e- Annihilation by Perturbation Theory in Quantum Chromodynamics. (In Russian)," *Sov. Phys. JETP*, vol. 46, pp. 641–653, 1977.

[41] V. N. Gribov and L. N. Lipatov, "Deep Inelastic *ep*-Scattering in Perturbation Theory," *Sov. J. Nucl. Phys.*, vol. 15, pp. 438–450, 1972.

[42] G. Altarelli and G. Parisi, "Asymptotic Freedom in Parton Language," *Nuclear Physics B*, vol. 126, no. 2, pp. 298–318, 1977.

[43] A. V. Manohar, "An Introduction to Spin Dependent Deep Inelastic Scattering," in *Lake Louise Winter Institute: Symmetry and Spin in the Standard Model*, Mar. 1992. arXiv: hep-ph/9204208.

[44] J. D. Bjorken, "Applications of the Chiral $U(6)\bigotimes U(6)$ Algebra of Current Densities," *Phys. Rev.*, vol. 148, pp. 1467–1478, 4 1966.

[45] J. D. Bjorken, "Inelastic Scattering of Polarized Leptons from Polarized Nucleons," *Phys. Rev. D*, vol. 1, pp. 1376–1379, 5 1970.

[46] J. Ellis and R. Jaffe, "Sum Rule for Deep-Inelastic Electroproduction from Polarized Protons," *Phys. Rev. D*, vol. 9, pp. 1444–1446, 5 1974.

[47] R. L. Jaffe and X. Ji, "Studies of the Transverse Spin Dependent Structure Function $g(2)$ (X, Q^2)," *Phys. Rev. D*, vol. 43, pp. 724–732, 1991.

[48] J. Ashman *et al.*, "A Measurement of the Spin Asymmetry and Determination of the Structure Function g_1 in Deep Inelastic Muon-Proton Scattering," *Phys. Lett. B*, vol. 206, p. 364, 1988.

[49] V. Hughes, V. Papavassiliou, R. Piegaia, K. Schüler, and G. Baum, "The Integral of the Spin-Dependent Structure Function g_1^p and the Ellis-Jaffe Sum Rule," *Physics Letters B*, vol. 212, no. 4, pp. 511–514, 1988.

[50] E. W. Hughes and R. Voss, "Spin Structure Functions," *Annual Review of Nuclear and Particle Science*, vol. 49, no. 1, pp. 303–339, 1999.

[51] R. L. Jaffe and A. Manohar, "The g_1 Problem: Deep Inelastic Electron Scattering and the Spin of the Proton," *Nucl. Phys. B*, vol. 337, pp. 509–546, 1990.

[52] X. Ji, "Gauge-Invariant Decomposition of Nucleon Spin," *Phys. Rev. Lett.*, vol. 78, pp. 610–613, 1997.

[53] C. A. Aidala, S. D. Bass, D. Hasch, and G. K. Mallot, "The Spin Structure of the Nucleon," *Rev. Mod. Phys.*, vol. 85, pp. 655–691, 2013.

[54] A. Deur, S. J. Brodsky, and G. F. De Téramond, "The Spin Structure of the Nucleon," 2018.

[55] L. Adamczyk *et al.*, "Precision Measurement of the Longitudinal Double-Spin Asymmetry for Inclusive Jet Production in Polarized Proton Collisions at $\sqrt{s} = 200$ GeV," *Phys. Rev. Lett.*, vol. 115, no. 9, p. 092 002, 2015.

[56] B. I. Abelev *et al.*, "Longitudinal Double-Spin Asymmetry for Inclusive Jet Production in $p + p$ Collisions at $\sqrt{s} = 200$ GeV," *Phys. Rev. Lett.*, vol. 100, p. 232 003, 2008.

[57] A. Adare *et al.*, "The Polarized Gluon Contribution to the Proton Spin from the Double Helicity Asymmetry in Inclusive π^0 Production in Polarized $p+p$ Collisions at $\sqrt{s} = 200$ GeV," *Phys. Rev. Lett.*, vol. 103, p. 012 003, 2009.

[58] A. Adare *et al.*, "Inclusive Double-Helicity Asymmetries in Neutral-Pion and Eta-Meson Production in $\vec{p}+\vec{p}$ Collisions at $\sqrt{s} = 200$ GeV," *Phys. Rev. D*, vol. 90, no. 1, p. 012 007, 2014.

[59] D. de Florian, R. Sassot, M. Stratmann, and W. Vogelsang, "Evidence for Polarization of Gluons in the Proton," *Phys. Rev. Lett.*, vol. 113, no. 1, p. 012 001, 2014.

[60] X. Ji, "Generalized Parton Distributions," *Annual Review of Nuclear and Particle Science*, vol. 54, no. 1, pp. 413–450, 2004.

[61] D. Müller, D. Robaschik, B. Geyer, F.-M. Dittes, and J. Hořejši, "Wave Functions, Evolution Equations and Evolution Kernels from Light-Ray Operators of QCD," *Fortschritte der Physik/Progress of Physics*, vol. 42, no. 2, pp. 101–141, 1994.

[62] X. Ji, "Deeply Virtual Compton Scattering," *Phys. Rev. D*, vol. 55, pp. 7114–7125, 11 1997.

[63] A. V. Radyushkin, "Nonforward Parton Distributions," *Phys. Rev. D*, vol. 56, pp. 5524–5557, 9 1997.

[64] R. E. Cutkosky, "Singularities and Discontinuities of Feynman Amplitudes," *J. Math. Phys.*, vol. 1, pp. 429–433, 1960.

[65] C. W. Bauer, D. Pirjol, and I. W. Stewart, "Soft Collinear Factorization in Effective Field Theory," *Phys. Rev. D*, vol. 65, p. 054 022, 2002.

[66] M. Guidal, "Generalized Parton Distributions and Deep Virtual Compton Scattering," *Prog. Part. Nucl. Phys.*, vol. 61, pp. 89–105, 2008.

[67] X. Ji, "Off Forward Parton Distributions," *J. Phys. G*, vol. 24, pp. 1181–1205, 1998.

[68] A. Accardi *et al.*, "Electron Ion Collider: The Next QCD Frontier: Understanding the glue that binds us all," *Eur. Phys. J. A*, vol. 52, no. 9, p. 268, 2016. arXiv: 1212.1701 [nucl-ex].

[69] M. Guidal, H. Moutarde, and M. Vanderhaeghen, "Generalized Parton Distributions in the Valence Region from Deeply Virtual Compton Scattering," *Rept. Prog. Phys.*, vol. 76, p. 066 202, 2013.

[70] M. Burkardt, "Impact Parameter Space Interpretation for Generalized Parton Distributions," *International Journal of Modern Physics A*, vol. 18, no. 02, pp. 173–207, 2003.

[71] A. Radyushkin, "Scaling Limit of Deeply Virtual Compton Scattering," *Physics Letters B*, vol. 380, no. 3, pp. 417–425, 1996.

[72] X. Ji and J. Osborne, "One-Loop Corrections and All Order Factorization in Deeply Virtual Compton Scattering," *Phys. Rev. D*, vol. 58, p. 094 018, 9 1998.

[73] J. C. Collins and A. Freund, "Proof of Factorization for Deeply Virtual Compton Scattering in QCD," *Phys. Rev. D*, vol. 59, p. 074 009, 7 1999.

[74] C. W. Bauer, S. Fleming, D. Pirjol, I. Z. Rothstein, and I. W. Stewart, "Hard Scattering Factorization from Effective Field Theory," *Phys. Rev. D*, vol. 66, p. 014 017, 1 2002.

[75] M. Burkardt and B. Pasquini, "Modelling the Nucleon Structure," *Eur. Phys. J. A*, vol. 52, no. 6, p. 161, 2016.

[76] A. Belitsky, D. Müller, and A. Kirchner, "Theory of Deeply Virtual Compton Scattering on the Nucleon," *Nuclear Physics B*, vol. 629, no. 1, pp. 323–392, 2002.

[77] B. Kriesten and S. Liuti, "Theory of Deeply Virtual Compton Scattering off the Unpolarized Proton," *Phys. Rev. D*, vol. 105, p. 016 015, 1 2022.

[78] D. J. Gross and S. B. Treiman, "Light-Cone Structure of Current Commutators in the Gluon-Quark Model," *Phys. Rev. D*, vol. 4, pp. 1059–1072, 4 1971.

[79] S. V. Goloskokov and P. Kroll, "Transversity in Hard Exclusive Electroproduction of Pseudoscalar Mesons," *Eur. Phys. J. A*, vol. 47, p. 112, 2011.

[80] R. L. Jaffe and X. Ji, "Chiral Odd Parton Distributions and Drell-Yan Processes," *Nucl. Phys. B*, vol. 375, pp. 527–560, 1992.

[81] R. L. Jaffe and X. Ji, "Chiral Odd Parton Distributions and Polarized Drell-Yan," *Phys. Rev. Lett.*, vol. 67, pp. 552–555, 1991.

[82] E.-C. Aschenauer, S. Fazio, K. Kumerički, and D. Müller, "Deeply Virtual Compton Scattering at a Proposed High-Luminosity Electron-Ion Collider," *JHEP*, vol. 09, p. 093, 2013.

[83] A. V. Radyushkin, "Double Distributions and Evolution Equations," *Phys. Rev. D*, vol. 59, p. 014 030, 1999.

[84] A. V. Radyushkin, "Symmetries and Structure of Skewed and Double Distributions," *Phys. Lett. B*, vol. 449, pp. 81–88, 1999.

[85] M. V. Polyakov and C. Weiss, "Skewed and Double Distributions in the Pion and The Nucleon," *Phys. Rev. D*, vol. 60, p. 114 017, 11 1999.

[86] V. D. Burkert, L. Elouadrhiri, and F. X. Girod, "The Pressure Distribution inside the Proton," *Nature*, vol. 557, no. 7705, pp. 396–399, 2018.

[87] P. E. Shanahan and W. Detmold, "Pressure Distribution and Shear Forces inside the Proton," *Phys. Rev. Lett.*, vol. 122, no. 7, p. 072 003, 2019.

[88] P. E. Shanahan and W. Detmold, "Gluon Gravitational Form Factors of the Nucleon and the Pion from Lattice QCD," *Phys. Rev. D*, vol. 99, no. 1, p. 014 511, 2019.

[89] M. Vanderhaeghen, P. A. M. Guichon, and M. Guidal, "Hard Electroproduction of Photons and Mesons on the Nucleon," *Phys. Rev. Lett.*, vol. 80, pp. 5064–5067, 23 1998.

[90] S. V. Goloskokov and P. Kroll, "The Target Asymmetry in Hard Vector-Meson Electroproduction and Parton Angular Momenta," *Eur. Phys. J. C*, vol. 59, pp. 809–819, 2009.

[91] M. V. Polyakov, "Hard Exclusive Electroproduction of Two Pions and Their Resonances," *Fizika B*, vol. 8, pp. 335–344, 1999.

[92] M. V. Polyakov and A. G. Shuvaev, "On "Dual" Parametrizations of Generalized Parton Distributions," Jul. 2002. arXiv: hep-ph/0207153.

[93] D. Müller and A. Schafer, "Complex Conformal Spin Partial Wave Expansion of Generalized Parton Distributions and Distribution Amplitudes," *Nucl. Phys. B*, vol. 739, pp. 1–59, 2006.

[94] K. Kumerički and D. Müller, "Deeply Virtual Compton Scattering at Small x_B and the Access to the GPD H," *Nucl. Phys. B*, vol. 841, pp. 1–58, 2010.

[95] K. Kumerički, S. Liuti, and H. Moutarde, "GPD phenomenology and DVCS fitting: Entering the High-Precision Era," *Eur. Phys. J. A*, vol. 52, no. 6, p. 157, 2016.

[96] Y. Guo, X. Ji, and K. Shiells, "Generalized Parton Distributions through Universal Moment Parameterization: Zero Skewness Case," 2022. arXiv: 2207.05768 [hep-ph].

[97] D. Müller, M. V. Polyakov, and K. M. Semenov-Tian-Shansky, "Dual Parametrization of Generalized Parton Distributions in Two Equivalent Representations," *JHEP*, vol. 03, p. 052, 2015.

[98] A. Freund, M. McDermott, and M. Strikman, "Modeling Generalized Parton Distributions to Describe Deeply Virtual Compton Scattering Data," *Phys. Rev. D*, vol. 67, p. 036 001, 2003. arXiv: hep-ph/0208160.

[99] S. Chekanov *et al.*, "A Measurement of the Q^2, W and t Dependences of Deeply Virtual Compton Scattering at HERA," *JHEP*, vol. 05, p. 108, 2009.

[100] S. Chekanov *et al.*, "Measurement of Deeply Virtual Compton Scattering at HERA," *Phys. Lett. B*, vol. 573, pp. 46–62, 2003.

[101] F. D. Aaron *et al.*, "Deeply Virtual Compton Scattering and Its Beam Charge Asymmetry in $e^{\pm}$ Collisions at HERA," *Phys. Lett. B*, vol. 681, pp. 391–399, 2009.

[102] A. Aktas *et al.*, "Measurement of Deeply Virtual Compton Scattering at HERA," *Eur. Phys. J. C*, vol. 44, pp. 1–11, 2005.

[103] A. Airapetian *et al.*, "Beam-Helicity and Beam-Charge Asymmetries Associated with Deeply Virtual Compton Scattering on the Unpolarised Proton," *JHEP*, vol. 07, p. 032, 2012.

[104] A. Airapetian *et al.*, "Exclusive Leptoproduction of Real Photons on a Longitudinally Polarised Hydrogen Target," *JHEP*, vol. 06, p. 019, 2010.

[105] A. Airapetian *et al.*, "Measurement of Azimuthal Asymmetries with respect to Both Beam Charge and Transverse Target Polarization in Exclusive Electroproduction of Real Photons," *JHEP*, vol. 06, p. 066, 2008.

[106] S. Pisano *et al.*, "Single and Double Spin Asymmetries for Deeply Virtual Compton Scattering Measured with CLAS and a Longitudinally Polarized Proton Target," *Phys. Rev. D*, vol. 91, no. 5, p. 052 014, 2015.

[107] H. S. Jo *et al.*, "Cross Sections for the Exclusive Photon Electroproduction on the Proton and Generalized Parton Distributions," *Phys. Rev. Lett.*, vol. 115, p. 212 003, 21 2015.

[108] F. X. Girod *et al.*, "Measurement of Deeply Virtual Compton Scattering Beam-Spin Asymmetries," *Phys. Rev. Lett.*, vol. 100, p. 162 002, 16 2008.

[109] G. Gavalian *et al.*, "Beam Spin Asymmetries in Deeply Virtual Compton Scattering (DVCS) with CLAS at 4.8 GeV," *Phys. Rev. C*, vol. 80, p. 035 206, 2009.

[110] C. M. Camacho *et al.*, "Scaling Tests of the Cross-Section for Deeply Virtual Compton Scattering," *Phys. Rev. Lett.*, vol. 97, p. 262 002, 2006.

[111] M. Defurne *et al.*, "E00-110 Experiment at Jefferson Lab Hall A: Deeply Virtual Compton Scattering off the Proton at 6 GeV," *Phys. Rev. C*, vol. 92, p. 055 202, 5 2015.

[112] K. Kumerički. (Accessed: 03/04/2022). Gepard: Tool for Studying the 3D Quark and Gluon Distributions in the Nucleon, [Online]. Available: https://gepard.phy.hr.

[113] F. D. Aaron *et al.*, "Measurement of Deeply Virtual Compton Scattering and Its t-Dependence at HERA," *Phys. Lett. B*, vol. 659, pp. 796–806, 2008.

[114] A. Airapetian *et al.*, "Measurement of the Beam Spin Azimuthal Asymmetry Associated with Deeply Virtual Compton Scattering," *Phys. Rev. Lett.*, vol. 87, p. 182 001, 2001.

[115] A. Airapetian *et al.*, "The Beam-Charge Azimuthal Asymmetry and Deeply Virtual Compton Scattering," *Phys. Rev. D*, vol. 75, p. 011 103, 2007.

[116] A. Sandacz, "COMPASS Results on DVCS and Exclusive π^0 Production," *J. Phys. Conf. Ser.*, vol. 938, no. 1, p. 012 015, 2017.

[117] S. Chen *et al.*, "Measurement of Deeply Virtual Compton Scattering with a Polarized Proton Target," *Phys. Rev. Lett.*, vol. 97, p. 072 002, 2006.

[118] M. Benali *et al.*, "Deeply Virtual Compton Scattering off the Neutron," *Nature Phys.*, vol. 16, no. 2, pp. 191–198, 2020.

[119] K. Kumerički and D. Müller, "Description and Interpretation of DVCS Measurements," *EPJ Web Conf.*, vol. 112, p. 01 012, 2016.

[120] V. Burkert *et al.*, "Beam Charge Asymmetries for Deeply Virtual Compton Scattering off the Proton," *Eur. Phys. J. A*, vol. 57, no. 6, p. 186, 2021.

[121] A. Afanasev *et al.*, "Deeply Virtual Compton Scattering using a Positron Beam in Hall-C at Jefferson Lab," *Eur. Phys. J. A*, vol. 57, no. 10, p. 300, 2021.

[122] H. S. Ko, "Neutral Pion Electroproduction and Development of a Neutral Particle Spectrometer," PhD thesis, Institut de Physique Nucleaire (IPN), Orsay, 2020.

[123] H. Avakian and others, "RGC Jeopardy Update Document," *JLAB Jeopardy*, 2011. [Online]. Available: https://www.jlab.org/exp_prog/proposals/20/Jeopardy/CLAS12%20Run%20Group%20C_Update.pdf.

[124] J. Maxwell and R. Milner, "A Concept for Polarized 3He Targets for High Luminosity Scattering Experiments in High Magnetic Field Environments," *Nucl. Instrum. Meth. A*, vol. 1012, p. 165 590, 2021.

[125] X. Li, J. Maxwell, and D. Nguyen, "Polarized ^{3}He Target in High Magnetic Field at CLAS12," in *APS April Meeting (Abstracts)*, 2022, p. D09.005.

[126] B. Kriesten *et al.*, "Extraction of Generalized Parton Distribution Observables from Deeply Virtual Electron Proton Scattering Experiments," *Phys. Rev. D*, vol. 101, p. 054 021, 5 2020.

[127] A. Stefanko, "Deeply Virtual Compton Scattering on the Proton in Hall A at Jefferson Lab," PhD thesis, Carnegie Mellon University, 2022.

[128] B. Guegan, "Study of Generalized Parton Distributions and Deeply Virtual Compton Scattering on the nucleon with the CLAS and CLAS12," PhD thesis, U. Paris-Sud 11, Dept. Phys., Orsay, 2013.

[129] F. Georges *et al.*, "Deeply Virtual Compton Scattering Cross Section at High Bjorken x_B," 2022. arXiv: 2201.03714 [hep-ph].

[130] Y. Guo, X. Ji, B. Kriesten, and K. Shiells, "Twist-Three Cross-Sections in Deeply Virtual Compton Scattering," *JHEP*, vol. 06, p. 096, 2022. arXiv: 2202.11114 [hep-ph].

[131] K. Shiells, Y. Guo, and X. Ji, "On Extraction of Twist-Two Compton Form Factors from DVCS Observables Through Harmonic Analysis," *JHEP*, vol. 08, p. 048, 2022.

[132] R. Abdul Khalek *et al.*, "Science Requirements and Detector Concepts for the Electron-Ion Collider: EIC Yellow Report," Mar. 2021. arXiv: 2103.05419 [physics.ins-det].

[133] A. Biselli, H. Egiyan, L. Elouadrhiri, D. Ireland, M. Holtrop, W. Kim, and F. Sabatié, "E12-06-119: Deeply Virtual Compton Scattering with CLAS12 at 11 GeV," *JLAB PAC 38*, 2011. [Online]. Available: https://www.jlab.org/exp_prog/PACpage/PAC38/proposals/Previously_Approved/E12-06-119_Update.pdf.

[134] V. D. Burkert *et al.*, "The CLAS12 Spectrometer at Jefferson Laboratory," *Nucl. Instrum. Meth. A*, vol. 959, p. 163 419, 2020.

[135] N. Baltzell *et al.*, "The CLAS12 Beamline and Its Performance," *Nucl. Instrum. Meth. A*, vol. 959, p. 163 421, 2020.

[136] Y. G. Sharabian *et al.*, "The CLAS12 High Threshold Cherenkov Counter," *Nucl. Instrum. Meth. A*, vol. 968, p. 163 824, 2020.

[137] M. Ungaro *et al.*, "The CLAS12 Low Threshold Cherenkov detector," *Nucl. Instrum. Meth. A*, vol. 957, p. 163 420, 2020.

[138] M. Contalbrigo *et al.*, "The CLAS12 Ring Imaging Cherenkov detector," *Nucl. Instrum. Meth. A*, vol. 964, p. 163 791, 2020.

[139] D. S. Carman *et al.*, "The CLAS12 Forward Time-of-Flight system," *Nucl. Instrum. Meth. A*, vol. 960, p. 163 629, 2020.

[140] M. D. Mestayer *et al.*, "The CLAS12 Drift Chamber System," *Nucl. Instrum. Meth. A*, vol. 959, p. 163 518, 2020.

[141] G. Asryan *et al.*, "The CLAS12 Forward Electromagnetic Calorimeter," *Nucl. Instrum. Meth. A*, vol. 959, p. 163 425, 2020.

[142] M. Amarian *et al.*, "The CLAS Forward Electromagnetic Calorimeter," *Nucl. Instrum. Meth. A*, vol. 460, pp. 239–265, 2001.

[143] A. Acker *et al.*, "The CLAS12 Micromegas Vertex Tracker," *Nucl. Instrum. Meth. A*, vol. 957, p. 163 423, 2020.

[144] M. A. Antonioli *et al.*, "The CLAS12 Silicon Vertex Tracker," *Nucl. Instrum. Meth. A*, vol. 962, p. 163 701, 2020.

[145] P. Chatagnon *et al.*, "The CLAS12 Central Neutron Detector," *Nucl. Instrum. Meth. A*, vol. 959, p. 163 441, 2020.

[146] E. P. Segarra *et al.*, "The CLAS12 Backward Angle Neutron Detector (BAND)," *Nucl. Instrum. Meth. A*, vol. 978, p. 164 356, 2020.

[147] A. Acker *et al.*, "The CLAS12 Forward Tagger," *Nucl. Instrum. Meth. A*, vol. 959, p. 163 475, 2020.

[148] R. Fair *et al.*, "The CLAS12 Superconducting Magnets," *Nucl. Instrum. Meth. A*, vol. 962, p. 163 578, 2020.

[149] B. A. Mecking *et al.*, "The CEBAF Large Acceptance Spectrometer (CLAS)," *Nucl. Instrum. Meth. A*, vol. 503, pp. 513–553, 2003.

[150] S. Boyarinov *et al.*, "The CLAS12 Data Acquisition System," *Nucl. Instrum. Meth. A*, vol. 966, p. 163 698, 2020.

[151] V. Ziegler *et al.*, "The CLAS12 Software Framework And Event Reconstruction," *Nucl. Instrum. Meth. A*, vol. 959, p. 163 472, 2020.

[152] D. S. Carman *et al.*, "The CLAS12 Central Time-of-Flight system," *Nucl. Instrum. Meth. A*, vol. 960, p. 163 626, 2020.

[153] P. Chatagnon *et al.*, "First Measurement of Timelike Compton Scattering," *Phys. Rev. Lett.*, vol. 127, no. 26, p. 262 501, 2021. arXiv: 2108.11746 [hep-ex].

[154] T. B. Hayward *et al.*, "Observation of Beam Spin Asymmetries in the Process $ep \to e'\pi^+\pi^- X$ with CLAS12," *Phys. Rev. Lett.*, vol. 126, p. 152 501, 2021. arXiv: 2101.04842 [hep-ex].

[155] S. Diehl *et al.*, "Multidimensional, High Precision Measurements of Beam Single Spin Asymmetries in Semi-inclusive $\pi+$ Electroproduction off Protons in the Valence Region," *Phys. Rev. Lett.*, vol. 128, no. 6, p. 062 005, 2022. arXiv: 2101.03544 [hep-ex].

[156] F. X. Girod, *Private Communication*, 2022.

[157] B. Raydo *et al.*, "The CLAS12 Trigger System," *Nucl. Instrum. Meth. A*, vol. 960, p. 163 529, 2020.

[158] F.-X. Girod *et al.*, *DVCS Wagon*, 2020. [Online]. Available: https://github.com/JeffersonLab/grapes/blob/master/src/main/java/org/jlab/jnp/grapes/services/DVCSWagon.java.

[159] E. Wolin *et al.*, "EVIO - A Lightweight Object-Oriented I/O package," in *2007 IEEE Nuclear Science Symposium and Medical Imaging Conference*, ser. IEEE Nucl.Sci.Symp.Conf.Rec. 2007, pp. 856–859.

[160] P. Virtanen *et al.*, "SciPy 1.0: Fundamental Algorithms for Scientific Computing in Python," *Nature Methods*, vol. 17, pp. 261–272, 2020.

[161] C. R. Harris *et al.*, "Array Programming with NumPy," *Nature*, vol. 585, no. 7825, pp. 357–362, 2020.

[162] G. van Rossum, *The Python Library Reference, Release 3.8.2*. Python misc Foundation, 2020.

[163] D. Glazier *et al.*, *CLAS12ROOT*, 2019. [Online]. Available: https://github.com/JeffersonLab/clas12root.

[164] R. Brun *et al.*, *Root-project/root: V6.18/02*, version v6-18-02, 2019. [Online]. Available: https://doi.org/10.5281/zenodo.3895860.

[165] J. Pivarski *et al.*, *Scikit-hep/uproot: 3.12.0*, version 3.12.0, 2020. [Online]. Available: https://doi.org/10.5281/zenodo.3952728.

[166] M. Düren, "DVCS and Associated Processes at HERMES," *EPJ Web Conf.*, vol. 73, p. 02 014, 2014.

[167] I. Bedlinskiy *et al.*, "Measurement of Exclusive π^0 Electroproduction Structure Functions and their Relationship to Transversity GPDs," *Phys. Rev. Lett.*, vol. 109, p. 112 001, 2012.

[168] F.-X. Girod *et al.*, *DVπ^0P Wagon*, 2020. [Online]. Available: https://github.com/JeffersonLab/grapes/blob/master/src/main/java/org/jlab/jnp/grapes/services/DVPi0PWagon.java.

[169] C. Smith, *Private Communication*, 2021.

[170] H. Avakian *et al.*, *dvcsgen*, 2018. [Online]. Available: https://github.com/JeffersonLab/dvcsgen.

[171] V. Kubarovsky *et al.*, *aao_gen*, 2017. [Online]. Available: https://github.com/JeffersonLab/aao_gen.

[172] V. A. Korotkov and W. D. Nowak, "Future Measurements of Deeply Virtual Compton Scattering at HERMES," *Eur. Phys. J. C*, vol. 23, pp. 455–461, 2002. arXiv: hep-ph/0108077.

[173] E. L. Isupov *et al.*, "Polarized Structure Function $\sigma_{LT'}$ from $\pi^0 p$ Electroproduction Data in the Resonance Region at $0.4\text{GeV}^2<Q^2<1.0\text{GeV}^2$," *Phys. Rev. C*, vol. 105, no. 2, p. L022201, 2022.

[174] A. Kim *et al.*, "Target and Double Spin Asymmetries of Deeply Virtual π^0 Production with a Longitudinally Polarized Proton Target and CLAS," *Phys. Lett. B*, vol. 768, pp. 168–173, 2017. arXiv: 1511.03338 [nucl-ex].

[175] S. Agostinelli *et al.*, "GEANT4–a Simulation Toolkit," *Nucl. Instrum. Meth. A*, vol. 506, pp. 250–303, 2003.

[176] M. Ungaro *et al.*, "The CLAS12 Geant4 Simulation," *Nucl. Instrum. Meth. A*, vol. 959, p. 163 422, 2020.

[177] V. Gyurgyan, S. Mancilla, and R. Oyarzún, "CLARA: CLAS12 Reconstruction and Analysis Framework," *J. Phys. Conf. Ser.*, vol. 762, no. 1, p. 012 009, 2016.

[178] S. Stepanyan *et al.*, *CLAS12 FD Charge Particle Reconstruction Efficiency and the Beam Background Merging*, 2020.

[179] L. W. Mo and Y.-S. Tsai, "Radiative Corrections to Elastic and Inelastic *ep* and μp Scattering," *Rev. Mod. Phys.*, vol. 41, pp. 205–235, 1969.

[180] I. Akushevich and A. Ilyichev, "Radiative Effects in Deep Virtual Compton Scattering," *Phys. Rev. D*, vol. 98, p. 013 005, 1 2018.

[181] I. Akushevich, A. Ilyichev, and N. M. Shumeiko, "QED Radiative Effects in the Processes of Exclusive Photon Electroproduction from Polarized Protons with the Next-to-Leading Accuracy," *Phys. Rev. D*, vol. 90, p. 033 001, 3 2014. [Online]. Available: https://link.aps.org/doi/10.1103/PhysRevD.90.033001.

[182] E. Veach, "Robust Monte Carlo Methods for Light Transport Simulation," PhD thesis, Stanford Univeristy), 1997.

[183] D. G. Horvitz and D. J. Thompson, "A Generalization of Sampling Without Replacement From a Finite Universe," *Journal of the American Statistical Association*, vol. 47, no. 260, pp. 663–685, 1952. (visited on 06/05/2022).

[184] M. Ungaro *et al.*, *clas12Tags*, 2016. [Online]. Available: https://github.com/gemc/clas12Tags.

[185] A. Kim, *Private Communication*, 2021.

[186] C. Dilks, *clasqaDB*, 2020. [Online]. Available: https://github.com/JeffersonLab/clasqaDB.

[187] R. Pordes *et al.*, "The Open Science Grid," *J. Phys. Conf. Ser.*, vol. 78, D. E. Keyes, Ed., p. 012 057, 2007.

[188] I. Sfiligoi *et al.*, "The Pilot Way to Grid Resources Using glideinWMS," *WRI World Congress*, vol. 2, pp. 428–432, 2009.

[189] W.-D. Nowak, "Deeply Virtual Compton Scattering: Results & Future," in *Hadron Physics 13 Topical Workshop*, Mar. 2005. arXiv: hep-ex/0503010.

[190] M. N. Hashir Rashad, "Deeply Virtual Compton Scattering at Hall A, Jefferson Lab," PhD thesis, Old Dominion University, Dec. 2020. [Online]. Available: https://www.osti.gov/biblio/1764682.

[191] M. Defurne *et al.*, "A Glimpse of Gluons through Deeply Virtual Compton Scattering on the Proton," *Nature Commun.*, vol. 8, no. 1, p. 1408, 2017.

[192] B. Kriesten, S. Liuti, and A. Meyer, "Novel Rosenbluth Extraction Framework for Compton Form Factors from Deeply Virtual Exclusive Experiments," *Phys. Lett. B*, vol. 829, p. 137 051, 2022.

[193] L. Elouadrhiri, J. A. Tan, and F.-X. Girod, "Deeply Virtual Compton Scattering Beam-Spin Asymmetry at 6.5 GeV and 7.5 GeV Polarized Electron Beam with CLAS12," in *APS April Meeting (Abstracts)*, 2022, K11.005.

[194] M. Defurne, "New DVCS Results with CLAS12 at 10.6 GeV," in *DIS2022: XXIX International Workshop on Deep-Inelastic Scattering and Related Subjects (Abstracts)*, May 2022.

[195] A. Hobart, "The Nucleon Structure and the Generalized Parton Distributions," in *Transversity 2022 (Abstracts)*, May 2022.

[196] S. Niccolai and others, "Deeply Virtual Compton Scattering on the Neutron with a Longitudinally Polarized Deuteron Target," *JLAB PAC 44*, 2016. [Online]. Available: https://www.jlab.org/exp_prog/proposals/16/E12-06-109A.pdf.

[197] A. Kim and CLAS Collaboration, "Beam Spin Asymmetry for Deeply Virtual π^0 Electroproduction with CLAS12 at Jefferson Lab," in *APS Division of Nuclear Physics Meeting (Abstracts)*, Jan. 2021, PC.006.

[198] B. A. Clary, "Exclusive Phi Production Beam Spin Asymmetry Measurements with CLAS12," PhD thesis, Connecticut U., Connecticut U., 2020.

[199] R. Johnston and CLAS12 Collaboration, "Deeply Virtual Neutral Pion Electroproduction Cross Section Off Proton at CLAS12," in *APS April Meeting (Abstracts)*, Jan. 2022, p. L11.003.

[200] P. Moran and CLAS12 Collaboration, "Exclusive Phi Electroproduction Cross Section Measurement off the Proton at CLAS12," in *APS April Meeting (Abstracts)*, Jan. 2021, T12.006.

[201] X. Ji, "QCD Analysis of the Mass Structure of the Nucleon," *Phys. Rev. Lett.*, vol. 74, pp. 1071–1074, 7 1995.

[202] A. Bogacz *et al.*, "20-24 GeV FFA CEBAF Energy Upgrade," *JACoW*, vol. IPAC2021, MOPAB216, 2021.

[203] J. P. Chen *et al.*, "A White Paper on SoLID (Solenoidal Large Intensity Device)," Sep. 2014. arXiv: 1409.7741 [nucl-ex].

[204] B. Adams *et al.*, "Letter of Intent: A New QCD facility at the M2 beam line of the CERN SPS (COMPASS++/AMBER)," Aug. 2018. arXiv: 1808.00848 [hep-ex].